THESIS FOR THE DEGREE OF DOCTOR OF PHILOSOPHY

Low Phase Noise GaN HEMT Oscillator Design based on High-Q resonators

Mikael Hörberg

Microwave Electronics Laboratory
Department of Microtechnology and Nanoscience MC2
CHALMERS UNIVERSITY OF TECHNOLOGY
Gothenburg, Sweden, April 2017

Low Phase Noise GaN HEMT Oscillator Design based on High-Q resonators

MIKAEL HÖRBERG

© Mikael Hörberg
Gothenburg, 2017

ISBN 978-91-7597-548-1

Löpnummer: 4229
Doktorsavhandlingar vid Chalmers tekniska högskola
Ny serie: (ISSN 0346-718X)

Technical Report MC2-357
ISSN 1652-0769

Microwave Electronics Laboratory
Department of Microtechnology and Nanoscience - MC2
Chalmers University of Technology
SE-412 96 Gothenburg
Sweden
Phone: +46 (0)31 772 1000

Cover:
Photos of designed and analyzed oscillators

Printed by Chalmers Reproservice
Gothenburg, Sweden, 2017

Abstract

The thesis considers the design and optimization of oscillators targeting low phase noise, given boundary conditions from the technology. Crucial technology figures are power capability, RF noise figure, low-frequency noise and the quality factor (Q-factor) of the resonator. Parameters that can be optimized from a design perspective are the resonator coupling, bias point and waveforms. The technology used in this study is GaN-HEMT, due to its low RF noise figure, high power capability and good DC to RF efficiency.

The focus has been on the resonator coupling which is an essential part of the oscillator design. Strong coupling with high power transfer to the resonator improves the phase noise. Contradictory it will also decrease the loaded Q-factor of the resonator. The optimum coupling factor is found to be between β=1/2 and β=1, defined as the ratio of power dissipated in the resonator compared to the total power delivered by the active device.

Several designs in various resonator technologies have been investigated. For example, an oscillator based on an aluminum cavity connected to a GaN-MMIC reflection amplifier has a phase noise of -145 dBc/Hz at 100 kHz offset from a 9.9 GHz carrier. The analysis of the coupling's effect to the cavity shows the optimum phase noise occurs for β close to unity, which is equivalent to an open loop gain close to 0 dB. A MMIC oscillator based on the same reflection amplifier and a quasi-lumped on-chip-resonator has a phase noise of -106 dBc/Hz at 100 kHz offset from a 15 GHz carrier, which clearly shows that the phase noise scales with the Q-factor of the resonator.

A reflection amplifier with an electronically controlled gain is also designed for control of the resonator coupling. Varactors in the termination network perform a gain adjustment without changing the bias point of the active transistor. The phase noise of a cavity oscillator based on this reflection amplifier is -136 dBc/Hz at 100 kHz offset from 8.5 GHz. A similar oscillator with a mechanically tuned cavity has about 3 dB better phase noise. Despite a small degradation in phase noise, the simplicity facilitated with electronic tuning motivates this design for practical applications.

High-Q tunable elements are key components for frequency control. This work reports an ohmic cantilever radio frequency electromechanical system (RF-MEMS) integrated on a PCB forming a tunable ground plane inside a cavity. Vertical and horizontal positions of the MEMSs are investigated for trade-offs between tuning-range, frequency resolution and phase noise. Placing the PCB at 1 mm depth from the cavity wall, 5 % tunability around 10 GHz is reached, with 100 kHz phase noise ranging from -140 dBc/Hz to -129 dBc/Hz. Placing the PCB deeper into the cavity, at 2.5 mm, the tuning range can be increased to 12.3 %, with 100 kHz phase noise varying from -133 dBc/Hz to -123 dBc/Hz.

A varactor-tuned cavity oscillator has been implemented using the same PCB. It presents a tuning range of 1.6 %. The optimum phase noise at 100 kHz is ranging from -111 dBc/Hz to -118 dBc/Hz. At 1 MHz offset the phase noise is varying from -138 dBc to -146 dBc/Hz, versus the tuning-range.

GaN-HEMT devices from different commercial vendors have been used for the designs. For modeling purposes, low-frequency noise is measured for all devices. A special high-voltage and current low-frequency noise test setup was developed and used for benchmarking of different GaN HEMTs versus other technologies, e.g., GaAs InGaP HBTs and GaAs-HEMTs.

Keywords: GaN HEMT, MMIC, MEMS, phase noise, low-frequency noise, resonator coupling, cavity resonator, reflection oscillator

List of publications

Appended papers

[A] M. Hörberg, T. Emanuelsson, H. Zirath, D. Kuylenstierna, "Analysis of a MEMS Tuned Cavity Oscillator on X-band", accepted for *IEEE Trans. Microw. Theory Techn*., 2017.

[B] M. Hörberg, T. Emanuelsson, P. Ligander, S. Lai, H. Zirath, D. Kuylenstierna, "RF-MEMS Tuned GaN HEMT based Cavity Oscillator for X-band", *IEEE Microw. Compon. Lett.,* vol. 27, pp. 46-48, 2017

[C] M. Hörberg, T. Emanuelsson, S. Lai, T. N. T. Do, H. Zirath, D. Kuylenstierna, "Phase Noise Analysis of an X-Band Ultra-low Phase Noise GaN HEMT based Cavity Oscillator," *IEEE Trans. Microw. Theory Techn.*, vol. 63, pp. 2619-2629, 2015

[D] M. Hörberg, D. Kuylenstierna, "A GaN HEMT X-band Cavity Oscillator with Electronic Gain Control", in *IEEE MTT-S Int. Dig.,* 22-27 May, San Francisco, California, 2016.

[E] M. Hörberg, D. Kuylenstierna, "Low phase noise power-efficient MMIC GaN-HEMT Oscillator at 15 GHz based on a Quasi-lumped on-chip resonator," in *IEEE MTT-S Int. Dig.,* 17-22 May, Phoenix, Arizona, 2015.

[F] M. Hörberg, S. Lai, T. N. T. Do, D. Kuylenstierna, "Phase noise analysis of a tuned-input/tuned-output oscillator based on a GaN HEMT device," in *Proc. 44th Eur. Microw. Conf. (EuMC),* 5-10 Oct. 2014, Rome, Italy, 2014 pp. 1118-1121.

[G] M. Hörberg, T. Emanuelsson, P. Ligander, H. Zirath, D. Kuylenstierna, "An X-band varactor-tuned cavity oscillator", in *IEEE MTT-S Int. Dig.,* 4-9 June, Honolulu, Hawaii, 2017.

[H] T. N. T. Do, M. Hörberg, S. Lai, D. Kuylenstierna, "Low Frequency Noise Measurements - A Technology Benchmark with Target on Oscillator Applications," in *Proc. 44th Eur. Microw. Conf. (EuMC),* 5-10 Oct. 2014, Rome, Italy, 2014 pp. 468-471.

Other papers

[a] S. Lai, D. Kuylenstierna, M. Hörberg, N. Rorsman, I. Angelov, K. Andersson*, et al.*, "Accurate Phase-Noise Prediction for a Balanced Colpitts GaN HEMT MMIC Oscillator," *IEEE Trans. Microw. Theory Techn.,* vol. 61, pp. 3916-3926, 2013.

[b] S. Lai, D. Kuylenstierna, M. Özen, M. Hörberg, N. Rorsman, I. Angelov*, et al.*, "Low Phase Noise GaN HEMT Oscillators With Excellent Figures of Merit," *IEEE Microw. Compon. Lett.,* vol. 24, pp. 412-414, 2014.

[c] T. N. T. Do, A. Malmros, M. Hörberg, N. Rorsman, P. Gamarra, C. Lacam, M-A. di Forte-Poisson, M. Tordjman, R. Aubry, D. Kuylenstierna, "Effects of surface passivation and deposition methods on the 1/f noise performance of AlInN/AlN/GaN HEMTs", *IEEE Electron Device Lett.,* vol. 36, pp. 315-317, 2015

[d] T. N. T. Do, S. Lai, M. Hörberg, H. Zirath, D. Kuylenstierna, "A MMIC GaN HEMT Voltage-Controlled-Oscillator with High Tuning Linearity and Low Phase Noise", 2015 *IEEE Compound Semiconductor Integrated Circuit Symposium (CSICS).*

[e] T. Huang, J. Bergsten, S. Gustafsson, M. Hörberg, S. Lai, M. Thorsell, D. Kuylenstierna, N. Rorsman, "Investigation of GaN HEMTs' Surface Passivation for Application in Oscillators", *manuscript.*

[f] Jingjing Chen, Zhongxia Simon He, Dan Kuylenstierna, Thomas Eriksson, Mikael Hörberg, Thomas Emanuelsson, Thomas Swahn, Herbert Zirath, "Does LO Noise Floor Limit Performance in Multi-gigabit Millimeter-wave Communication?", *manuscript.*

Thesis

[g] M. Hörberg, "Optimum GaN HEMT Oscillator Design Targeting Low Phase Noise", Techn. lic. thesis, Department of Microtechnology and Nanoscience, Chalmers University of Technology, Gothenburg, Sweden, April, 2015.

As part of the authors's doctoral studies, some of the work presented in this thesis has previously been published in [g]. Figures, tables and text from [g] may therefore be fully or partly reproduced in this thesis.

Notations and abbreviations

Notations

β	Coupling factor
C	Capacitance
f_{1/f^3}	Flicker noise corner frequency
f_m	Offset frequency
f_0	Carrier center frequency
F	Noise Figure
g_m	Transistor transconductance
I_c	Collector current
I_d	Drain current
k	Boltzmann's constant
L	Inductance
$\mathcal{L}(f_m)$	Single sideband phase noise at offset f_m
P_{AVO}	Available RF power
P_{RF}	RF-power
Q_0	Unloaded Quality-factor
Q_L	Loaded Quality-factor
R	Resistance
T	Temperature in Kelvin
V_c	Collector voltage
V_d	Drain voltage
ω	Angular frequency (rad/s)
Γ_R, Γ_A	Reflection coefficient to resonator, amplifier
q	Elementary charge
Y_{in}	Input admittance
Z_{in}	Input impedance

Abbreviations

AWGN	Additive White Gaussian Noise
BJT	Bipolar Junction Transistor
CMOS	Complementary Metal Oxide Semiconductor
CW	Continuous Wave
DUT	Design Under Test
DR	Dielectric Resonator
DRO	Dielectric Resonator Oscillator
EVM	Error Vector Magnitude
FET	Field Effect Transistor
FFT	Fast Fourier Transform
FOM	Figure of Merit
GaAs	Gallium Arsenide
GaN	Gallium Nitride
HBT	Heterojunction Bipolar Transistor
HEMT	High Electron Mobility Transistor
HFSS	High Frequency Structure Simulator, Software tool from Ansys Inc.
InGaP	Indium Gallium Phosphide
LFN	Low Frequency Noise
LTE	Long Term Evolution
LTI	Linear Time Invariant
LTV	Linear Time Variant
MEMS	Microelectromechanical System
MIMO	Multiple Input Multiple Output
PLL	Phase Locked Loop
QAM	Quadrature Amplitude Modulation
SiC	Silicon Carbide
SiGe	Silicon Germanium
SIW	Substrate Integrated Waveguide
SNR	Signal to Noise Ratio
SSB	Single Side Band
VCO	Voltage Controlled Oscillator
YIG	Yttrium-Iron-Garnet, ferromagnetic resonator

Contents

Chapter 1.

Introduction

Ever since I was a child, I have been interested in radio equipment. It started in the early 1980's, when I was around ten years old, and my father bought me an electronic hobby kit for simple experiments. The kit provided possibilities of building an AM-transmitter with a few tens meter range in the medium wave band using an ordinary transistor radio. Fascinated by the radio technology, and unaware about radio regulations, I tried to improve the range, transmit quality and to enable other frequencies. By that time, I had very little knowledge about limitations of performance in radio communication. Nevertheless, these were my first steps towards a career as radio developer at Ericsson and a Ph.D. in oscillator design at the Microwave Electronics Laboratory at Chalmers.

Evolution of the oscillator

In the early days of microwave engineering, the invention of the oscillator made it possible to build a signal source to verify Maxwell's equations. Heinrich Hertz was a pioneer in this area, and with the construction of a spark gap generator, he could generate electromagnetic waves. The radiated signal was broad and covered from hundreds of Hz to several hundreds of MHz [1]. Hertz's pioneering work was followed by several similar experiments elaborating with Maxwell's theory. The oscillator circuits were studied in details, and models of the behavior were developed. The knowledge that the oscillator had to consist of a frequency selective resonator and an amplifying part to compensate for its loss was established as well as feedback theories for stability analysis and fulfillment of the oscillation criteria [2], [3], [4].

Historically, the parameters measured for oscillators were the frequency of oscillation, power and noise. Early experiments were based on trial and error, without deeper insight into the theory. Later the popular classic papers of how to synthesize ideal oscillators were written as from Colpitts [5], [6] and Clapp [7], [8]. An early paper to describe the noise properties was presented by Leeson in 1966 [9]. He defined many of the key parameters in oscillator design, such as the importance of the power coupled to the resonator, the amplifier noise figure, the quality factor of the resonator and the noise behavior versus oscillation frequency and offset frequency. Other important contributions were Kurokawa's analysis of frequency stability [10], [11] and Rizzoli's detailed analysis of noise sources and their contribution to phase noise [12]. Driven by needs from computer aided design (CAD) applications, transistor models were developed, e.g., Gummel-Poon for the bipolar transistors [13] and various models of field effect transistor (FET and JFET etc.) with noise properties [14], [15], [16], [17].

A different approach to models for general noise theory was presented by Lee and Hajimiri [18]. They considered the time-varying behavior of the current waveform in the transistor and formed a theory based on noise impulse functions of the oscillating periodic signal.

The improved transistor models and theory of noise generation together with better simulators, as microwave harmonic-balance for frequency domain analysis and different time-domain simulators, have been vital steps towards improved oscillators.

Oscillators and phase noise in communication systems

The ever-increased need of data capacity, as well as better coverage in modern communication systems, force the radio parts to have the cutting edge performance. The capacity entails a higher symbol rate, which involves a larger modulation bandwidth, or in reality with spectral bandwidth limitations, an improved spectral efficiency with a more advanced modulation format.

One of the main limitations of the spectral efficiency is spectral purity of the local oscillator (LO) used for frequency translation [19], [20]. Even for high-frequency systems, e.g. emerging standards as 5G, and millimeter-wave point-to-point communication, e.g., the E-band, the LO signal is generated at a relatively low frequency and subsequently multiplied, using frequency multipliers. Frequency multiplication will degrade near carrier phase noise as well as far carrier noise that is limited by the signal to noise ratio of the oscillator.

According to linear noise theory, e.g., Leeson's equation [9], near carrier phase noise as well as far carrier noise floor benefit from a high power process such as wide bandgap GaN High Electron Mobility transistors (GaN-HEMTs). This is an emerging technology for power electronics due to its high breakdown voltage, high power capability, and good efficiency. A drawback with GaN-HEMTs is the high amount of flicker noise that up-convert to near carrier phase noise. However, in wideband systems, near carrier phase noise is less critical for capacity compared to far carrier noise. Nevertheless, near carrier noise must be sufficiently good to avoid phase slipping issues and problems in the clock recovery. These issues may be addressed by using a high-Q resonator so that the oscillator reaches good near-carrier phase noise, despite relatively high flicker noise.

The resonator coupling is essential for minimizing the phase noise [21]. Other critical issues are frequency tuning for PLL-locking and techniques for wide frequency reconfiguration. Any tuning or reconfiguration will inevitably degrade the spectral purity of the oscillator signal. High-Q tuning elements, as RF-MEMS switches [22] for digital control combined with weakly connected solid state varactors for analog tuning, is an interesting technology choice.

Contribution of this work

This thesis reports on GaN-HEMT oscillators where the coupling between the active device and the passive resonator is carefully optimized for best phase noise given the properties of the used components. All designs are based on AlGaN/GaN-HEMTs with very similar properties while the passive resonators are varied as well as the coupling methods. Moderate-Q integrated resonators, as well as high-Q cavity resonators, have been investigated. Further, trade-offs between tunability and phase noise are investigated.

Different tuning elements, e.g., MEMS and semiconductor varactors have been used. In all designs, the phase noise is analyzed carefully and benchmarked versus the theoretical noise floor [21], [23].

Some examples of designed oscillators are reported in Paper [A-G]. Paper [C] shows an aluminum cavity connected to a GaN-HEMT MMIC reflection amplifier. The coupling to the cavity is adjusted by changing the position of the cavity along a microstrip line, the optimum phase noise is showing a state-of-the-art performance for GaN-HEMT oscillators of -145 dBc/Hz at 100 kHz offset from a 9.9 GHz carrier. Paper [E] reports on the same MMIC-amplifier integrated with an on-chip-resonator using a coupling network based on a quasi-lumped impedance transformation. The phase noise is -106 dBc/Hz at 100 kHz from a 15 GHz oscillation frequency. Roughly 40 dB difference in phase noise can be explained by a factor 100 difference in Q-factor.

Mechanically tuning of the oscillator coupling as in Paper [C] is efficient but not production friendly. An alternative is to control the coupling factor by adjusting the amplifier gain. Paper [D] reports on an oscillator based on a reflection amplifier with electronic gain control implemented with varactors in the terminating network. A phase noise of -136 dBc/Hz at 100 kHz offset from an 8.5 GHz oscillation frequency is measured for this circuit, which is 3 dB worse compared to a mechanically tuned oscillator in the same process, demonstrating that electronic tuning is feasible without drastic degradation in performance.

The thesis also investigates tunable and reconfigurable cavity oscillators. Paper [B] reports on a MEMS-tuned cavity oscillator, where digital RF-MEMS-switches are embedded in the cavity resonator to create an electronically tunable ground plane. The concept is further investigated in Paper [A] where several cavity configurations are analyzed. Trade-offs between digital tuning range, frequency resolution and quality-factor of the resonator are discussed. This is performed by changing the position of the MEMSs in the horizontal and vertical position inside the cavity. An optimum performance of -123 dBc/Hz to -133 dBc/Hz with 12.3 % tunability around 10 GHz is reached. The RF-MEMS tuning can be combined with an analog tuning to enable PLL-locking. A method to couple a varactor inside the cavity with the same building practice is presented in Paper [G].

Paper [F] demonstrates a hybrid resonator with a lumped LC-tank connected to a single GaN-HEMT device, with a tuned input and output network. It is flexibly designed to study the up-converted phase noise from a bare die transistor device, the influence of operating point and flicker noise are discussed. It is found that far carrier noise improves with increased power while near carrier noise has an optimum for rather low DC power and degrades slightly for increased DC current associated with higher flicker noise.

Thesis Outline

The thesis is organized as follows. Chapter 2 presents background theory, design challenges, phase noise models and methods for benchmarking performance. Chapter 3 describes component and sub-block characterization used in the oscillator designs in this study, and Chapter 4 presents and discusses the complete oscillator designs investigated in this work. Finally, Chapter 5 concludes the thesis and discusses some future challenges.

Chapter 2.

Challenges in oscillator design

This chapter presents typical oscillator properties and a general circuit representation. Details about the individual building blocks are discussed with a focus on important trade-offs made by the designer, e.g., choice of active device and resonator. Linear phase noise models and optimization methods to improve phase noise are presented. In particular, the resonator coupling, and issues regarding different frequency tuning techniques are discussed. Finally, it demonstrates ways to benchmark oscillators and shows an overview of state-of-the-art published oscillators.

2.1 General requirements on oscillators

An oscillator is typically specified by a set of parameters, of which most commonly used are listed below with short description [1].

1. **Frequency range.** It is probably the most fundamental property of an oscillator. It defines the tunable range of oscillation frequencies. Typical oscillators have less than one octave tuning in frequency. Otherwise, several oscillator cores have to be combined and be provided with dividers or multipliers. The tuning is necessary for phase-locking to external references, and further, a wide tuning is often desired for, e.g., selection of oscillation sub-band.

2. **Output power.** A sufficient power level must be supplied to connected mixers in a system. Otherwise, external buffer amplifiers are needed. Typical drive levels needed for diode mixers are less than <10 dBm. Active mixers require lower level.

3. **Phase noise.** The purity of the signal is a fundamental property. Various noise sources in and outside the active part modulate the oscillator, resulting in energy and spectral distortions on both sidebands around the carrier. The noise contributes to amplitude modulation (AM) and frequency modulation (FM). Due to signal power compression, the active parts practically suppress the AM-noise, and the remaining part consists of FM-noise, which time integral is phase noise. For simplicity, the single-sideband (SSB) phase noise is used and described by power spectral density normalized to 1 Hz bandwidth.

4. **Harmonic suppression.** Harmonic suppression is important to avoid high frequency RF-leakage in distribution networks of signal power from the local oscillator to different consumers, e.g., mixers. Mixers for I and Q-modulation are sensitive for the phase balance, which can be disturbed by improper harmonic termination.
5. **Out-of-band spuriouses.** Out-of-band spuriouses not related to harmonics are often specified in regular requirements on spectral purity. A synthesizer in a phase-locked-system can generate digitally modulated spuriouses.
6. **Frequency pulling.** The oscillator must be insensitive to load variations, in particular, for reactive loads. A common remedy is to use extra buffer amplifiers. Pulling is often measured by a load change that exhibits non-unity VSWR overall phase variations. Pulling robustness is needed if several oscillators are combined in a system with potential RF-leakage and risks of frequency injection locking.
7. **Frequency pushing.** The oscillator must be robust to variations in power supply voltage and must have low impact on the frequency.
8. **Tuning characteristics.** This parameter describes the oscillation frequency dependence versus the tuning voltage. Ideally, a linear dependency is desired. At least, the oscillator must have a proper oscillation over the whole tuning range, especially for 0 V to enhance a proper start-up condition. A monotonic and continuous behavior is important in a phase-locked system.

   Large tuning sensitivity increases the up-conversion of modulation noise, which sets a strict requirement on the noise level on the tuning circuitry.
9. **Power consumptions and efficiency.** These parameters are always of interest, especially in multi-radio systems with several oscillators.

The short-term behavior of the signal purity is usually defined as phase noise in the spectrum domain as Figure 2-1 (a), and the long-term frequency deviation is normally defined in the time domain as Figure 2-1 (b). The long-term drift is seldom of interest for a voltage controlled oscillator as it normally is locked to a long-time stable reference.

In communication systems, the phase noise within the modulation bandwidth close to carrier affects the error-vector-magnitude (EVM) of modulated signals, while the far-out noise disturbs the selectivity by the reciprocal mixing of unwanted signals to the channel.

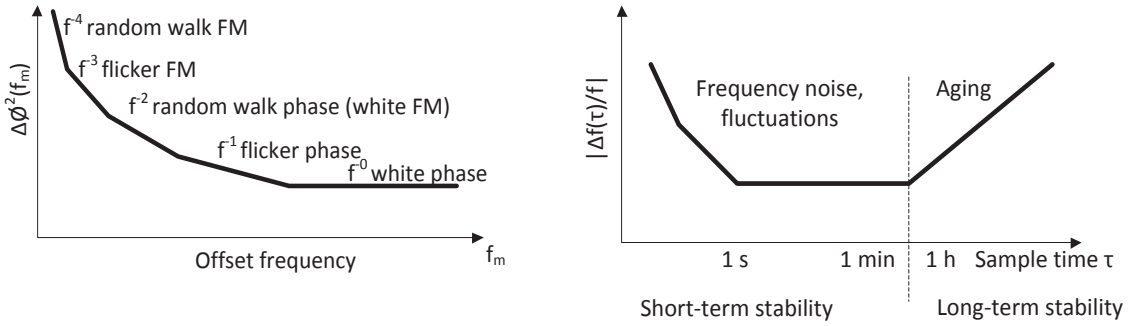

Figure 2-1 (a) SSB-spectrum of a signal with phase noise. (b) Performance versus time.

2.2 System aspects

The increased need for data capacity, e.g., in the microwave backhaul, demands an improved spectral efficiency. The available channel bandwidth limits the maximum number of symbols per second transmitted on a microwave carrier. The spectral efficiency is improved by coding each symbol by a larger number of bits as is illustrated in constellation plots in Figure 2-2 for modulation format of 2 bits and 10 bits, respectively.

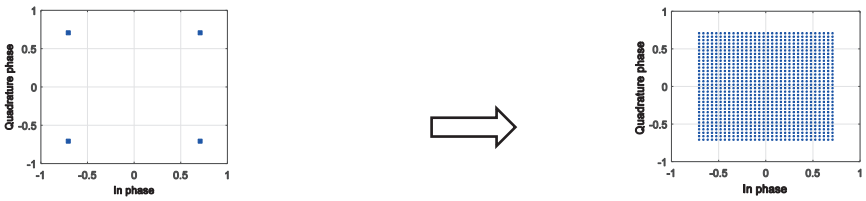

Figure 2-2 Example of Quadrature Amplitude Modulation (QAM). (a) 4-QAM. (b) 1024-QAM.

Figure 2-3 (a) and (b) show a 16-QAM signal with additive Gaussian white noise (AWGN), and with both AWGN-noise and phase noise, respectively. The constellation points in the latter case are significantly distorted and the detection margins are reduced.

Figure 2-3 (a) 16-QAM with AWGN noise. (b) 16-QAM with AWGN noise and phase noise.

The more complex the modulation scheme, the more sensitive the system is to imperfections in the radio transport, as rain, multi-path fading, etc. Furthermore, the spectral purity degrades due to imperfections such as noise in the receiver and nonlinearities in the transmitter. The receiver requires a certain signal-to-noise ratio (SNR) to minimize failures in signal detection. In particular, the phase noise in the frequency conversion of the radio chain is crucial and the signal sources are not allowed to fluctuate in frequency over time. Figure 2-4 illustrates the impact of phase noise on the measured capacity in Mbit/s for a radio link as a function of the constellation format of 2 to 11 bits, corresponding to 4-QAM to 2048-QAM, and channel bandwidth.

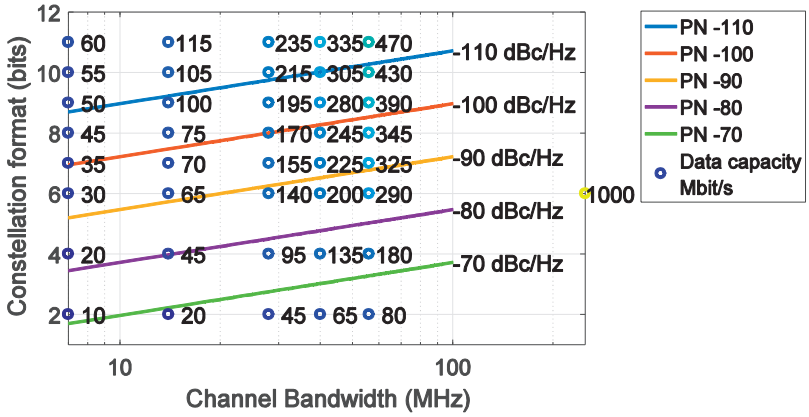

Figure 2-4 Measured channel capacity on a radio link in Mbits/s, plotted versus constellation format and channel bandwidth. The guided lines show different phase noise requirements at 100 kHz offset that must be fulfilled. The plot is valid for a constant SNR for the signal detection [24].

In reality, phase noise limits the available modulation for a certain bandwidth. Figure 2-4 presents boundaries indicating what modulation format that can be used for a given phase noise, signal bandwidth and capacity. The contours of the phase noise requirement indicate that performance for low offset frequency as 100 kHz is less dominating for a broadband signal. For broadband signals, the far-out noise floor is more dominant and must be kept low.

Other demands are on flexibility and reconfigurability for radio units to handle multiband, multistandard, etc. The trends go for software defined radios with generic hardware, which has to be cost effective, have low weight and size. This sets new requirements on the tuning technology in the frequency dependent parts, as for the oscillators. Tuning technologies that do not severely degrade the phase noise are necessary.

2.3 Fundamentals of oscillator design

2.3.1 Oscillator representation

An oscillator generates a periodic output signal by converting DC-power to RF-power. The oscillator contains an amplifier with a specific feedback path that at start up allows noise to grow and create a wanted signal. The noise is shaped by a highly filtering and selective positive feedback at the particularly wanted frequency, and it is amplified until it reaches saturation. In the closed loop, the gain will saturate to unity at a steady state, and the active device will only compensate for the losses in the feedback path. Signals not fulfilling the oscillation condition will be suppressed. If the oscillator suffers a transient disturbance, as pulling from a load variation, or as pushing from a change in bias supply, it will correct itself to the frequency fulfilling the oscillation condition.

The oscillator can be described either as a positive feedback system or a negative resistance (i.e., reflection amplifier) connected to a passive resonator. There are no strict differences between the two representations, and they can be used arbitrarily for representation of an oscillator. In the following chapters, there are some general characteristics of each type discussed.

Feedback oscillators

Figure 2-5 shows a positive feedback system.

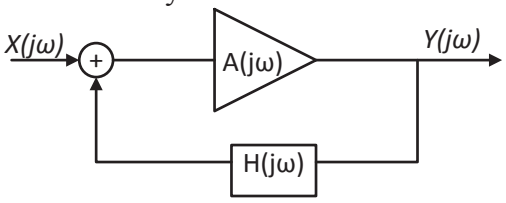

Figure 2-5. Block diagram of a feedback oscillator.

The output signal in Figure 2-5 can be expressed as

$$Y(j\omega) = X(j\omega)\frac{A(j\omega)}{1 - A(j\omega)H(j\omega)} \tag{2-1}$$

The denominator should equal zero to cause an oscillation, and following conditions must be fulfilled, the so-called Barkhausen criterion

$$|A(j\omega)H(j\omega)| > 1 \tag{2-2}$$

$$\angle A(j\omega)H(j\omega) = n360° \tag{2-3}$$

Negative resistance oscillators

Figure 2-6 shows the case of a negative resistance oscillator. In this respect, the amplifying active part is described as a one-port, with a reflection gain. The coupled resonator is also a one-port.

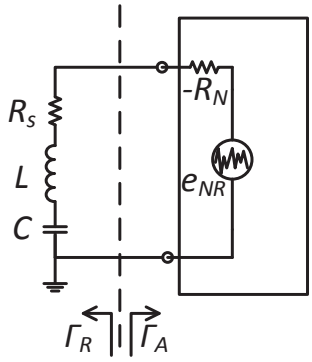

Figure 2-6. Block diagram of a negative resistance oscillator.

To fulfill the oscillation conditions, following expressions must be fulfilled, equally to the feedback system.

$$|\Gamma_R\Gamma_A| > 1 \tag{2-4}$$

$$\angle\Gamma_R\Gamma_A = n360° \tag{2-5}$$

Topology

A negative resistance can be illustrated from a simple FET-model as in Figure 2-7 (a). In Figure 2-7 (b), the gate terminal is grounded, and a negative resistance appears on the drain terminal, which is derived in (2-6) to (2-8).

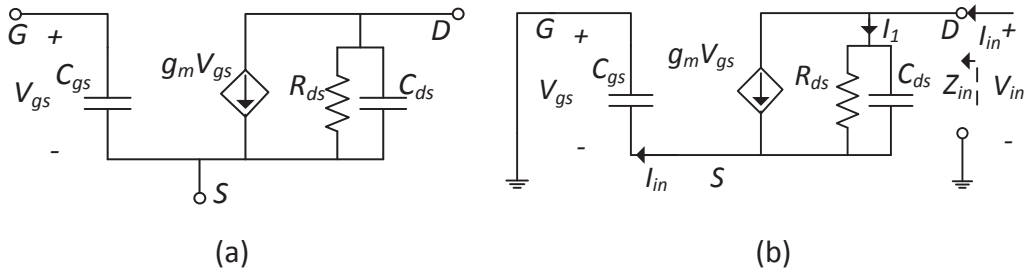

Figure 2-7 (a) FET-model. (b) FET with grounded gate.

Following expression can be extracted from Figure 2-7 (b)

$$V_{in} = I_1\left(\frac{R_{ds}}{j\omega R_{ds}C_{ds}+1}\right) - V_{gs} = \left(I_{in} - g_m V_{gs}\right)\left(\frac{R_{ds}}{j\omega R_{ds}C_{ds}+1}\right) - V_{gs} \tag{2-6}$$

$$V_{in} = I_{in}\left(1 + \frac{g_m}{j\omega C_{gs}}\right)\left(\frac{R_{ds}}{j\omega R_{ds}C_{ds}+1}\right) + \frac{I_{in}}{j\omega C_{gs}} \tag{2-7}$$

and if $R_{ds} \gg 1/\omega C_{ds}$, the expression is simplified to

$$Z_{in} = \frac{V_{in}}{I_{in}} = \frac{1}{j\omega C_{gs}} + \frac{1}{j\omega C_{ds}} - \frac{g_m}{\omega^2 C_{gs}C_{ds}} \tag{2-8}$$

which shows a negative resistance combined with a serial coupling of C_{gs} and C_{ds}.

As previously mentioned there is an analogy of seeing the oscillator as a feedback type or as a reflection type. Figure 2-8 demonstrates an example, where different groundings are used and, consequently, the view of the feedback paths is changed. The bias networks are not shown. Figure 2-8 (a) shows a feedback path of an 180-degree π-filter connecting the amplified signal back to input in a common emitter configuration. Figure 2-8 (b-c) shows the same design, but with the ground reference moved to the base side. Figure 2-8 (c) is equivalent with a common-base Colpitts oscillator. Finally, Figure 2-8 (d) shows a break-up of the resonator formed by an inductor connected to the capacitance network, principally defined by C_1 and C_2 in serial [25]. The latter network is similar to the transistor circuit in Figure 2-7 (b), and it will have a negative resistance into the collector, according to (2-8). If the intrinsic capacitances are neglected, the real part of the impedance is negative as a function of the transistor transconductance, $\text{real}(Z_{in}) = -g_m/(C_1C_2\omega^2)$, which enables oscillation.

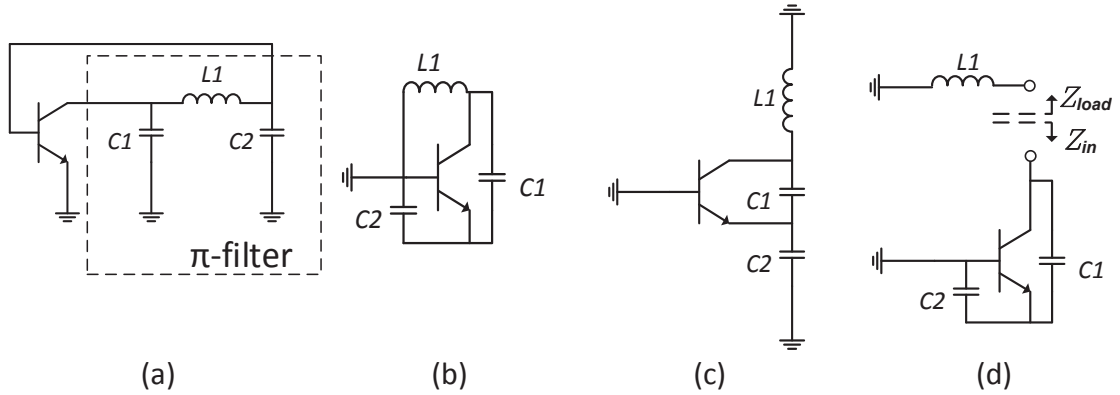

Figure 2-8 (a) Feedback by an 180-degree π-filter. (b-c) different grounding, a.k.a common-base Colpitts. (d) The resonator is broken-up in an inductor and a capacitive network with a negative resistance.

Further, the capacitive part in Figure 2-8 (d) can be out-phased with a transmission length to achieve a pure negative resistance. In this case, a high-Q resonator can be connected.

2.3.2 Active part including noise generation

Noise sources in semiconductor devices

The active device has a central role for the phase noise around the carrier. The device noise floor and the low-frequency noise (LFN) will due to up-conversion in the oscillation process create phase noise. This can be minimized by choosing a proper device technology.

There are two main types of transistors, the field effect transistor (FET) and the bipolar transistor (BJT). The first type is characterized of a conductive channel controlled by an electric field, while the latter type is bipolar and has two PN-junctions of charge carriers of electrons and holes. An example of FET is the high electron mobility transistor (HEMT). Common substrate technologies for HEMTs are GaN and GaAs. Examples of bipolar transistors are the heterojunction bipolar transistors (HBT) that commonly are processed in materials like GaAs, InGaP or SiGe. Typically, HEMTs have lower high-frequency noise level, but higher noise at low frequencies than the bipolar transistors.

Without going into details of semiconductor physics, following parts of the chapter will describe how the noise sources impact on phase noise in the oscillator application. Most focus is on the internal noise figures of the transistors. Other effects as the power capability of creating a better signal-to-noise-ratio, the drain efficiency and the linearity, are discussed for the oscillator designs in Chapter 4.

The noise sources with the most impact on oscillator phase noise coming from the active parts are thermal noise, shot noise, flicker noise and generation-recombination (GR) noise.

Thermal noise

Thermal noise described as white Gaussian noise has no bias dependence. The resistance of the circuit and its equivalent noise temperature determines the level of the noise floor. Thermal noise was investigated by Nyquist and Johnson [26], [27]. The noise is a distribution of voltages and currents in a network due to the thermal electron agitation, called Brownian motion. It can be modeled as

$$\frac{< i_{n,th}^2 >}{\Delta f} = \frac{4kT}{R} \tag{2-9}$$

where R is the circuit resistance, and T the physical temperature or an equivalent noise temperature and Δf the bandwidth.

Shot noise

The discrete nature of charge flow can generate shot noise, because of the emission of charge carriers across a potential barrier, and it is therefore contributed in bipolar devices. It is a white and frequency independent noise, which increases with bias current. It can be modeled as,

$$\frac{< i_{n,s}^2 >}{\Delta f} = 2qI_{DC} \tag{2-10}$$

where I_{DC} is the bias current, and q is the elementary charge.

Flicker noise

The conductance of semiconductors and metals can fluctuate in time and produce flicker noise. The reason for this is variation in the number of charge carriers and mobility in the presence of a DC-current. It is thus dependent on the bias current and the frequency. Models of flicker noise are presented in [16] and [17]. The flicker noise can be mathematically expressed as

$$\frac{< i_{fl}^2 >}{\Delta f} = \frac{K_f I_{DC}^{A_f}}{f^{F_{fe}}} \tag{2-11}$$

where the flicker noise coefficients K_f, A_f, and F_{fe}, are used to curve fit measured data, while f is the frequency.

Generation-Recombination (GR)-noise

Fluctuations in the number of free carriers cause this kind of noise, where the carrier concentration typically can vary over several orders of magnitude. The noise may appear in transitions between the conduction band and other energy levels in the energy gap, in the conduction band or valence band, etc. GR-noise depends on bias current and frequency as

$$\frac{< i_{n,gr}^2 >}{\Delta f} = \frac{K_b I_{DC}^{A_b}}{1 + \left(\frac{f}{f_b}\right)^2} \tag{2-12}$$

where I_{DC} is the bias current, K_b and A_b are fitting parameters. Frequency f is related to frequency f_b when GR-centers are activated [28].

The noise sources occur differently in a HEMT or a BJT. Figure 2-9 shows a noise model of a HEMT with a representation of their main noise sources. The gate resistance and drain resistance contribute most to thermal noise. Flicker noise and GR-noise appear across the channel, and they are represented as noise sources on the gate and the drain.

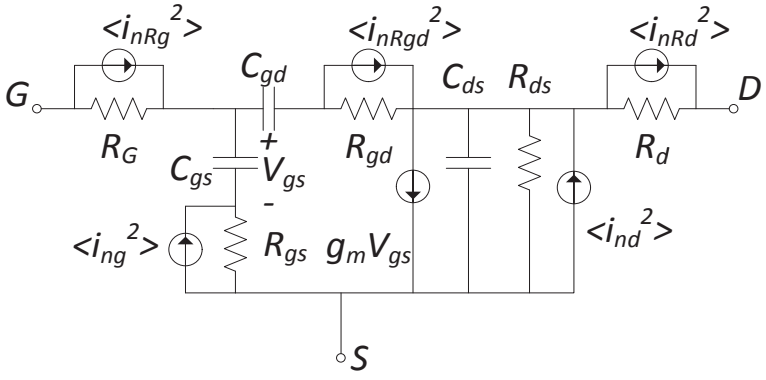

(a)

Thermal noise:

$$< i_{nRg}^2 >= \frac{4kT}{R_G}\Delta f \qquad < i_{nRd}^2 >= \frac{4kT}{R_d}\Delta f$$

$$< i_{nRgd}^2 >= \frac{4kT}{R_{gd}}\Delta f$$

Flicker noise and GR-noise:

$$< i_{ng}^2 >= \frac{K_{1f} I_G^{A_{1f}}}{f^{F_{1fe}}}\Delta f + \frac{K_{1b} I_G^{A_{1b}}}{1+\left(\frac{f}{f_{1b}}\right)^2}\Delta f$$

$$< i_{nd}^2 >= \frac{K_{2f} I_D^{A_{2f}}}{f^{F_{2fe}}}\Delta f + \frac{K_{2b} I_D^{A_{2b}}}{1+\left(\frac{f}{f_{2b}}\right)^2}\Delta f$$

(b)

Figure 2-9 (a) Noise model of a HEMT with corresponding main noise sources [29]. (b) Expressions of the noise sources.

For a BJT, thermal noise appears due to the base resistance. Shot noise appears in the junction between the collector and the base. Figure 2-10 shows a noise model of a BJT with their corresponding main noise sources.

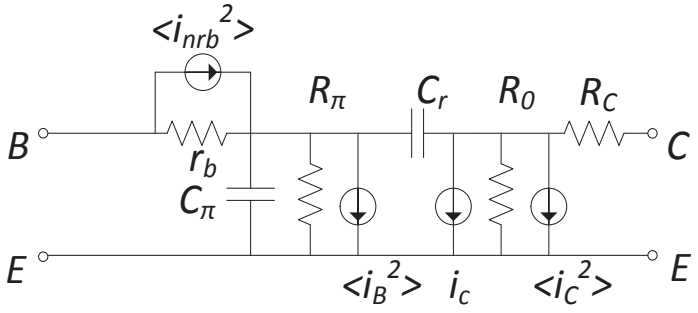

(a)

Thermal noise:	$< i_{nrb}^2 >= \frac{4kT}{r_b}\Delta f$
Shot noise:	$< i_C^2 >= 2qI_c\Delta f$
Shot noise, flicker noise and GR noise:	$< i_B^2 >= 2qI_B\Delta f + \frac{K_{1f}I_B^{A_{1f}}}{f^{F_{1fe}}}\Delta f + \frac{K_{1b}I_B^{A_{1b}}}{1+\left(\frac{f}{f_b}\right)^2}\Delta f$

(b)

Figure 2-10 (a) Noise model of a BJT with corresponding main noise sources [30]. (b) Expressions of the noise sources.

Flicker noise and GR-noise have a dominant low-frequency (LF) behavior. LFN-measurement is important in device characterization as it can reveal imperfections in the semiconductor process. Some imperfections can cause traps and surface states for the electrons, which lead to LFN. LFN-measurement is commonly used for benchmarking the technology. The phase noise close to the carrier in oscillators is dependent on LFN which is up-converted in the oscillation process.

The amount of LFN varies with transistor technology. A commonly used parameter is the flicker noise corner-frequency, f_c, which defines the frequency where the LFN has the same magnitude as the white noise floor. It should be mentioned that there are uncertainties to estimate the device noise floor as the measurement noise floor also contributes. Devices with high RF-noise figure can by this definition get a lower flicker noise corner-frequency. This argues to handle this parameter carefully. The flicker noise corner-frequency is illustrated in Figure 2-11. Vertical structures like HBTs generally have lower LF-noise than FETs and HEMTs which are more exposed in the surface. Traps and surface states for the electrons are more frequent in laterally structured devices. For example, InGaP/GaAs HBTs have LF corner-frequencies of about 20 kHz, while in the case of GaN-HEMT it can be about 1 MHz. The lower estimated flicker noise corner frequency for bipolars can also be due to the higher shot noise in these devices. Paper [H] presents detailed LFN measurements comparing different transistor technologies.

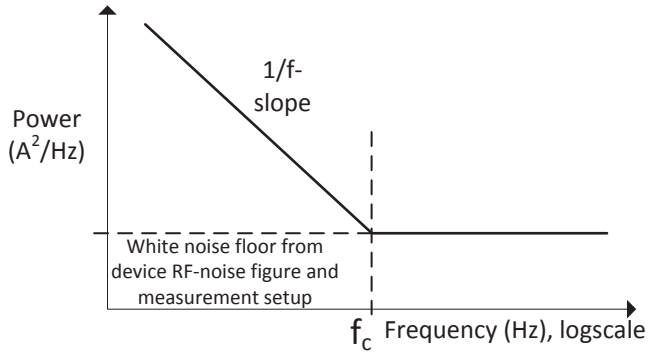

Figure 2-11. Low-frequency noise and the device noise floor combined with the measurement system noise floor.

The choice of the active part depends on where the noise performance is most critical to optimize. A trade-off between low flicker-noise and low noise floor compared to the power of the carrier is often necessary. Figure 2-12 shows an illustration of phase noise profiles

for typically sized and biased GaN-HEMTs and silicon BJTs, respectively, with a resonator in PCB-technology (Q≈100). GaN devices used in this study are beneficial for their low noise floor far out, and their high power efficiency and power capability perform an excellent signal-to-noise ratio. The drawbacks of the higher flicker noise compared to other technologies will become less important for broadband signals that are expected in future communication systems. The targeting application for broadband communication in this study identifies the noise floor as most critical [19]. In this perspective GaN-technology would be a good choice.

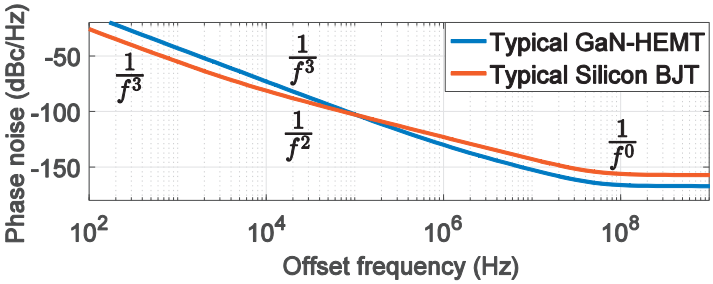

Figure 2-12 Typical phase noise profiles with frequency slope stated for GaN-HEMT with high flicker noise compared to silicon BJTs with less flicker noise but with higher noise floor with a resonator on PCB.

2.3.3 Resonator

Q-factor of the resonator

Passive circuits forming the resonator in an oscillator are often characterized and benchmarked regarding a quality factor (Q-factor). In a resonator, the energy alternates between electrically and magnetically stored energy. The Q-factor of a resonator can be expressed as the ratio between stored energy and the energy loss per cycle, i.e., average power loss,

$$Q_{def} = 2\pi \frac{\text{Stored energy}}{\text{Energy dissipation per cycle}} = \omega \frac{\text{Stored energy}}{\text{Average power loss}}$$

The magnetic energy W_m is maximized when the electrical energy W_e is zero and vice versa, i.e., $W_{stored} = W_{e,peak} = W_{m,peak}$. Measurement of the Q-factor according to the general definition is quite impractical, and it is often necessary to use some of the following derived methods. The first method is using the 3 dB bandwidth of the frequency response of the power transmission, or the power reflection at the center frequency ω_0.

$$Q = \frac{\omega_0}{\Delta\omega_{3dB}} \tag{2-13}$$

Another relation is the phase slope of the input impedance. For a parallel resonator,

$$Q = -\frac{\omega_0}{2} \frac{\partial \phi(Z_p)}{\partial \omega}\bigg|_{\omega=\omega_0} \tag{2-14}$$

For a serial resonator the phase slope shifts sign, and the quality factor can be expressed

$$Q = \frac{\omega_0}{2}\frac{\partial \emptyset(Z_s)}{\partial \omega}\Big|_{\omega=\omega_0} \tag{2-15}$$

If an electrical model of the resonator is used, the Q-factor of the resonator can be calculated directly from the component values,

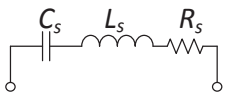

$$Q = \frac{\omega_0 L_s}{R_s} = \frac{1}{\omega_0 C_s R_s} \tag{2-16}$$

(a) Serial resonance

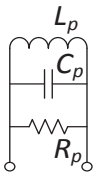

$$Q = \frac{R_P}{\omega_0 L_P} = \omega_0 C_P R_P \tag{2-17}$$

(b) Parallel resonance

Figure 2-13 (a) Schematics of a serial resonance circuit and (b) a parallel resonance circuit.

Loaded Quality factor

When resonators are not connected or very weakly connected to a load, they are characterized by the unloaded Q-factor, Q_0. In reality, this metric is often impractical, as resonators always have to be connected to some device injecting power into it, or to couple out a wanted signal from it. In the case of an oscillator, this means that it must connect to an active device, thus be loaded by its internal resistance. This load network can also be characterized by an external Q-factor, Q_{ext}. The total loaded Q-factor, Q_L, for the network is then calculated as

$$\frac{1}{Q_L} = \frac{1}{Q_0} + \frac{1}{Q_{ext}} \tag{2-18}$$

Design impact

The unloaded quality factor, Q_0, of a resonator is of importance for effective filtering with high frequency selectivity, that will shape the noise around the carrier. Dependent on the building practice, different types of resonators are used, e.g., dielectric resonators as used in DROs, metal cavities, lumped components, distributed transmission lines as resonant stubs and crystals. The technology choice is affected by the Q-factor needed, power handling of the resonator, frequency tunability, etc.

Table 2-1 Example of Q-factor in different technologies [1],

Example of resonator	Unloaded Q-factor (Q_0) Typical values	Frequency (GHz) Typical values
DR (dielectric resonator)	10 k-25 k	<50
YIG (yttrium-iron-garnet)	1 k-10 k	<50
Cavity aluminum (without silver plating)	3000	<40
Microstrip on low loss PCB	100	<40
Lumped LC	100-300	<10
MMIC (III-V-substrate)	40	<100

There are some considerations to design an oscillator and to utilize the resonator and the Q-factor in an optimum way.

- The phase condition for the closed loop, $n360^{\circ}$, should occur for maximum phase slope $(\partial\emptyset(Z)/\partial\omega)$. This is further discussed when tunability is added in Chapter 2.6.
- The coupling of the resonator to the active device will decrease the total loaded Q-factor, Q_L, with a negative impact on phase noise, which is contradictory to that high power coupled to the resonator is beneficial. An optimum coupling exists which is discussed in Chapter 2.5.

2.4 Phase noise models

Modeling phase noise has been continuing for several decades and is still not a completely understood research area. The complexity depends on the nonlinear way the noise from different sources is up-converted around the carrier, which differs from the linear noise figures in example amplifiers. Besides the linearity aspects, there are considerations about modeling the noise sources as stationary and time-invariant sources, or as time-variant meaning that they will depend on the current and voltage trajectory waveform across the transistor. The latter approach implies a cyclo-stationary model. Limiting to the linear theory, the two most used models are the linear time-invariant model (LTI) by Leeson [9], and the linear time-variant model (LTV) by Hajimiri [18]. In this study, we have focused on the time-invariant linear models only for the study of optimizing the resonator coupling, power handling and noise figures of the active device. The limitation is that the up-conversion of flicker noise will not be accurately modeled [31], as it is in a cyclo-stationary process where the noise level is dependent of the current waveform across the transistor. Phase noise far out is less dominated by flicker noise and will be predicted fairly well by the time-invariant models originated from Leeson.

2.4.1 A linear theory of phase noise

A general feedback oscillator system can be described as [25].

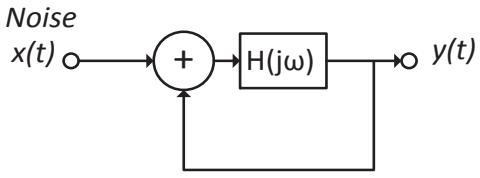

Figure 2-14 General oscillator feedback system

The transfer function can be written as

$$\frac{Y(j\omega)}{X(j\omega)} = \frac{H(j\omega)}{1 - H(j\omega)} \tag{2-19}$$

The Taylor expansion around the oscillation frequency (ω_0) can be expressed as

$$H(j\omega) \approx H(j\omega_0) + \Delta\omega \frac{dH}{d\omega} \tag{2-20}$$

where at resonance $H(j\omega_0) = 1$ and for small offset frequencies $\Delta\omega$, $|\Delta\omega\, dH/d\omega| \ll 1$, the following expression can be written

$$\frac{Y}{X}(\omega_0 + \Delta\omega) \approx \frac{-1}{\Delta\omega \frac{dH}{d\omega}} \tag{2-21}$$

The power ratio can be expressed as

$$\left|\frac{Y}{X(\omega_0 + \Delta\omega)}\right|^2 = \frac{1}{(\Delta\omega)^2 \left|\frac{dH}{d\omega}\right|^2} \tag{2-22}$$

The forward function in the loop can be assumed on the form

$$H(\omega) = |H|e^{j\emptyset} \tag{2-23}$$

This is equal to the impedance transfer function for a simple LC-network and following expression can be written

$$\frac{dH}{d\omega} = \left[\frac{d|H|}{d\omega} + j|H|\frac{d\emptyset}{d\omega}\right] e^{j\emptyset} \tag{2-24}$$

The squared absolute value can be expressed as

$$\left|\frac{dH}{d\omega}\right|^2 = \left|\frac{d|H|}{d\omega}\right|^2 + \left|\frac{d\emptyset}{d\omega}\right|^2 |H|^2 \tag{2-25}$$

For standard LC-oscillators $|d|H|/d\omega|^2$ is much smaller than $|d\emptyset/d\omega|^2$. Furthermore, $|H|$ is close to unity at stationary oscillation. By using these simplifications and inserting (2-25) in (2-22), the ratio Y and X can be reformulated as

$$\left|\frac{Y}{X}(\Delta\omega)\right|^2 = \frac{\omega_0^2}{4(\Delta\omega)^2} \frac{1}{\left[\frac{\omega_0}{2}\frac{d\emptyset}{d\omega}\right]^2} = \frac{1}{4Q_L^2}\left(\frac{\omega_0}{\Delta\omega}\right)^2 \tag{2-26}$$

The definition of the loaded Q-factor according to (2-15) is inserted. Under the assumption that the noise power at input before the active device is $|X(j\omega)|^2 = kT$, the filtered noise expression becomes

$$|Y(\Delta\omega)|^2 = \frac{kT}{4Q_L^2}\left(\frac{\omega_0}{\Delta\omega}\right)^2 \tag{2-27}$$

The expression can be normalized to the carrier signal power built up in the same node, i.e., at the node for the power before the active device, P_{in}. If a single-sideband signal is considered, the noise level can be reduced to half of the value, and the noise-to-signal power ratio for offset frequency f_m can be expressed as

$$\mathcal{L}(f_m) = \frac{|Y(\Delta\omega)|^2}{2P_{in}} = \frac{kT}{2P_{in}}\left(\frac{f_0}{2Q_L f_m}\right)^2 \tag{2-28}$$

2.4.2 Leeson's equation

Leeson used the linear phase noise theory and incorporated additional parameters for flicker noise corner f_{1/f^3}, the noise floor, and an empirical noise figure F to (2-28), and expressed the phase noise as [9]

$$\mathcal{L}(f_m) = 10\log_{10}\left[\frac{FkT}{2P_{in}}\left[1+\left(\frac{f_0}{2Q_L f_m}\right)^2\right]\left[1+\frac{f_{1/f^3}}{f_m}\right]\right] \tag{2-29}$$

which shows the normalized single-sideband for an offset frequency f_m. Leeson originally formulated an expression with respects to a feedback oscillator where the power P_{in} denotes the power at the input of the amplifier after the loss in the resonator. At optimum resonator coupling, $Q_L/Q_0 = 1/2$, which later will be derived, the power dissipated in the resonator P_r is half of the total power dissipated in the loop P_{RF}, or in other words, twice the power transmitted by the resonator thus $P_r = 2P_{in}$. The power at the resonator input is equal to the output of the amplifier, which is equal to the input power of the amplifier multiplied by its power gain, thus $P_{out} = G_A P_{in} = 4P_{in} = 2P_r$. The power gain is calculated from the gain needed for oscillation, $G_A = 1/|1 - Q_L/Q_0|^2$. The discussed power level in the feedback loop is illustrated in Figure 2-15 [32].

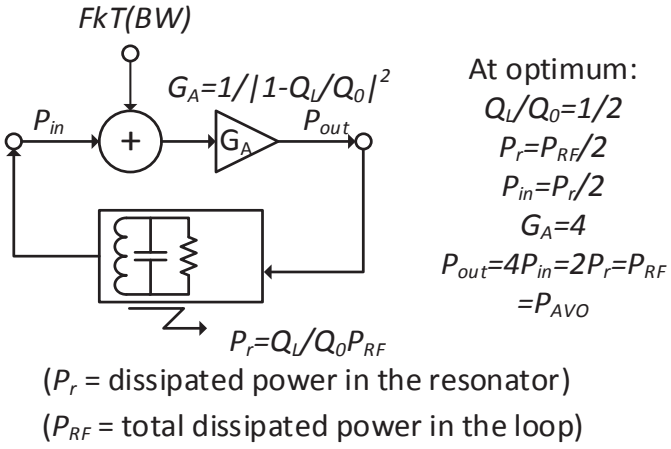

Figure 2-15 Power levels in the loop

Using power dissipated in the resonator, the single-sideband phase noise can be expressed as

$$\mathcal{L}(f_m) = 10\log_{10}\left[\frac{FkT}{P_r}\left[1+\left(\frac{f_0}{2Q_L f_m}\right)^2\right]\left[1+\frac{f_{1/f^3}}{f_m}\right]\right] \tag{2-30}$$

Alternatively, if the power at the amplifier output is used, the same single-sideband phase noise can be expressed as

$$\mathcal{L}(f_m) = 10\log_{10}\left[\frac{2FkT}{P_{out}}\left[1+\left(\frac{f_0}{2Q_L f_m}\right)^2\right]\left[1+\frac{f_{1/f^3}}{f_m}\right]\right] \tag{2-31}$$

Figure 2-16 (a-b) illustrate the empirical model for different cases: for a high Q_L-factor, a low Q_L-factor, compared to the f_{1/f^3}-factor.

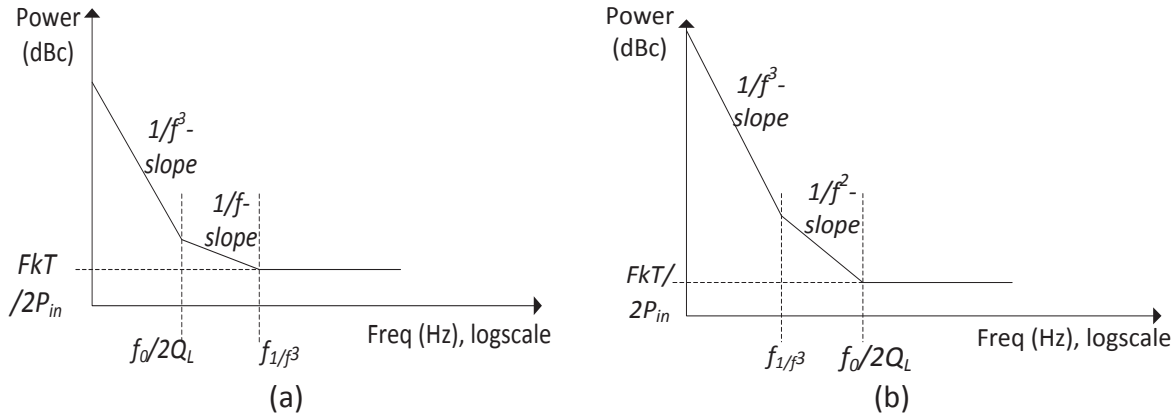

Figure 2-16 (a) Phase noise behavior, where the resonator bandwidth due to high Q falls inside the flicker noise corner, $f_{1/f3}$. (b) Phase noise behavior, where the bandwidth due to low Q falls outside the flicker noise corner.

The single-sideband phase noise floor given by the $\mathcal{L}_{floor} = FkT/2P_{in}$ is discussed in [33]. The noise level of -177 dBc/Hz for a 0 dBm signal has been verified in experiments [34]. The reason for half of the thermal noise energy relatively the carrier is explained by the definition of single-sideband [32]. Within the resonator bandwidth $f_m = f_0/2Q_L$, the amplitude noise is suppressed by amplitude compression, but the far-out noise floor is contributed by both phase and amplitude noise in equilibrium [35].

2.4.3 Everard's model

Everard expressed the phase noise in a closed form as a function of coupling factor regarding the quote Q_L/Q_0 for feedback type oscillators. For the optimum coupling condition, the minimum phase noise is expressed both for feedback type and for a reflection type or a negative resistance type oscillator.

Feedback type oscillator

A phase noise model according to [36], [23] is described as

$$\mathcal{L}(f_m) = 10\log_{10}\left[A\frac{FkT}{8(Q_0)^2(Q_L/Q_0)^2(1-Q_L/Q_0)^N P}\left(\frac{f_0}{f_m}\right)^2\right] \tag{2-32}$$

where for the cases 1-3:

1. N=1 and A=1 if P=P_{RF} and R_{OUT}=0, i.e. P is power dissipated in both resonator and the internal resistance R_{IN}, in Figure 2-17.
2. N=1 and A=2 if P=P_{RF} and R_{OUT}=R_{IN}, i.e. P is power dissipated in both resonator and the internal resistances, R_{OUT}, and R_{IN} in Figure 2-17.
3. N=2 and A=1 if P=P_{AVO} and R_{OUT}=R_{IN}, i.e. P is the available power from the amplifier at the output terminated in a matched load in Figure 2-17.

Case 2 can be used with P=P_{RF}, R_{OUT}=R_{IN} for the optimum resonator coupling of Q_L/Q_0=1/2 which is derived in 2.5.1.

The quote is corresponding to $P_r=P_{RF}/2$ (power dissipated only in the resonator), and it can be evaluated to an expression for minimum phase noise for a feedback oscillator as

$$\mathcal{L}(f_m) = 10\log_{10}\left[\frac{FkT}{{Q_0}^2 P_r}\left(\frac{f_0}{f_m}\right)^2\right] \tag{2-33}$$

which is the same as stated in (2-28) for $Q_0=2Q_L$ and $P_r = 2P_{in} = P_{AVO}/2$.

Negative resistance type oscillator

The minimum phase noise for a reflection type oscillator is in [21] derived to

$$\mathcal{L}(f_m) = 10\log_{10}\left[\frac{FkT}{2{Q_0}^2 P_r}\left(\frac{f_0}{f_m}\right)^2\right] \tag{2-34}$$

where P_r is representing the power dissipated only in the resonator.

2.5 Resonator coupling

Physical boundaries as the resonator Q-factor, the device noise factor and power capability are important figures as earlier discussed. Important is also to find a proper coupling between the resonator and the active device. This chapter shows the derivation of the optimum coupling in detail from [8], [37], [32], [38]. The theory assumes only thermal noise with Q-multiplication effect which is valid close to the phase noise skirts. Other optimums are found if flicker-noise is considered, and furthermore, a different optimum is found when minimizing the far out noise. Also, the system noise figure, *F*, is assumed to be constant (versus different impedance) during this optimization.

2.5.1 A theory of resonator coupling

Feedback oscillator

Figure 2-17 depicts a model of a feedback type oscillator.

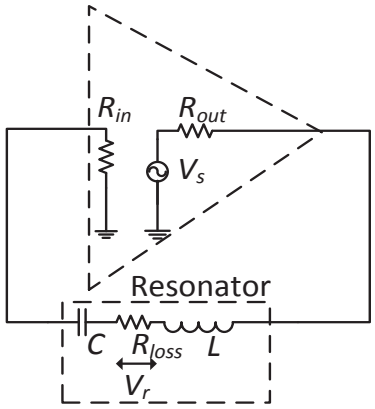

Figure 2-17. Model of a feedback oscillator.

If $R_{in} = R_{out} = Z_0$ is assumed, the following expression can be written for the loaded Q-factor

$$Q_L = \frac{\omega L}{R_{Loss} + R_{in} + R_{out}} = \frac{\omega L}{R_{Loss} + 2Z_0} = Q_0 \left(\frac{1}{1 + \frac{2Z_0}{R_{Loss}}} \right) \tag{2-35}$$

The ratio to the unloaded Q-factor is calculated by defining a coupling factor β as

$$\frac{Q_L}{Q_0} = \left(\frac{1}{1 + \frac{2Z_0}{R_{Loss}}} \right) = \frac{1}{1 + \beta} \tag{2-36}$$

The rms-voltage over the resonator can be expressed as

$$V_r = V_s \frac{R_{Loss}}{R_{Loss} + 2Z_0} = V_s \frac{Q_L}{Q_0} \tag{2-37}$$

Maximum available power from the amplifier at output can be expressed as

$$P_{avo} = \frac{{V_s}^2}{2 \cdot 2Z_0} \tag{2-38}$$

and the power dissipated inside the resonator is formulated when inserting (2-37) and (2-38) as

$$\begin{aligned} P_r = \frac{{V_r}^2}{R_{Loss}} = \frac{{V_s}^2 {Q_L}^2}{{Q_0}^2 R_{Loss}} = \frac{P_{avo} 4Z_0}{R_{Loss}} \left(\frac{Q_L}{Q_0} \right)^2 = 2P_{avo} \left(\frac{Q_0}{Q_L} - 1 \right) \left(\frac{Q_L}{Q_0} \right)^2 \\ = 2P_{avo} \frac{Q_L}{Q_0} \left(1 - \frac{Q_L}{Q_0} \right) \end{aligned} \tag{2-39}$$

If (2-39) is inserted in (2-32) for case 3, the best phase noise is achieved when maximum power is dissipated in the resonator. The optimum in terms of Q_L/Q_0 is when [21]

$$\frac{Q_L}{Q_0} = \frac{1}{2} \tag{2-40}$$

or if considering the insertion loss expression,

$$S_{21} = (1 - \frac{Q_L}{Q_0}) \tag{2-41}$$

An interpretation of this is that half of the available power is dissipated in the resonator, one quarter is reflected, and one quarter is transmitted (=$|S_{21}|^2$) which was illustrated in

Figure 2-15. The best phase noise according to Everard's model (2-32) for the feedback case with R_{in}=R_{out}, can be summarized to

$$\mathcal{L}(f_m) = \frac{2FkT}{P_{avo}{Q_0}^2}\left(\frac{f_0}{f_m}\right)^2 \tag{2-42}$$

or equivalently expressed in the dissipated power in the resonator

$$P_r = \frac{{V_r}^2}{R_{Loss}} = \frac{P_{avo}}{2} \tag{2-43}$$

The phase noise is calculated to

$$\mathcal{L}(f_m) = \frac{FkT}{P_r{Q_0}^2}\left(\frac{f_0}{f_m}\right)^2 \tag{2-44}$$

which is the same expression as given in (2-33).

Negative resistance oscillator

Figure 2-18 depicts a model of a reflection type oscillator.

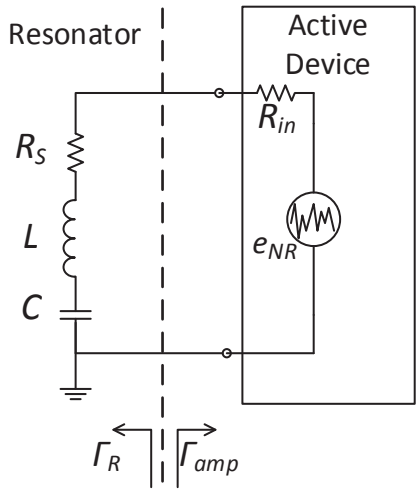

Figure 2-18 Model of a reflection oscillator.

The amplifier is modeled with an internal resistance R_{in}, and a voltage noise source. The loss resistance in the cavity is described by R_S. The ratio of loaded and unloaded quality factor according to (2-36) can be expressed as

$$\frac{Q_L}{Q_0} = \frac{R_s}{R_s + R_{in}} = \frac{1}{1 + \frac{R_{in}}{R_s}} = \frac{1}{1+\beta} \tag{2-45}$$

An expression of the phase noise using (2-32) with $P = P_{RF}$, R_{OUT}=0, i.e., case 1 for power dissipated in both the resonator and in the internal resistance in the amplifier R_{in}, is stated

below. The circuit may be seen as a one-port with one port grounded, according to [21], [39],

$$\mathcal{L}(f_m) = \frac{FkT}{8(Q_0)^2(Q_L/Q_0)^2(1-Q_L/Q_0)P_{RF}}\left(\frac{f_0}{f_m}\right)^2 \tag{2-46}$$

The equation simplifies when inserting (2-36) in (2-46) to

$$\mathcal{L}(f_m) = \frac{FkT}{8(Q_0)^2\beta/(1+\beta)^3 P_{RF}}\left(\frac{f_0}{f_m}\right)^2 \tag{2-47}$$

It can be shown with differentiation that (2-47) will have a minimum value for

$$\beta = \frac{1}{2} \tag{2-48}$$

or equivalently,

$$\frac{Q_L}{Q_0} = \frac{2}{3} \tag{2-49}$$

This means that the power dissipated in the resonator is $P_r = 2/3P_{RF}$. If the expression is inserted in (2-47), it will evaluate the optimum phase noise value as [37], [21],

$$\mathcal{L}(f_m) = \frac{9FkT}{16P_r{Q_0}^2}\left(\frac{f_0}{f_m}\right)^2 \tag{2-50}$$

Equation (2-50) has been derived from the analytical expression, and it is quite similar to (2-34) using the approximate derivation in [21]. It can be worth noting that the power dissipated inside the resonator, P_r, is only half in the negative resistance oscillator compared to the feedback oscillator for a given phase noise performance (2-44). Therefore, it is beneficial to use reflection type oscillators where the resonators are the bottleneck for power capability, as for power limited crystal resonators or for resonators tuned with power-limited varactors that will be discussed in 2.6.1.

If the power delivered from the amplifier P_{RF} is considered, the optimum value of β is used, and the efficiency is stated $P_{RF} = \eta P_{DC}$, following expression of phase noise can be written

$$\mathcal{L}(f_m) = \frac{FkT}{8(Q_0)^2\beta/(1+\beta)^3\,\eta P_{DC}}\left(\frac{f_0}{f_m}\right)^2 \tag{2-51}$$

which for optimum coupling according to (2-48) simplifies to

$$\mathcal{L}(f_m) = \frac{27}{32}\frac{FkT}{\eta P_{DC}Q_0^2}\left(\frac{f_0}{f_m}\right)^2 \tag{2-52}$$

Equation (2-52) can be used to calculate the bound on phase noise for available P_{DC}, and Q_0 from the technology.

2.5.2 Resonator coupling design impact

In this study, two possible methods to match the resonator coupling for a reflection oscillator are considered; by changing the impedance coupling to the resonator, or by changing the reflection gain of the amplifier. The following designs exemplify the two methods.

A cavity oscillator with varied resonator coupling by changing the position of the cavity from an excitation microstrip line is demonstrated in Paper [C]. The corresponding resonator resistance, R_S, and the amplifier gain for the optimum bias point $-R_N$ at the best phase noise shows the ratio $R_s/|R_N|$ is close to unity, which is further discussed in 4.2.1.

The different approach to adjust the resonator coupling $R_s/|R_N|$ by changing the gain represented by $-R_N$ of the active device is reported in Paper [D]. A reflection amplifier is used where the gain can be tuned by a passive change using varactors in its termination network without affecting the bias level of the active transistor. The oscillator with the electronical gain control is found to give about the same result as a mechanically tuned coupling factor, which is further discussed in 4.4.2.

There are published results for reflection oscillators where the optimum loss resistance in the resonator is showed for one third of the absolute value of the negative resistance from the amplifier, [40], [41] and Paper [F]. That optimum can still be applied as a good design rule. The optimum resonator coupling which is derived in (2-48) for a reflection oscillator is $\beta = 1/2$, [23]. It corresponds to the ratio of the dissipated power in the resonator to the power in the loop (P_{RF}) as $Q_L/Q_0 = 1/(1 + \beta) = 2/3$. The open loop gain is important to consider for the optimum coupling. It is found in measurement that high loop gain compression shall be avoided, due to the non-linear up-conversion of flicker noise and thermal noise, and consequently, a β close to unity, or $Q_L/Q_0 = 1/2$ is preferable. Generally, $\beta = 1/2$ to $\beta = 1$ should be considered dependent on the design condition, as due to flicker noise content, or the needed margin for start-up oscillation, etc.

The theoretical effect on phase noise for different coupling expressed in Q_L/Q_0 according to (2-46) is shown in Figure 2-19. Two different definitions of power are used for calculating the Q_L/Q_0, as the power dissipated in the loop or as available power. The usage of the available power requires a matched load, which is not necessary if dissipated power is used.

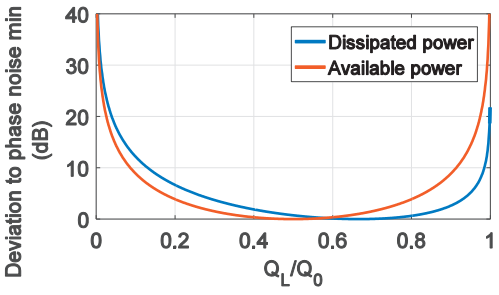

Figure 2-19 Minimum phase noise versus Q_L/Q_0 with power defined as the dissipated power in the resonator, and defined as maximum available power for a feedback type oscillator.

It can be noticed from Figure 2-19 that the deviation in phase noise between coupling factor $\beta = 1/2$, $(Q_L/Q_0 = 2/3)$ to $\beta = 1$, $(Q_L/Q_0 = 1/2)$, for constant dissipated power is about 0.7 dB for this linear model. The different coupling factors corresponds to a variation in S_{21} according to (2-41) to about 3.5 dB. In reality, when incorporating the non-linear up-conversion of noise, the difference in phase noise can be significantly larger. In Table 4-2 in 4.2.1, a phase noise variation of 5 dB is shown due to a variation of about 3.5 dB in the open loop gain.

Impact of phase condition

The phase condition of $n \cdot 360°$ is desired to be fulfilled for the frequency where the maximum phase slope occurs, thus at $\max(\partial\emptyset(Z)/\partial\omega)$ or equivalently at maximum Q-factor. If a phase error is introduced in the loop, the frequency is changed to meet the phase condition. For a feedback oscillator the phase error can be written as

$$\Delta\emptyset_{error} + \angle(S_{21}(\Delta f)) = 0 \tag{2-53}$$

and generally the transfer function versus offset Δf is rolled-off as

$$\mathrm{S}_{21}(\Delta f) = \frac{\mathrm{S}_{21}(0)}{1 + j2Q_L\frac{\Delta f}{f_r}} \tag{2-54}$$

If considering the argument of the expression of (2-54) used in (2-53), the following expression can be stated

$$\tan(\Delta\emptyset_{error}) = 2Q_L\Delta f/f_r \tag{2-55}$$

where the changed oscillation frequency $f_0 = f_r + \Delta f$ to fulfill the condition from (2-53). If no phase error, $\Delta\emptyset_{error} = 0$, the oscillation frequency is equal to the original oscillation frequency f_r.

The voltage gain in the loop can be written as [42]

$$\frac{1}{G_v} = |S_{21}(\Delta f)| = S_{21}(0)\cos^2(\Delta\emptyset_{error}) \tag{2-56}$$

The phase noise expression can be rewritten with power gain and the phase error in the open loop, $\Delta\emptyset_{error}$, consequently showing the degradation in phase noise as [42],[23],

$$\mathcal{L}(f_m, \Delta\emptyset_{error}) \propto \frac{\mathcal{L}(f_m, 0)}{\cos^4(\Delta\emptyset_{error})} \tag{2-57}$$

2.6 Frequency tuning

Frequency tuning can be achieved by changing the equivalent inductance or capacitance values that define the resonance frequency

$$f_0 = \frac{1}{2\pi\sqrt{LC}} \tag{2-58}$$

A common method uses varactors connected as part of the capacitance *C*, connected single or switched from a capacitor bank for generating several sub-bands. These elements can be integrated with the resonator circuitry to direct affect the resonance condition. Alternatively, they can be coupled externally to the resonator to change the load of the resonator or to change the phase condition.

The tuning elements can be implemented as semiconductor devices with junction capacitance or formed as digital switches of PIN-diodes with connected lumped capacitors. They can alternatively be implemented in micro-machined structures as MEMS-varactors or RF-MEMS switches, etc.

The advantage of using switched elements in combination with analog tuning within the sub-band is that the analog elements can be weakly coupled to enhance a narrow band tuning and still keep a high loaded Q-factor. The performance of the digital switches are thus important, and they are preferably implemented as low-loss switches example in RF-MEMS technology. Tuning with semiconductor varactors is described in 2.6.1 and tuning with RF-MEMS-switches in 2.6.2.

A frequency tuning by a change in the phase condition, i.e., a change in the group delay Δt_g can be written as

$$\Delta f = \frac{1}{360}\frac{\theta}{\Delta t_g} \tag{2-59}$$

and the Q as

$$Q = \pi f_0 t_g \tag{2-60}$$

The phase shift in the signal path does not degrade the Q-factor of the resonator. A disadvantage is the phase condition may not be fulfilled for the frequency corresponding to maximum phase slope of the impedance. The introduced phase error degrades the performance according to (2-57), and therefore this method is often limited to narrow-band tuning.

A wideband resonator often used in instruments is the yttrium-iron-garnet, (YIG), resonator. It consists of a high-Q ferrite of $Y_2Fe_2(FeO_4)_3$, and normally it has a spherical form that can be widely tuned by varying the DC-bias of an applied magnetic field [1]. Due to the change in the ferromagnetic resonance, the frequency can be tuned over several octaves. YIGs are commonly manufactured for center frequencies from about 500 MHz to 50 GHz, and the unloaded Q-factor is normally greater than 1000. The fabrication is quite difficult with a complex polishing and aligning process of the ferrite sphere to the coupling loop. Other drawbacks are the high DC-current consumption needed for tuning and their normally bulky solution (volume of several cm^3) with difficulties for miniaturization and integration compared to solid state semiconductor tuning elements. However, more compact solutions using planar YIG-structures have recently demonstrated successful results [43].

As previously discussed, the resonator coupling is essential for an efficient usage of the resonator to maintain a high Q-factor as well as keeping a high signal-to-noise ratio. This task becomes even more challenging for tunable resonators, where the loaded Q-factor has to remain high over a certain bandwidth with an optimum coupling factor [44]. Another

impact on the phase noise is that all tuning circuitry itself will cause modulation noise that will degrade the phase noise. The effect of modulation noise is empirically modeled by adding an extra term to Leeson's equation [45],

$$\mathcal{L}(\Delta f) = 10\log_{10}\left[\frac{FkT}{2P_s}\left[1+\left(\frac{f_0}{2Q_L\Delta f}\right)^2\right]\left[1+\frac{\Delta f_{1/f^3}}{\Delta f}\right]+\frac{K_0^2V_m^2}{8\Delta f^2}\right] \tag{2-61}$$

where besides the previously defined parameters, K_o represents tuning sensitivity (Hz/V) and V_m the voltage noise on the varactor.

2.6.1 Varactor based tuning

A varactor may be incorporated in the capacitance value in (2-58) to direct change the resonance frequency. An example of a varactor tuned serial *LC*-resonator for a negative resistance oscillator is studied in this section. The negative resistance, $-R_N$ represents the transistor gain, and R_S represents the resonator loss. For a steady state $-R_N + R_s = 0$. A tuning capacitor, i.e., varactor, is added in serial with the resonator as in Figure 2-20, and the varactor loss resistance R_V is incorporated in the total loss of the resonator when dimensioning the coupling factor.

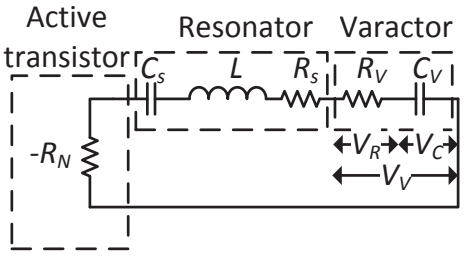

Figure 2-20 Schematic of a reflection oscillator with series varactor [32].

The oscillation frequency is expressed by

$$f_0 = \frac{1}{2\pi}\sqrt{\frac{C_s+C_v}{LC_sC_v}} = \frac{1}{2\pi}\sqrt{\frac{1}{LC_v}\frac{P_sQ_s}{P_vQ_v}} \tag{2-62}$$

where P_s is the total power dissipated in the resonator, and P_v is the power dissipated in the varactor. The quality-factor for the complete resonator, i.e., the loss in the resonator compared to the total capacitance in the resonator, is given by,

$$Q_s = \frac{C_s+C_v}{\omega_0 R_s C_v C_s} \tag{2-63}$$

The quality factor of the varactor, i.e., loss in the varactor compared to its capacitance is given by

$$Q_v = \frac{1}{\omega_0 R_v C_v} \tag{2-64}$$

The ratio $P_s/P_v = R_sI_{res}^2/R_vI_{res}^2 = R_s/R_v$ due to the same current in the serial resonator. The tuning sensitivity with respects to the varactor capacitance is set by [32]

$$\frac{\partial f}{\partial C_v} = -\frac{f_0}{2C_v}\frac{P_v Q_v}{P_s Q_s} \tag{2-65}$$

which indicates that a wider tuning bandwidth for a given coupling P_s/P_v and f_0 is achieved with a lower varactor capacitance with a higher quality factor. The maximum tuning range is given when $P_v Q_v / P_s Q_s \to 1$, that is when $C_v/C_s \to 0$ for the varactor C_v in serial with the capacitance C_s of the resonator. The relative tuning sensitivity will also be maximized to

$$\frac{\partial f}{f_0} \Big/ \frac{\partial C_v}{C_v} = -\frac{1}{2} \tag{2-66}$$

Power handling in varactors

The Q-factor of the resonator is limiting the noise performance and tuning-range of the oscillator. Further, the voltage handling capability of the varactor itself is limiting a wideband tuning. The varactor is normally modeled as a voltage-controlled capacitor in serial with a loss resistance, and if V_R is representing the rms-voltage across the loss resistance in Figure 2-20, the dissipated power is expressed by

$$P_v = \frac{V_R^2}{R_v} \tag{2-67}$$

and the rms-voltage across the varactor capacitor, V_c, can be expressed as

$$V_C = Q_v V_R \tag{2-68}$$

The power dissipated in the varactor is equal to

$$P_v = \frac{V_C^2}{Q_v^2 R_v} \tag{2-69}$$

As the phase noise is minimized by maximizing $1/P_{res}Q_{L,res}^2$ in the resonator, the term V_C^2/R_v will be a figure-of-merit for a good varactor [23]. This term sets the maximum power handling of the varactor in the resonator. Equation (2-50) expresses the corresponding minimum achievable phase noise as

$$\mathcal{L}(f_m) = \frac{9FkTR_v}{16{V_C}^2}\left(\frac{f_0}{f_m}\right)^2 \tag{2-70}$$

In this case, the varactor contributes with all loss and power dissipation of the resonator, and the losses of other parts are neglected. The minimum phase noise given by (2-70) is valid for a reflection type oscillator. This level would be degraded twice for a feedback type oscillator (2-44). A feedback oscillator needs twice the dissipated power in the resonator to achieve the same performance as for a reflection oscillator.

Another effect to consider is that the voltage swing across the varactors increases with a stronger coupling to the resonator, besides for a higher Q-factor and increased input power level. The voltage swing can exceed the reverse-bias of the varactor in a case of junction capacitance based varactors. This effect starts to degrade the Q-factor in a large-signal condition at a rather low power level and must be considered [36]. Figure 2-21 (a) shows

the large-signal Q-factor degradation discussed in Paper [G], which demonstrates a varactor tuned cavity oscillator at 10 GHz. Figure 2-21 (b) shows the corresponding voltage swing across one single varactor in an anti-serial pair for different power P_{in} in the cavity. Bias level of -2 V is applied on the varactors. For higher power level and thus higher voltage swing, current leakage in the forward region will cause the Q-factor degradation. For low power, the voltage swing scales by $\propto Q\sqrt{P_{in}}$, until Q degrades at higher P_{in}.

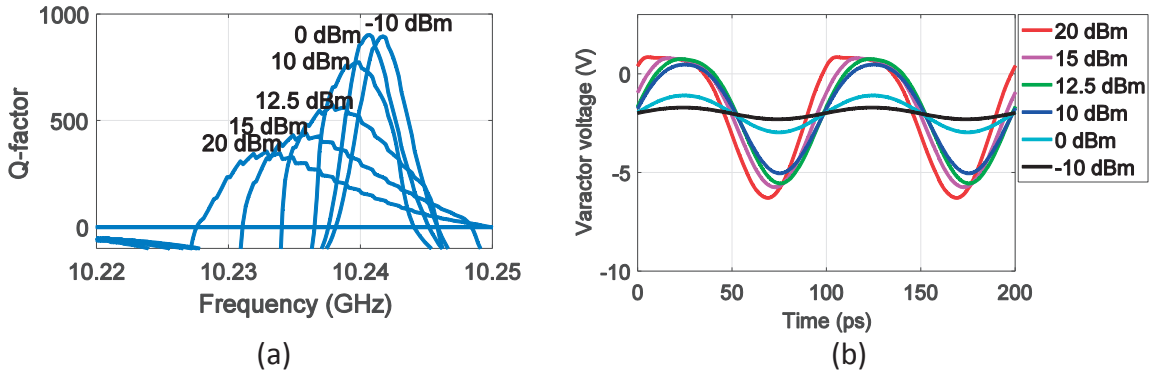

Figure 2-21. Simulated large-signal Q-factor degradation is shown. A shift in frequency due to self-bias of RF-power is noticeable. (a) Q-factor degradation for different input RF-power in the resonator. (b) Voltage across one single varactor in the anti-serial pair for different input RF-power.

As the power handling of the varactor can be a bottleneck for the phase noise of wideband varactors, it is beneficial to use two anti-serial varactors to divide the voltage swing. Another solution is to use weakly coupled varactors for a narrowband tuning. They can be used together with high power capable switches e.g. MEMS-switches for sub-band selection. This solution is proposed in Paper [A].

Generally, VCO tuning characteristics are nonlinear. The $C_v(V_v)$ characteristic is on the form

$$C_v(V_v) = \frac{C_{v0}}{\left(1 + \frac{V_v}{\varphi}\right)^{\gamma}} \tag{2-71}$$

where φ is the built-in potential, C_{v0} the capacitance at zero bias and γ is the varactor junction sensitivity. For abrupt varactors $\gamma = 0.5$, and for hyperabrupt varactors $1 \leq \gamma \leq 2$. As the $C_v(V_v)$ from (2-71) has a nonlinear behavior, normally two anti-serial varactors are used in designs to suppress harmonics from tuned capacitance [32]. Also, usage of hyperabrupt varactors will give a more linear frequency tuning, e.g., for $\gamma = 2$, a completely linear tuning will occur which is seen if using (2-71) in (2-58). This case is beneficial to suppress non-desired up-converted spuriouses.

2.6.2 MEMS based tuning

During the recent decades, extensive efforts have been invested in developing micro-machined structures, as RF-MEMS. They have become good candidates as tuning elements due to their high power capability and low loss [22]. However, drawbacks are their slow switching speed and that the moving mechanical structures can be influenced by vibrations. This causes inevitably electroacoustic coupling. Sensitivity for vibrations around 10-20 kHz is found in common MEMS with typical modal mass and spring constant for the moving structure [22], [46]. Rather high voltage is needed for MEMS types using

electrostatic actuation, around 10 V-30 V. This high voltage are also beneficial for the power capacity, due to the capable RF-swing before the switch will self-actuate. For a pull-in voltage of 1-30 V, the RF power required for self-actuation in a 50-ohm system corresponds to 0.02-18 W. Another application of low voltage MEMS-bridges are power-limiters, due to the protection capability and survival of high power.

The MEMS-switches can be categorized in several ways, regarding actuation mechanism, movement type, contact type, the circuit configuration and geometric type. Short descriptions of each category are discussed in following sections.

Common mechanisms to apply the force to the necessary movement of the membranes are listed below.

- **Electrostatic.** A bottom electrode beneath a membrane, which is connected to the RF-path, creates an attraction by an electrostatic force when a voltage is applied. The membrane bends to the other position, counterbalancing the spring force of the membrane. It reverts to its original position without the applied voltage. Figure 2-22 (a-c) show principal drawings.
- **Thermal.** A piece of material that changes shape with temperature causes the movement of the membrane.
- **Magnetostatic.** There are two different methods. A Lorentz force actuates patterned coils on the membrane by an externally applied magnetic field. The other method uses a ferromagnetic coating deposited on the membranes, which interacts with an externally applied magnetic field.
- **Piezoelectric.** A material that changes shape due to piezoelectric phenomenon causes the movement of the membrane.

The movement direction can be

- **Vertical**
- **Lateral**

The connection type in the RF-path can be

- **Metal-to-metal.** An ohmic connection is established between the membrane and the disrupted transmission line. The bottom electrode is still isolated. Figure 2-22 (a) shows a principal drawing.
- **Capacitive.** The distance between the gaps of the membranes and the disrupted transmission line is changed when the membrane is attracted to the other position. Figure 2-22 (b) shows a principal drawing.
- **Varactor.** The height of the membrane to the transmission line varies analogously by the voltage forming a controllable capacitance. Figure 2-22 (c) shows a principal drawing.

The membrane connecting to the RF-path can be

- **Series**, shown in Figure 2-22 (a).
- **Shunt**, e.g., connecting a grounded pad shown in Figure 2-22 (b).

The membrane topology can be

- **Cantilever type.** No residual stress remains within the membrane, as there is freedom for the tip to move which diminish static forces. The membrane is fastened only along one side shown in Figure 2-22 (a).
- **Fixed-fixed-beams.** The beams are fastened on two opposite sides and they will bend down in the middle in the presence of an actuation force shown in Figure 2-22 (b).
- **Circular diaphragms or membrane.** This is a production friendly shape.

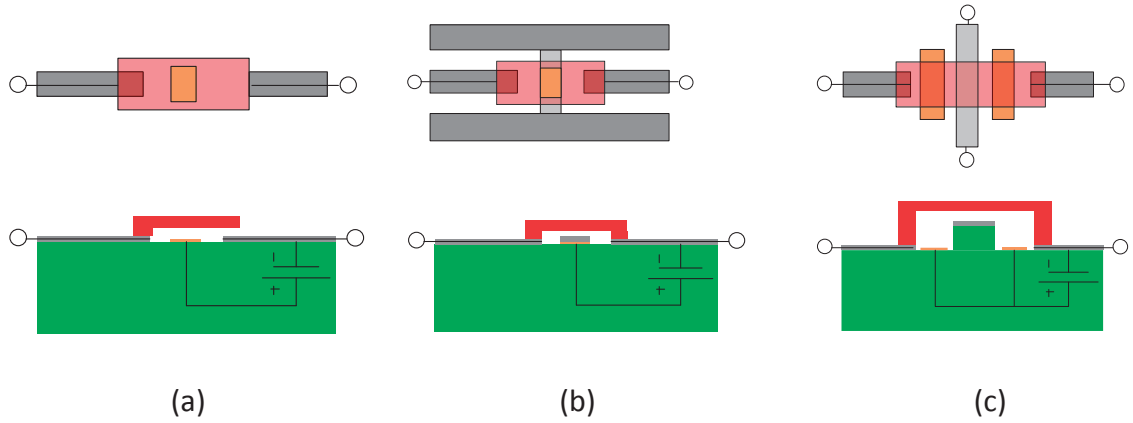

Figure 2-22 Typical MEMS-topologies, depicted with top view and crossection. (a) Ohmic cantilever. (b) Shunt capacitive. (c) Varactor with airgap separation to bottom electrode.

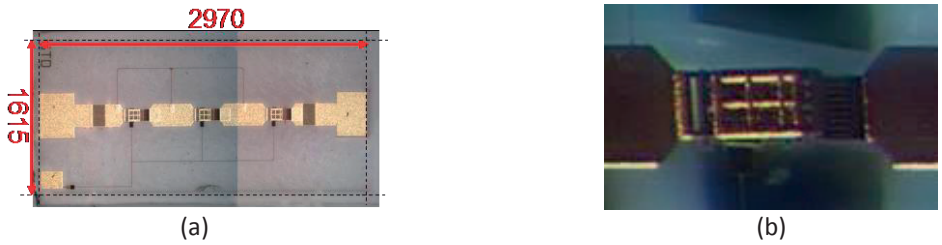

Figure 2-23 Cantilever MEMS from this study. (a) Chip photo. The chip size is 2970 x 1615 um and the MEMS contains three switch elements. (b) Chip photo. Cantilever in open position for one switch element.

Figure 2-23 (a-b) shows chip photo of the RF-MEMS-switches used in this study. They are designed by RF Microtech and fabricated at the FBK foundry.

RF-MEMSs have demonstrated good performance due to their high power handling and low loss. The power capacity is needed for a broad tuning range as the tuning elements need to be strongly coupled to the resonator. Further, a high power capacity in the resonator is needed for good phase noise performance. The low loss entails a high Q-factor, which

not will be suffered from large-signal degradation due to the high power capacity. However, the side-effects of electroacoustic vibration and some reliability issues are continuously improved.

2.7 Benchmarking oscillators

Benchmarking oscillators in literature are often a challenging task as several performance parameters are involved. These parameters can involve output power, power consumption, center frequency, offset frequency, tunability, etc. It is, therefore, a difficult task to define a single figure-of-merit for benchmark an oscillator. The figure could either, relate the performance to the physical boundaries set by the process technology as the Q-factor, and the device noise floor; or alternatively be dependent on some typical application.

According to Leeson's equation (2-29), the noise floor is measured relative the RF-power in the resonator, and therefore increasing the power is beneficial. The power can be increased by increasing the current density in the transistor, or by scaling the transistor size for the same current density. Drawbacks are that the close-in flicker noise, as well as shot noise for a bipolar device are increased with higher drain current, which will counterbalance the benefit of the increased signal power. The far out noise floor of HEMTs is improved at increased power.

2.7.1 Figures of merit

The power can be increased by combining several oscillators locked to the same reference. In general, the carrier power can be increased by N^2, if the output signals from N identical oscillators are added coherently in phase. Their noise power is added by the factor N, as the noise sources are uncorrelated. The noise to power ratio is improved by the factor N [25]. This is advantageous e.g., in MIMO systems using several oscillators [47].

The benefit of the increased output power compared to the noise floor implies that benchmarking oscillators might be measured with a DC-power normalized figure-of-merit. The figure-of-merit is further normalized with center frequency, and frequency offset for a fair comparison.

A commonly used key parameter for benchmarking is as previously suggested the power-normalized figure-of-merit, hereinafter referred to simply as *FOM*. DC-power normalized figures-of-merit must be handled with care. An example is that low power consuming oscillators can still reach high merit figures, although having low or moderate absolute phase noise performance. For a radio system, the absolute phase noise performance is the major important merit figure to increase the data capacity. However, if DC-power-normalized *FOM* is used together with the absolute phase noise performance to benchmark oscillators, it becomes a complementary measure of the power efficiency of the oscillator, and grades the design quality. The DC to RF-power is important to maximize, and the RF-power in the resonator is beneficial for the phase noise. The maximum *FOM* will be shown to be scaled by the unloaded Q-factor of the resonator and the noise floor within the $f_0/2Q$ bandwidth.

To benchmark the oscillator performance versus different technologies, *FOM*, is calculated under the assumption of no flicker noise. This figure was defined by Wagemans [48], and it was further refined in [49]. It is defined as

$$FOM = -\mathcal{L}_{\text{meas}}(f_m) + 20\log_{10}\left(\frac{f_0}{f_m}\right) - 10\log_{10}\left(\frac{P_{DC}}{1mW}\right) \tag{2-72}$$

where $\mathcal{L}_{\text{meas}}(f_m)$ is the measured phase noise at offset frequency f_m, f_0 is the oscillation frequency and P_{DC} (mW) the DC-power consumption.

In Leeson's equation, this is used as a base for scaling the effect of resonator power, and Q-factor, and to relate the figures to a physical noise floor. The fitting parameter, F_{eff}, can there be extracted from (2-52) as

$$F_{\text{eff}} = \mathcal{L}_{\text{meas}}(f_m) - 20\log_{10}\left(\frac{f_0}{f_m}\right) - 10\log_{10}\frac{27kT}{32} - 30 + 10\log_{10}\left(\frac{P_{DC}}{1mW}\right) + 20\log_{10}(Q_0) \tag{2-73}$$

F_{eff} can further be expressed with the definition of *FOM* in (2-72) as

$$F_{\text{eff}} = 174.6 + 20\log_{10}(Q_0) - FOM. \tag{2-74}$$

In case of no flicker noise and no RF-noise from the active device, and 100 % DC to RF conversion efficiency, meaning that F_{eff}=0 dB in (2-74), FOM_{max} is found to be linearly related to the unloaded Q-factor of the resonator. Normally $F_{\text{eff}} > 0$ dB, and *FOM* will be reduced. Obvious reasons for $F_{\text{eff}} > 0$ dB in (2-74) are the finite efficiency and the effect of non-ideal resonator coupling. If the effects of finite efficiency and non-ideal resonator coupling are considered, an operating noise figure can be defined by using the expression in (2-46) as

$$F_{op} = 173.9 + 10\log_{10}\frac{8\eta\beta}{(1+\beta)^3} + 20\log_{10}(Q_0) - FOM \tag{2-75}$$

It results that $F_{\text{op}} = F_{\text{eff}}$ in the ideal case $\eta = 100\%$ and ideal coupling $\beta = 1/2$.

The best performance that can be achieved at F_{eff}=0 dB in (2-73) for given process parameters, Q_0 and power capability, P_{DC} (mW) can be expressed as

$$\mathcal{L}_{min}(f_m) = -174.6 - 10\log_{10}(P_{DC}) - 20\log_{10}(Q_0) + 20\log_{10}\left(\frac{f_0}{f_m}\right) \tag{2-76}$$

This equation can be used to show trend lines for the phase noise performance in the used technology.

Table 2-2 presents process parameters as Q_0 and practical power capability. Calculated trend lines of the phase noise at 100 kHz for a 10 GHz oscillation frequency are shown. The power capability values are calculated from an averaged DC-consumption of the considered MMIC-designs among those from [50]-[65]. The reported results on DC-consumption in this calculation is used to take care of the practical issues for good bias

level. For example the choice of transistor size and bias condition to manage the needed cooling etc., influence on the typically used devices. Typical Q-factors for the respective process technology are found in textbooks as [51]. Phase noise trend lines and published results together with designs from this work are shown in Figure 2-24. The phase noise trend lines are based on calculations from (2-76). For mature processes like CMOS, the results are fairly well saturated at the phase noise trend line, but for GaN-HEMT there is still a significant discrepancy between reported values and the theoretical limit. Some oscillators designed in this work in hybrid technology, as for the cavity oscillators, are also included in Figure 2-24.

Table 2-2 Phase noise limit at 100 kHz offset from a 10 GHz oscillation frequency, calculated from process parameters for MMICs. The given bias levels are averaged values from the published oscillators, [50-65]

	GaN-HEMT,	InGaP-HBT	CMOS 90 nm	SiGe-HBT
V_c, / V_d (V)	30	5	1	3
I_c / I_d (mA)	120	90	9	25
Q_0	40	40	10	10
Phase noise@1 MHz (dBc/Hz), f_{center}=10 GHz	-142	-133	-104	-113

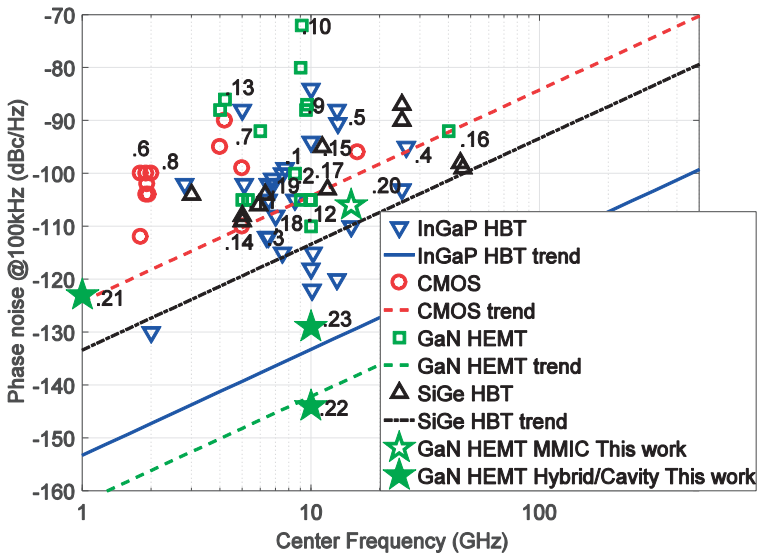

InGaP-HBT
1. [50]
2. [50]
3. [52]
4. [53]
5. [54]

CMOS
6. [55]
7. [56]
8. [57]

GaN-HEMT
9. [58]
10. [59]
11. [60]
12. [61]
13. [62]
20. Paper [E] (MMIC)
21. Paper [F] (Hybrid)
22. Paper [C] (Cavity)
23. Paper [A] (Cavity)

SiGe-HBT
14. [52]
15. [63]
16. [64]
17. [65]
18. [65]
19. [65]

Figure 2-24 Phase noise versus oscillation frequency for oscillators in different MMIC technologies, compared to GaN HEMT oscillators designed in this work. The trend lines are valid for typical MMIC technology parameters, presented in Table 2-2. Note that two oscillators designed in this work are designed in hybrid technology and consequently have significantly better Q-factor.

Table 2-3 shows a comparison to other state-of-art fixed frequency oscillators with high-Q-resonators in different technologies at X-band.

Table 2-3 State-of-the-art published High-Q oscillators for fixed frequency

Ref	$\mathcal{L}$(100 k) (dBc/Hz)	f_0 (GHz)	P_{dc} (mW)	FOM@ 100 kHz	Active device Technology	Resonator Technology
HMC-C200 8.0-8.3 GHz *(Hittite)*	-140	8.2	700(**)	209	N/A	DRO
[66], fig 9	-132(*)	9.2	N/A	N/A	GaAs pHEMT	Silver coated cavity
DRO-10.600-FR *(PSI)*	-137	10.2	N/A	N/A	N/A	DRO
[67]	-118	10.6	54(***)	201	GaN HEMT	DRO
[67]	-123	10.6	46(***)	207	GaAs pHEMT	DRO
[67]	-135	10.6	N/A	N/A	SiGe HBT	DRO
[68]	-149	7.61	400	221	GaAs InGaP HBT	DRO
[68]	-142	7.61	100	220	GaAs InGaP HBT	DRO
Paper [C]	-145	9.9	200	221	GaN HEMT	Aluminum cavity

(*)The plot in [66] is used to estimate the phase noise. (**) A buffer amplifier is included, but output power is comparable with other output power in this work. (***) calculated from power density and transistor size.

Figure of merit for tunable oscillators

The power-normalized figure of merit, *FOM*, is physical in the sense of the phase noise scaling with DC-power consumption, loaded Q-factor, oscillation- and offset frequency. A figure-of-merit value also including the tunability is more difficult to define. A definition, commonly used by MMIC designers, is to normalize to 10 % tuning, which is considered to be a typical tuning range for MMIC VCOs [69],

$$FOM_T = -\mathcal{L}_{meas}(f_m) + 20\log_{10}\left(\frac{f_0}{f_m}\right) - 10\log_{10}\left(\frac{P_{DC}}{1mW}\right) + 20\log_{10}(TR/10) \quad (2\text{-}77)$$

or expressed as

$$FOM_T = FOM + 20\log_{10}(TR/10) \quad (2\text{-}78)$$

where the factor TR is the percentage relative tuning ratio. From (2-78) it is clear that the FOM_T will be degraded from the FOM-value if tuning range lower than 10 % is achieved.

Another figure-of-merit is using the absolute tuning bandwidth without the DC-power consumption as [44]

$$FOM'_T = -\mathcal{L}_{meas}(f_m) + 20\log_{10}\left(\frac{BW}{f_m}\right) \quad (2\text{-}79)$$

A benefit of this definition is that normalizing to the center frequency is not needed explicitly, as it is already considered when the absolute tuning frequency $BW = TR \cdot f_0/100$ is used, instead of relative tuning as in (2-77).

However, a complication of the figure-of-merit in (2-77) and (2-79) is that they do not asymptotic converge to the figure-of-merit of a fixed frequency oscillator as in (2-72) when the tuning bandwidth decreases to zero.

Table 2-4 presents a comparison between tunable oscillators technologies.

Table 2-4 State-of-the-art published high-Q tunable oscillators

Ref	Phase noise @ 10 kHz (dBc/Hz)	Phase noise @ 100 kHz (dBc/Hz)	Phase noise @ 1MHz (dBc/Hz)	fc (GHz)	Tuning-ratio (TR) (%)	Q_0	FOM	FOM_T (*)	Tech-nology
[70]	-135			9.84665-9.8472	0.0056	10k-22k	-	-	DRO,SiGe
[71]	-100	-129	-149.5	8.2	1.28	510 load	211.7	194	micro-strip,SiGe
[72]	-121.7	-133@ 50k		13.3	0.165 mechanic	13k	-	-	DRO,GaAs pHEMT
[73]	-78	<-100	-123	11.4033-11.5565	1.34	-	-	-	SIW,SiGe
[74]			-134.5 (at 500k)	3.475	6		167.1	162.7	MEMS-varactor, microstrip, SiGe
[75]		-95.6	-125.1	11.16	4.1	300	193	185	SIW, GaAs HEMT
[76]			-122	12.2	2.5 mechanic		189.1	177	SIW, HJ-FET
[43]	-100	-130		2-4	67				YIG
[77]		-132.7		5.3	0.094				Vt-DRO,
[78]	-108.4	-129.4	-152.4	23.12	3.8		214.5	206	Möbius strip SiGe HBT
[79]			-109	22.1	20.6		181	187	SiGe Integrated
[80]			-117	9.5	4.8		180.9	174.5	SIW, pHEMT
Paper [A]		<-129	<-158	10	5	500	202	196	MEMS (@1mm)
Paper [A]		<-123	<153	10	12.3	500	196	198	MEMS (@2.5 mm)
Paper [C]		-144	<-165	9.9	-	3800	227	-	Cavity fixed freq
Paper [E]		-106	<-132	15	-	40	191	-	MMIC
Paper [G]		-118	-146	10	1.6	400	201	185	Cavity with diode varactors

(*) $FOM_T = -\mathcal{L}(\Delta f) + 20\log(f_0/\Delta f) - 10\log(P_{DC}/1mW) + 20\log(TR/10)$ or $FOM_T = FOM + 20\log(TR/10)$

Chapter 3.

Component characterization

This chapter discusses component and device characterization of sub-blocks used throughout in the oscillator study.

It initially starts to describe the used active device regarding DC-characteristic for a bare die and DC and gain behavior for the same device integrated in a MMIC-amplifier. It further presents a developed low-frequency noise measurement setup for high bias condition suitable for GaN-HEMTs. The measured characteristics adapt the simulation models for the oscillator for more accurate noise prediction. Further, the chapter describes a high-Q resonator of an aluminum cavity with flexibility to adjust the coupling to an excitation microstrip line. The chapter discusses the cavity modes in detail, and finally, it reports the characterization of used tuning elements of MEMS and varactors and discusses a proposal of how to efficiently integrate them in the cavity to enhance tunability.

3.1 Active device characterization

The used reflection amplifier is based on a GaN-HEMT, 8x50 um gate periphery and 0.25 um gate length processed in TriQuint's 3MI-process. DC-characteristics versus model for a bare die are shown in Figure 3-1 (a-b).

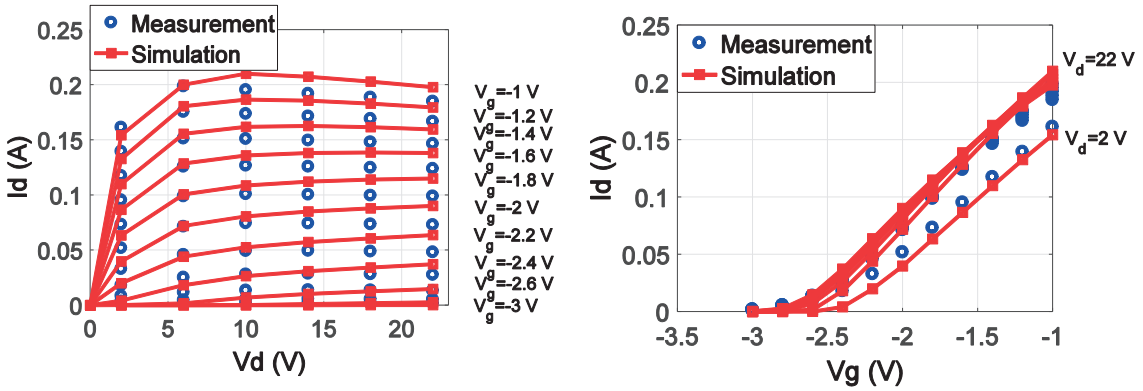

Figure 3-1 IV-plots simulated (red square) and measured (blue circle) for the 8x50 um HEMT used in the design (a) I_d versus V_d, (b) I_d versus V_g.

Figure 3-2 (a-c) show bias characteristics I_d versus V_d, I_d versus V_g and reflection gain, respectively, for the MMIC reflection amplifier based on the 8x50 um HEMT.

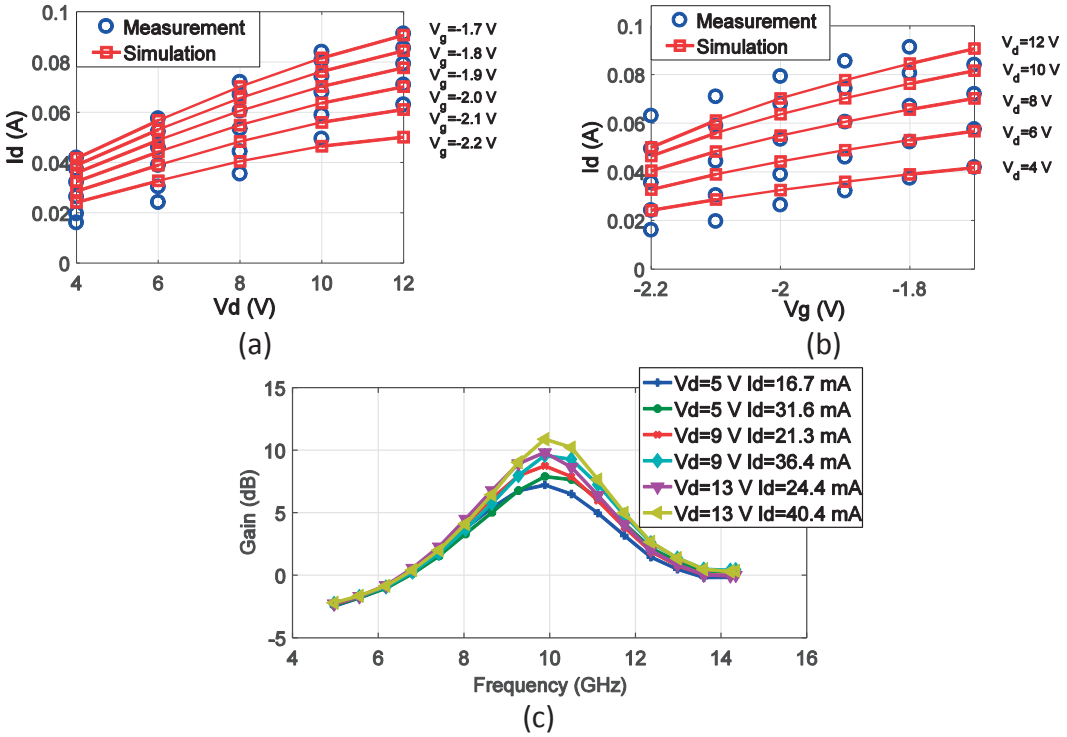

Figure 3-2 MMIC reflection amplifier with HEMT-device 8x50 um. (a) Measured I_d versus V_d compared to simulations. V_g swept from -2.2 V to -1.7 V. (b) Measured I_d versus V_g compared to simulations. V_d is swept from 4 V to 12 V(c) Measured reflection gain for different bias.

The different IV-characteristic for the complete MMIC compared to the bare die depends on a source resistance added in the MMIC for bias regulation and for increasing the gain, as is described in Paper [C].

3.2 Flicker noise characterization

Verification of the low-frequency noise (LFN) spectra will put some specific demands on the instrumentation setup. The bias tee must have a low cutoff frequency, and it is necessary to consider the input impedance of the low noise amplifiers not to affect the DUT, etc. Two measurement methods are analyzed in the study, and they are discussed in the following sections.

Current-noise amplification

The first method is using a transimpedance preamplifier system, based on a commercial amplifier (SR570) [81]. For low bias level, <5 mA, the internal bias supply in SR570 has a satisfying noise performance. A higher bias level will require an external bias-tee. That may limit the lowest cutoff frequency, because of the practical size of the inductors and capacitors used for the filtering. Also, large capacitors are often of the electrolyte type, which themselves contribute to flicker noise, and therefore the system noise level must be investigated carefully in the setup for clarifying its limitations. Figure 3-3 illustrates the setup, which is described in detail in [82].

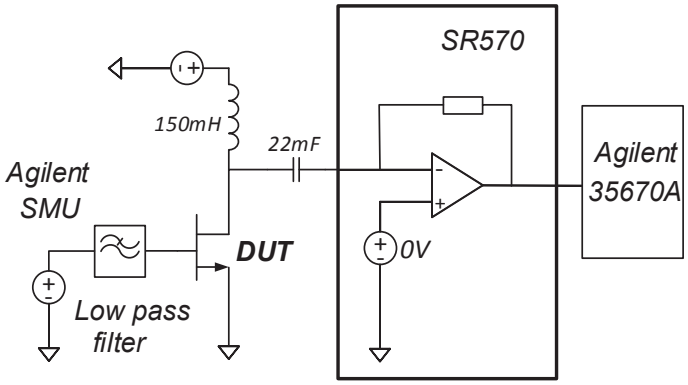

Figure 3-3. LF-noise setup with current-noise amplification and external bias.

The transimpedance amplifier has low input impedance, around 1 Ω. The bias-tee components, 150 mH, and 22 mF are chosen to be parallel resonant at 3 Hz according to (3-1) for not short-circuiting the LF-noise from the DUT. On the other hand, they must make a good conduction for the current noise to the low impedance current amplifier.

$$f_{res} = \frac{1}{2\pi\sqrt{0.15 \cdot 0.022}} = 3 \text{ Hz} \tag{3-1}$$

The output of the amplifier is connected to a dynamic signal analyzer, Agilent 35670A, which measures the voltage of the signal in time domain and calculates the FFT for frequencies up to 100 kHz.

One disadvantage of the current amplifier method is the settling time to charge the large capacitor in the DC-block when changing bias which makes these measurements for different bias very time-consuming.

Voltage-noise amplification

The other method is based on a high-impedance voltage amplifier, SR560 [83]. The bias to the device is connected through a load resistor, which in the setup is chosen to 100 Ω. This value is suitable for the studied sizes of devices. As there is a lower cutoff-frequency for the bias components in the signal path for this setup, it can measure noise almost down to DC. That makes the method very attractive. However, the load resistor must be chosen carefully, preferably less than the transistor channel resistance, R_{ds}, to ensure that the external load dominates for the total resistance and that it is low enough with an acceptable low thermal noise contribution. The current noise is calculated by considering the channel resistance R_{ds} in parallel with the external load resistor which is seen in Figure 3-4.

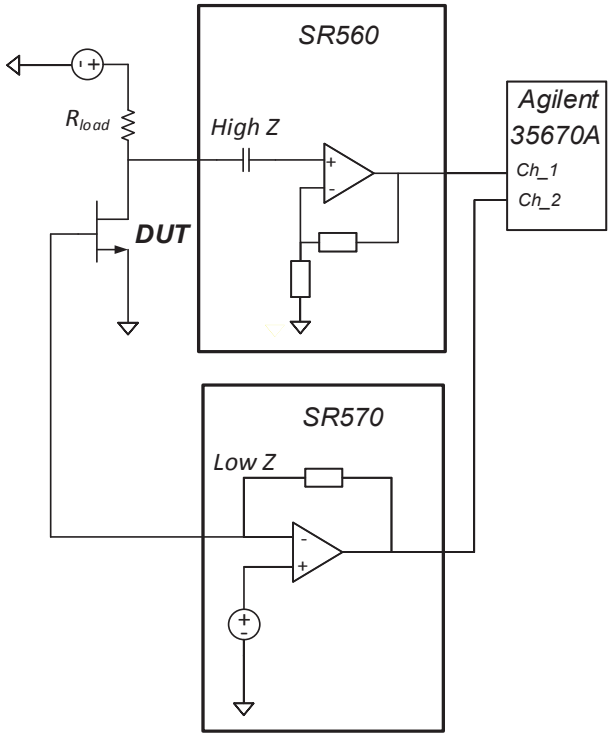

Figure 3-4. LFN setup with a voltage amplification with SR560 on the drain and with SR570 on the gate, essentially for biasing purpose.

The SR560 measures the voltage noise terminated by the load resistance, which is the load resistor, R_{load}, in parallel with R_{ds}. The current noise is calculated by normalizing the voltage noise with the total load impedance. The used voltage gain of the SR560 is about 40 dB (100 V/V), and its noise floor at the input is about 4 n$V/\sqrt{\text{Hz}}$. The transimpedance amplifier SR570 measures the gate noise simultaneously, but main reason in this measurement is to use its internal supply to bias the gate.

$$< I_{drain\ noise} >= \frac{< V_{meas\ \ noise\ 35670} >}{(R_{ds}//R_{load}) \cdot G_{voltage\ gain\ SR560}} \tag{3-2}$$

The same dynamic signal analyzer, Agilent 35670A, samples the output signal from the low noise amplifiers. A description of a similar setup is found in [84].

Test bed verification

The system noise level for the different setups is investigated by measuring a BJT transistor, 2N2222, because it has a relatively low LFN. Low bias (<8 mA, 3 V) makes it convenient to compare the different setups without introducing too much LFN from the setup itself. Different bias supplies have been used to control their noise impact in the voltage-noise measurement setup; a battery and a parameter analyzer, Agilent 4156. In the current-noise measurement setup, the internal supply in SR570 is used. Figure 3-5 (a) shows the results of this investigation. Figure 3-5 (b) shows the result of a GaN-HEMT device measured with the two different methods.

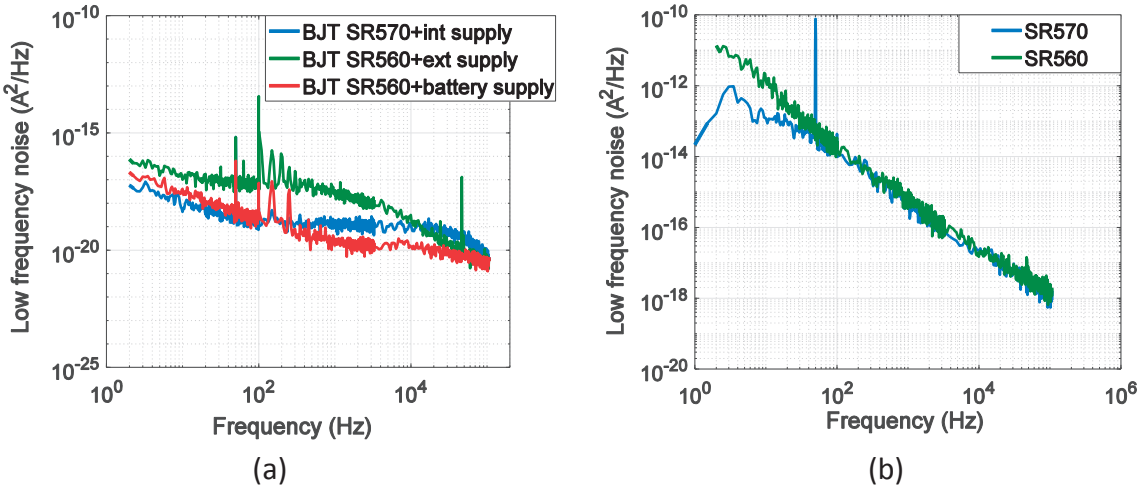

Figure 3-5 (a). Noise floor characterization by measuring a BJT 2N2222 in the testbed. (b) Comparison between the setups of the current-method (SR570) and the voltage-method (SR560) measuring a GaN-HEMT, 4x75 inhouse from the CTH-process, biased at V_g/V_d=-2 V/11 V.

The thermal noise floor of the load resistor (100 Ω) used in the SR560-setup is calculated as

$$< i_{n,100}^2 >= \frac{4kT}{R} = 1.6 \cdot 10^{-22}\ (\mathrm{A^2/Hz}) \tag{3-3}$$

This is about 10 dB lower than the lowest device noise floor measured in Figure 3-5, and therefore it is considered to have a negligible effect on the system noise floor in the studied frequency range.

The study concludes that the noise from the power supply affects more than the measurement method itself, and therefore, the voltage-noise amplification method is used for further LFN measurements. Besides, the voltage-noise method provides LFN measurement almost down to DC, which is shown in Figure 3-5 (b). Paper [H] presents a detailed comparison between different devices in GaN measured by this setup. Later, a compliance verification with a commercial system, E4727A, from Keysight Technologies, was performed, which showed similar results.

LFN at 1 kHz, 10 kHz and 100 kHz normalized to DC power is a relevant benchmark parameter for oscillator applications. Table 3-1 present measured LFN for GaN-HEMTs compared to other III-V material (InGaP HBT and GaAs pHEMT).

Table 3-1 Measured devices with voltage amplification method reported in Paper [H]

Device	Size (µm)	L_g/W_b (nm)	F_{fe}	Id (mA)	Vd(V)	LFN@1kHz (A^2/Hz)· 10^{-15}	$\frac{LFN@1kHz}{V_c \cdot I_c}$ (A/Hz•V) · 10^{-15}	LFN@10kHz (A^2/Hz) · 10^{-18}	$\frac{LFN@10kHz}{V_c \cdot I_c}$ (A/Hz•V) · 10^{-18}	LFN@ 100kHz (A^2/Hz) · 10^{-18}	$\frac{LFN@100kHz}{V_c \cdot I_c}$ (A/Hz•V) · 10^{-18}
GaN HEMT 1	2x75	250	1.5	19.3	10	0.426	2.21	24.1	125	1.76	9.13
GaN HEMT 2	4x75	250	1.3	27.4	10	0.227	0.831	32.6	119	2.67	9.76
GaN HEMT 3	2x50	250	1.3	20.0	10	0.675	3.37	25.6	128	0.863	4.31
GaN HEMT 4	4x50	250	1.3	38.9	10	1.53	3.92	66.6	171	1.75	4.50
GaN HEMT 5	8x50	250	1.3	81.0	10	3.10	3.83	145	178	3.48	4.30
GaN HEMT 6	4x50 (G2)	250	1.5	4.73	10	0.450	9.51	17.1	361.8	0.143	3.03
GaN HEMT 7	8x50 (G3)	250	1.5	52.6	10	2.79	5.31	66.6	127	0.655	1.24
InGaP HBT 1	4x20	1000	1.2	9	3	0.007	0.389	0.530	19.6	0.110	4.07
InGaP HBT 2	2x20	1000	1.2	9	3	0.004095	0.152	0.454	16.8	0.132	4.90
GaAs pHEMT 1	2x20	150	1	12.6	3	0.142	3.75	30.0	792	2.59	68.5
GaAs pHEMT 2	4x20	150	1	24.8	3	0.187	2.51	44.0	591	4.98	66.82
GaAs pHEMT 3	2x20	100	1	5.55	3	0.143	8.61	20.0	1200	2.64	159
GaAs pHEMT 4	4x20	100	1	11.2	3	0.181	5.35	33.5	992	3.85	114
GaAs pHEMT 5	2x40	100	1	11.5	3	0.183	5.32	27.6	801.5	4.06	118
GaAs pHEMT 6	4x40	100	1	24.9	3	0.265	3.55	38.8	519	4.71	63.1

The parameters in Table 3-1 are denoted by L_g for the gate length, W_b base width, F_{fe} for the frequency slope ($1/f^{Ffe}$), and *LFN* (A^2/Hz)@ 1 kHz, @10 kHz, and @100 kHz for the measured LFN at the respective offset frequencies. It is obvious that the flicker noise at <100 kHz is higher for GaN-HEMTs than for InGaP HBTs. GaN-HEMTs are however better if the power-normalized noise is considered. The active devices for almost all designed oscillators in this study are based on the GaN-HEMT 8x50 (G3), which is shaded in Table 3-1. Figure 3-6 (a) shows the measured LFN for this used device versus frequency compared to simulation model, and Figure 3-6 (b) shows the measured LFN at 100 kHz versus bias.

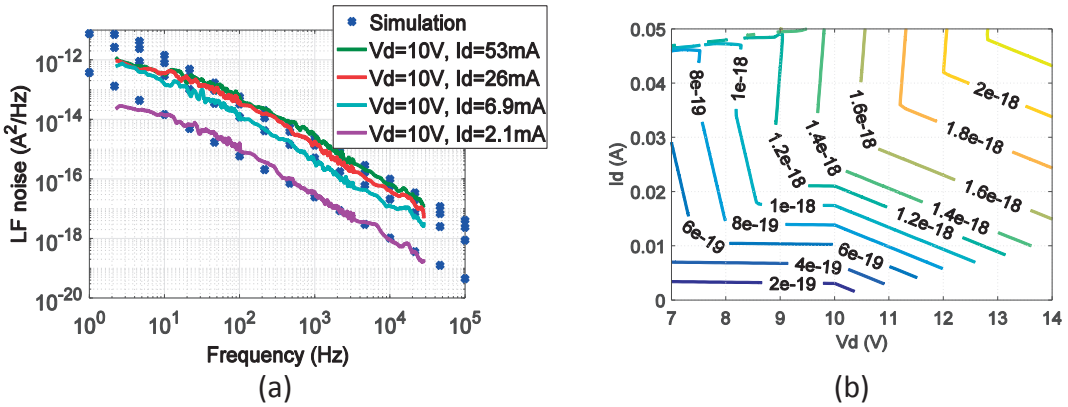

Figure 3-6 Measured low-frequency noise of (a) measured LFN (A^2/Hz) versus frequency. Fixed V_d=10 V for different current compared to simulation. (b) Measured LFN (A^2/Hz) at 100 kHz versus bias.

3.3 Cavity resonators and modes

The resonator is as previously mentioned a critical component for the oscillator phase noise performance close to the carrier. Some oscillators designed in this study are based on external high-Q resonators implemented as aluminum cavities. The following chapters discuss the theory and the characterizing of the used cavity resonators.

3.3.1 General theory of rectangular waveguide resonators

The propagation property of a waveguide depends on its dimensions. The phase propagation constant of a rectangular metal waveguide can be expressed

$$\beta = \sqrt{k^2 - k_c^2} \tag{3-4}$$

where

$$k = \omega\sqrt{\mu\varepsilon} \tag{3-5}$$

and

$$k_c = \sqrt{\left(\frac{m\pi}{a}\right)^2 + \left(\frac{n\pi}{b}\right)^2} \tag{3-6}$$

In (3-6) a and b are the side lengths of the rectangular cross section. The permittivity ε and the permeability μ define the medium properties, ω the used angular frequency, and m and n define the mode number. The waveguide wavelength along z-axis can be written as

$$\lambda_g = \frac{2\pi}{\beta} = \frac{2\pi}{\sqrt{\omega^2\mu\varepsilon - \left(\frac{m\pi}{a}\right)^2 - \left(\frac{n\pi}{b}\right)^2}} \tag{3-7}$$

A cavity resonator can be realized by short-circuiting the waveguide along the z-axis, at $z = 0$ and at $z = d$, respectively. The resonances will occur during the following condition,

$$l\frac{\lambda_g}{2} = d, \qquad l = 1,2,3,\ldots \tag{3-8}$$

Figure 3-7 depicts the E-field for mode l=1, and 2, and m=1.

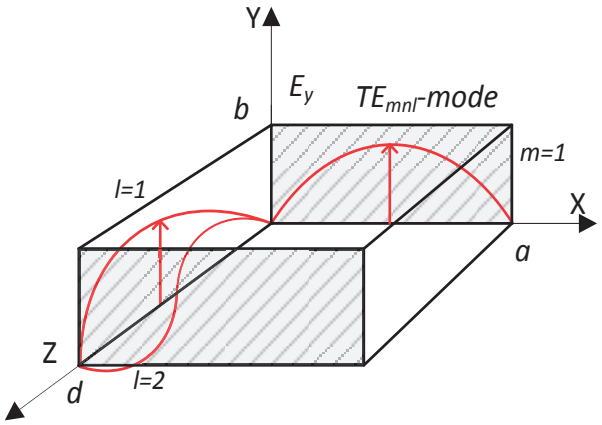

Figure 3-7 TE_{mnl}-mode shown in a resonator for l=1 and 2, and m=1

By inserting (3-7) in (3-8), the resonance frequencies can be written as [85]

$$f_{mnl} = \frac{c_0}{2\pi\sqrt{\mu_r\epsilon_r}}\sqrt{\left(\frac{m\pi}{a}\right)^2 + \left(\frac{n\pi}{b}\right)^2 + \left(\frac{l\pi}{d}\right)^2} \tag{3-9}$$

The dominant mode at the lowest frequency will be the TE_{101}-mode ($m = 1, l = 1$), which evaluates to a=d=$\lambda_g/2$. It is common to set b=$\lambda_g/4$ to assure maximum margin to other resonant modes.

The E-field in y-direction for this mode, $E_y(x,z)$, is creating a standing wave inside the cavity, which can be expressed as [85]

$$E_y = E_0 \sin\frac{\pi x}{a}\sin\frac{\pi z}{d} \tag{3-10}$$

Figure 3-8 illustrates the E_y-field-distribution for the TE_{101}-mode.

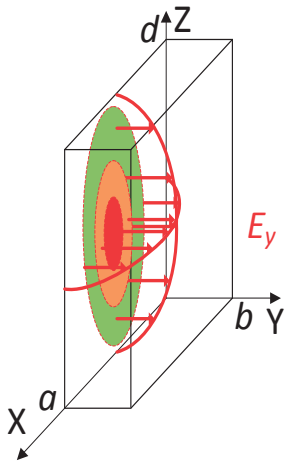

Figure 3-8 E_y-field distribution for the TE_{101}-mode

The stored electric energy at resonance is calculated by

$$W_e = \frac{\varepsilon}{4}\int_V E_y E_y^* dV = \frac{\varepsilon abd}{16}E_0^2 \tag{3-11}$$

which at resonance is the same as the stored magnetic energy, $W_m = W_e$.

The contribution of losses in the cavity is power dissipation in the cavity wall, dielectric loss in the substrate and radiated power. The power loss due to finite conductivity in the wall is expressed by [85],

$$P_c = \frac{R_s}{2}\int_{walls} |H_t|^2 dS = \frac{R_s E_0^2 \lambda^2}{8\eta^2}\left(\frac{ab}{d^2} + \frac{bd}{a^2} + \frac{a}{2d} + \frac{d}{2a}\right) \tag{3-12}$$

where the surface resistivity $R_s = \sqrt{\omega\mu_0/2\sigma}$, and $\eta^2 = \mu/\varepsilon$, and H_t is the tangential magnetic field at the wall's surface.

Q-factor due to the conductive loss is calculated by

$$Q_c = \frac{2\omega_0 W_e}{P_c} \tag{3-13}$$

The dielectric loss is expressed by

$$P_d = \frac{1}{2}\int_V \bar{J}\cdot\bar{E}^* dV = \frac{\omega\varepsilon''}{2}\int_V |\bar{E}|^2 dV = \frac{abd\omega\varepsilon''|E_0|^2}{8} \tag{3-14}$$

where $\varepsilon = \varepsilon' - j\varepsilon''$, for the effective dielectric constant including substrate loss.
The Q-factor due to substrate loss is estimated for $\varepsilon'' \ll \varepsilon'$ to

$$Q_d = \frac{2\omega W_e}{P_d} = \frac{\varepsilon'}{\varepsilon''} = \frac{1}{tan\delta} \tag{3-15}$$

The total unloaded Q-factor for the cavity can be calculated to

$$Q_0 = \left(\frac{1}{Q_c} + \frac{1}{Q_d}\right)^{-1} \tag{3-16}$$

In this study, the lowest resonant mode, TE_{101}-mode, for a rectangular metal cavity is considered for simplicity. That also makes a large frequency separation to other undesired modes.

The dielectric loss and the conductive loss in the cavity walls limit the Q-factor of the resonator. Therefore, this study uses an air-filled cavity in aluminum with Q_0 measured to 3800 which is further reported in Paper [C].

Similar calculations appear for dielectric resonators, which might support other more peculiar modes with several tens of thousands in Q-factor. The Whispery-Gallery mode is an example of an azimuthal propagation of the wave around the resonator [86], [87], etc.

Other popular modes for dielectric resonators are the evanescent modes where the field will cut off at the boundary of the high permittivity of a dielectric to the surrounded low dielectric air. This mode has a decreased height of the resonator, L, and appears lower than $2L/\lambda_g < 1$, which means that the resonator is reactively terminated at the ends. That mode is beneficial for having more dense volume, larger spurious-free region, and for being easier coupled with improved feasibility for monolithic integration.

The frequency tuning of high-Q resonators as metal cavities or ceramic resonators is non-trivial. A consequence of their high Q-factor is that they will have very limited coupling possibilities of tuning elements and accessibility to the resonator structure. In particular, if external loading or phase shifting techniques are used outside the resonator, these will have limited effect on the frequency tuning. A more efficient method is to directly disturb the EM-field inside the cavity as proposals presented with tunable ground plane using RF-MEMS switches as in Paper [A] and Paper [B], or by using GaAs-varactors connected to field probes inside the cavity as demonstrated in Paper [G].

Furthermore, the tuning elements require very high Q-factors to have minor degradation of the total Q-factor of the resonator. Also, the power (or voltage) capability can be a severe problem due to high voltage and current swing in high-Q resonators across the terminals of the tuning elements. The conversion of modulation noise must be considered, or in the case of electromechanical tuning as for MEMS-technology, the vibration sensitivity should be handled with care.

3.3.2 Tuning with an electronically controlled wall

In principle, the resonance frequency can be tuned by changing the distance between the short-circuiting planes in the z-direction of the cavity resonator. Paper [A] analyzes a method to do that by using RF-MEMS-switches on a PCB intruded in the cavity close to the wall as is illustrated in Figure 3-9. This method aims to digitally tune the frequency to

specific sub-bands, and the analog fine-tuning within the sub-band can be achieved by weakly coupled varactors.

Figure 3-9. E-field contribution with an electrically tunable wall inside the cavity. (a) RF-MEMSs in open state. (b) RF-MEMSs in a closed state.

Two effects mainly contribute to the frequency change. The electrical volume is contracted when the switches are in a closed state, due to the short-circuiting by the switched ground plane. The change in volume $-\Delta V_b$, that is obscured by the switches, creates the frequency change as [85],

$$\frac{\omega - \omega_0}{\omega_0} = -\frac{2\Delta V_b}{V_0} \tag{3-17}$$

The other effect is when switches are in open state, and they, besides, forming the original volume V_0 also add part of an increased volume ΔV_s beneath the switch elements with other medium with dielectric constant ε_r as [85]

$$\frac{\omega - \omega_0}{\omega_0} = -\frac{(\varepsilon_r - 1)\Delta V_s}{2V_0} \tag{3-18}$$

The new oscillation frequency is denoted ω, and the original resonance frequency is denoted ω_0 corresponding to the volume V_0. Figure 3-10 (a) and (b), respectively, show HFSS-simulations with RF-MEMS switches in open state and closed state for a three-row configuration of RF-MEMS in parallel. The RF-field penetrates through the RF-MEMS switches in the open state, but will be shielded by the switches in the closed state.

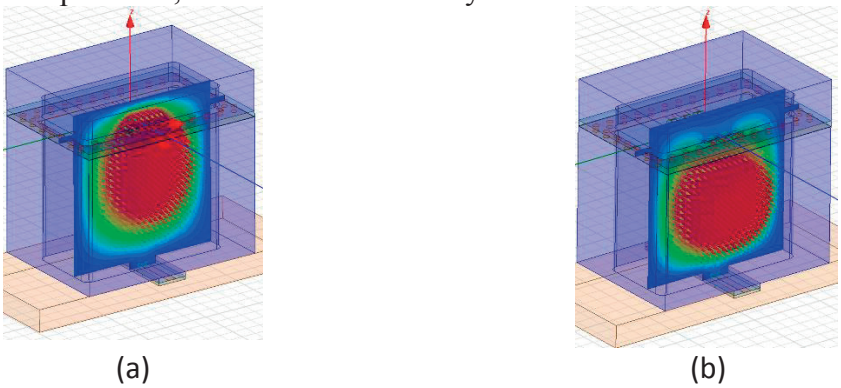

Figure 3-10 HFSS-simulations of the E-field. (a) MEMSs are in open state. (b) MEMSs are in closed state.

3.3.3 Analog cavity tuning with varactors

Tuning technologies performed with varactors integrated on chip-resonator circuitry for example in MMIC-solutions as Colpitts oscillators are successful for a large tuning-range [69], but the processes have often poor Q-factors for the resonators. External high-Q resonators, example DROs, make the varactor coupling difficult to achieve for a broad tuning range, consequently due to their high Q-factors as previously mentioned. The discussed method to change a load capacitance outside the resonator is demonstrated in [72], [88], [71], or to change the phase condition with a drawback to not utilize the optimum Q-factor of the resonator is showed in [70] and [89]. These techniques provide a tuning range of only a few tenths of a percent. More attractive is to embed the varactors inside the resonators, as solid-state varactors integrated with SIW-resonators demonstrated in [90], or by using high-Q-MEMS varactors in SIW as in [91] and [92], or for lumped LC-resonators [74].

Paper [G] demonstrates an aluminum cavity with embedded bare die GaAs varactor diodes inside a cavity. They are exposed directly of the RF-field for most efficient coupling. The varactors align with the E-field in the waveguide. Their capacitance C_{var} increases the electrical length of the waveguide, which is short-circuited at the end by a lid, and the resonance frequency will decrease. This is illustrated in Figure 3-11, and despite the model is developed for a two-conductor TEM-transmission line, it can principally model the behavior at resonance for a waveguide, in particular for the TE_{101} mode with short-circuited condition for a $\lambda_g/2$-resonance. The C_{var} is aligned with the E-field, transversally to the propagation direction.

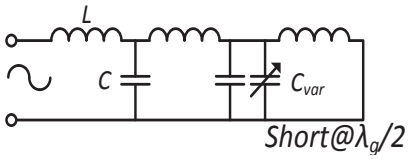

Figure 3-11 An equivalent circuit of the terminated waveguide with an included varactor.

Two-port S-parameter measurements of the designed cavity have been performed for different setups. Figure 3-12 (a) and (b) show the reflection coefficient and unloaded Q-factor, respectively, for intrusion depth of the assembled position of the varactors of 1 mm. Figure 3-13 (a) and (b) show the reflection coefficient and unloaded Q-factor, respectively, for an intrusion depth of 2.5 mm. The larger intrusion depth gives a stronger coupling of the varactor, which increases the tuning range from 1.6 % to 2.0 %. The deviation to the compared HFSS-simulation depends on parasitic and tolerances for the different assembly alternatives. The total lower Q-factor of the cavity at higher frequencies, despite the better Q-factor internally for the varactor at more reversed bias, is explained by the cavity itself degrades the Q at a larger disturbance from its natural resonance frequency.

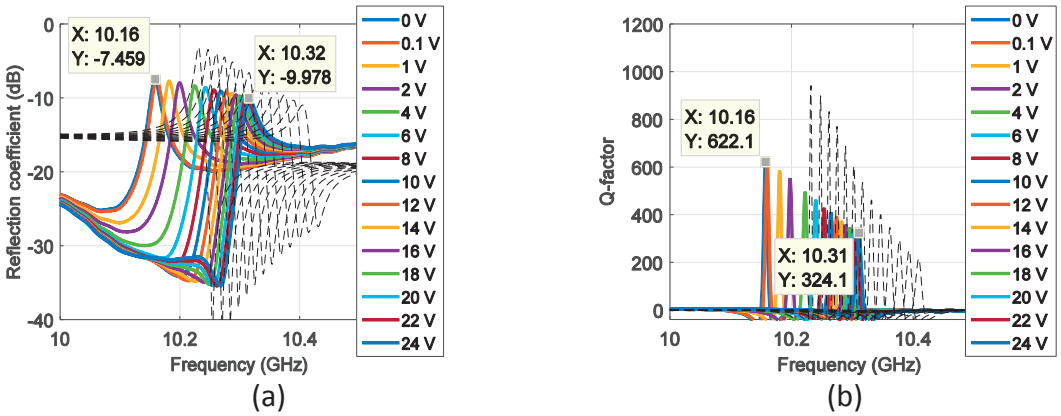

Figure 3-12. Varactors assembled at 1 mm depth in the cavity at different reversed voltages. (a) Measured reflection coefficient compared to HFSS-simulation in dotted black trace. (b) Measured Q-factor compared to HFSS-simulation in dotted black traces.

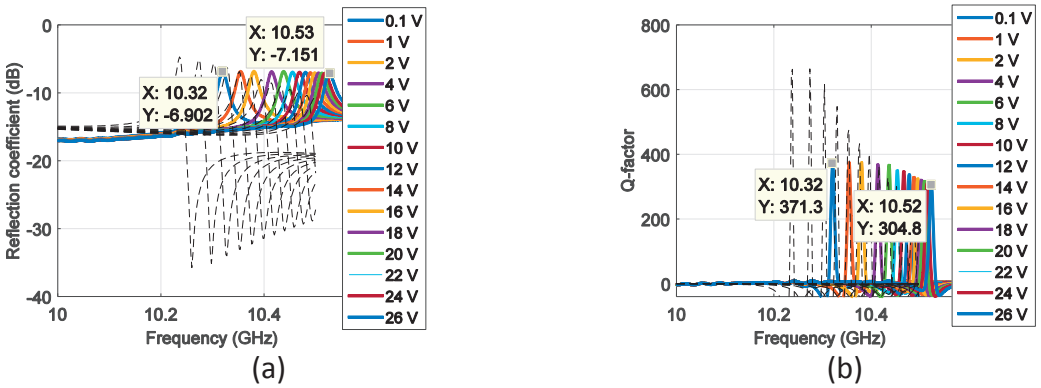

Figure 3-13. Varactors assembled at 2.5 mm depth in the cavity at different reversed voltages. (a) Measured reflection coefficient compared to simulation in dotted black trace. (b) Measured Q-factor compared to simulation in dotted black traces.

3.3.4 Varactor device characterization

The used varactors are manufactured by MA/Com of type MA46H146 bare-die and flip-chip mounted in GaAs-technology with abrupt γ=0.5 doping profile. They are characterized by a resonant Deloach-structure [93], shown in Figure 3-14 (a) and (b), and the measured transmission is shown in Figure 3-14 (c). Measurement extracts R_s and C_j to 2 ohm and 40 fF, respectively, for a reversed varactor voltage of -24 V. The unloaded Q_0 for the varactor, defined as $Q_0 = \text{imag}(Z_{var})/\text{real}(Z_{var}) = 1/\omega C_j R_s = 200$ at 10 GHz.

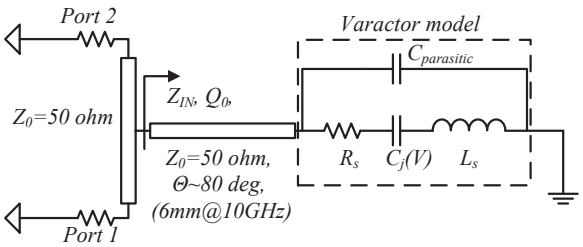

(a)

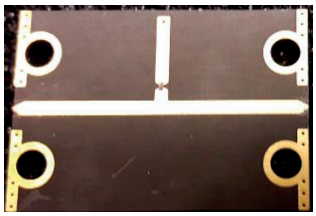

(b)

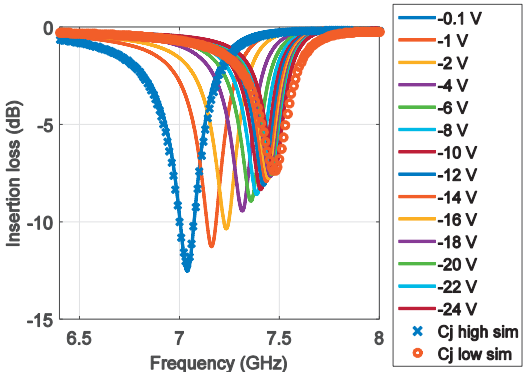

(c)

Figure 3-14 (a) Schematic of the test-structure. (b) Photo of the PCB test-circuit. (c) Measured transmission compared to simulation on the test-structure for different varactor voltages.

3.4 MEMS device properties

The used RF-MEMSs in this study are aimed for a digital sub-band selection for multichannel oscillators with moderate requirements on switching speed. The switches are characterized during electrostatic conditions by S-parameters to define a small-signal model.

However, in the application of the oscillator, the electroacoustic phenomena due to the electrodynamic behavior affect the phase noise. Particularly sensitiveness is at offset frequencies corresponding to the mechanical resonances.

3.4.1 Measured electrostatic behavior

The RF-MEMS is a mechanical system where an electrostatic force pulls down a membrane described as [22], [46], [94],

$$F_e = -\frac{1}{2}\frac{\varepsilon_0 A}{d^2}{V_{act}}^2 \tag{3-19}$$

where A is the membrane area, d the distance between the membrane and the actuator, ε_0 the dielectric constant and V_{act} the actuation voltage. The electric force F_e counteracts a mechanic force F_m which is described as

$$F_m = k\Delta z \tag{3-20}$$

where k defines the spring constant of the membrane and Δz the displacement towards the actuator. For small displacements, a stable condition is established for $F_m = F_e$, which makes a controllable capacitor, thus a varactor. The electric force, F_e, increases by larger displacement and will counterbalance the increased mechanical force, F_m. The needed electric force (or applied voltage V_{act}) to create a displacement Δz can be expressed as

$$V_{act} = \sqrt{\frac{2k}{\varepsilon_0 A}(d_0 - \Delta z)^2 \Delta z} \tag{3-21}$$

Equation (3-21) tells that there exists two possible displacements Δz for the same actuation voltage V_{act} lower than the certain voltage, $V_{pull-in}$. At $V_{pull-in}$ the both states coincide and instability makes the system collapse. Figure 3-15 illustrates this behavior.

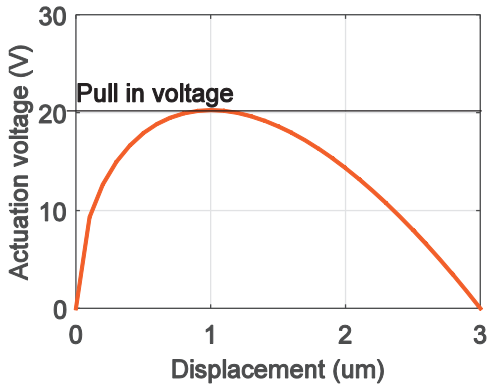

Figure 3-15 Calculated actuation voltage versus the membrane displacement according to (3-21) for the used RF-MEMS. The maximum gap for unbiased state, $d_0 = 3\ um$.

The membrane will then snap to the bottom position. This appears when $\Delta z = d_0/3$, [22], where d_0 is the maximum gap in the unbiased state. Typical values for the RF-MEMS used in this study are A=0.170 x 0.11 mm, d_0=3 µm and the needed pull-in voltage, $V_{pull-in}$=20 V. This evaluates to a spring constant of about k=8 N/m. The spring constant for a cantilever MEMS can also be calculated as [22],

$$k_c = 2Ew\left(\frac{t}{l}\right)^3 \frac{1-\frac{x}{l}}{3-4\left(\frac{x}{l}\right)^3+\left(\frac{x}{l}\right)^4} \tag{3-22}$$

where l is the total length of MEMS-membrane (170 um), and w is the width (110 um), x is the distance from the anchor edge to where the actuator force starts due to the bottom electrode (about 20 um, seen in Figure 3-16 (b)) and t the thickness of the MEMS-membrane (~2 um). The Young's modulus for gold $E = 80 \cdot 10^9\ \mathrm{N/m^2}$. That evaluates to k_c=8.5 N/m, which is approximately the same as previous calculation.

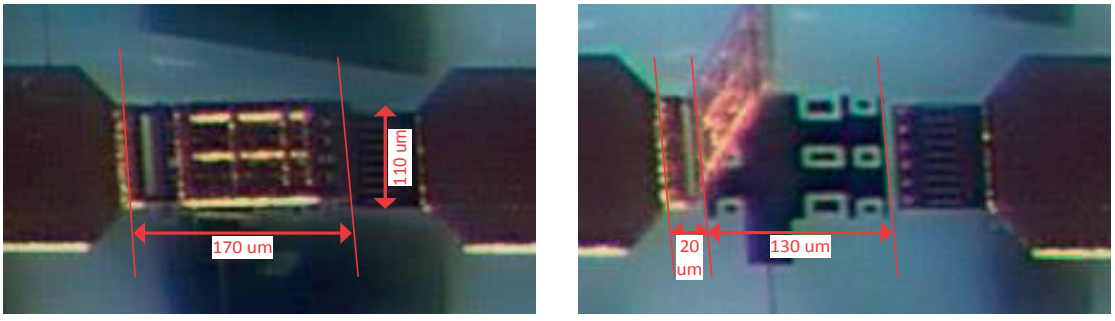

Figure 3-16 Photo of the MEMS-die element. (a) The size of membrane: 170 um x 110 um. (b) A MEMS-switch where the cantilever membrane has accidently been bent up. The actuator electrode is about 130 um x 110 um and starts about 20 um from the anchor edge to the left.

A low spring constant is necessary to decrease the needed actuation voltage, but will also result in a low restoring force and therefore may suffer from stiction problems. For high-reliability applications, the spring constant should not be designed lower than 10 N/m [22].

3.4.2 RF-MEMS model

Reflection and isolation measurements for different actuation voltage are shown in Figure 3-17 (a,b), where the pull-in voltage is seen where the first switch elements snap-in, resulting in an isolation degradation in the insertion loss graph (at about 20 V-30 V). Further increased voltage forces more switches to close. The intermediate state causes an undesired stub which changes reflection phase rapidly versus frequency and reduces the isolation.

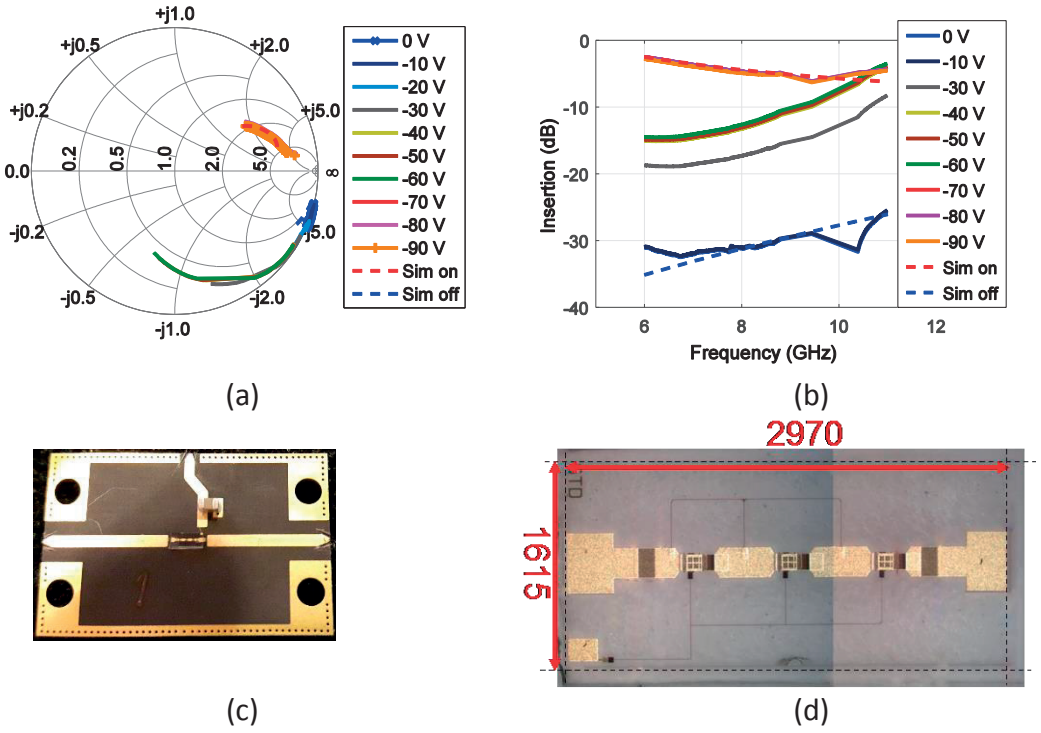

Figure 3-17 (a) Reflection coefficient for different actuation voltages. (b) Isolation for different actuation voltages. (c) Photo of the PCB test-circuit. (d) Chip photo of the MEMS, size 2970 um x 1615 um.

RF-model of the MEMS

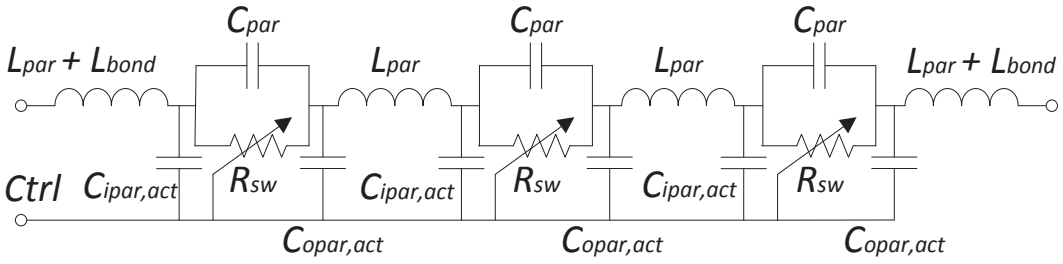

Figure 3-18 Model of the used MEMS.

The components in the model in Figure 3-18 are extracted for L_{par} and C_{par} to 0.3 nH and 22 fF, respectively, in open state. In the closed state, the line inductance, L_{par} is increased

to 0.4 nH due to a prolonged length through the switch region. The ohmic contact resistance is estimated to 1 ohm in the closed state and infinity in open state, and the included bond wires are estimated to 1 nH. The parasitic capacitance of the transmission line to the control wire are found negligible, and more, those lines have a high impedance to protect further RF-propagation.

For a two-port measurement of a serial MEMS-switch, the total parasitic capacitance in the open state can be approximated from the isolation as

$$|S_{21}|^2 = 4\omega^2 {C_{par,tot}}^2 {Z_0}^2 \tag{3-23}$$

From Figure 3-17 the measured S_{21}=-27 dB at 10 GHz in open state, and by using (3-23) it can estimate $C_{par,tot}$=7 fF, or about 21 fF per switch element which are in serial. That agrees well with C_{par} in the model in Figure 3-18.
The on-resistance in closed state can be calculated at low frequency as

$$S_{21} = 1 - \frac{R_{sw\ on,tot}}{2Z_0} \tag{3-24}$$

if the total impedance of MEMS-switch is $Z_s = R_{sw} + j\omega L$, and $\omega L \ll R_{sw}$.

RF-MEMS used in varactor application will, due to the beam instability at *1/3* of the beam displacement at the pull-in voltage, have limited capacitance ratio. Normally the capacitance ratio measures to about 1:1.25 for cantilever beams, and 1:1.4 for fixed-fixed beams. For a three-plate design, this ratio can be increased to about 1:2. However, techniques as dual-air-gap can increase the ratio further. An example in [95] shows a capacitance ratio of 1:3.

3.4.3 Electromechanic behavior

The dynamic response of the mechanical system can be described as

$$m\frac{d^2x}{dt^2} + b\frac{dx}{dt} + kx = f_{ext} \tag{3-25}$$

where x is the MEMS cantilever displacement, b the damping coefficient, k the spring constant and f_{ext} an externally applied force. This expression is useful to determine the switching speed as well as potential electroacoustic resonances.

A corresponding transfer function which models the frequency response can be written as

$$\frac{X(j\omega)}{F(j\omega)} = \frac{1}{k}\left(\frac{1}{1 - (\omega/\omega_0)^2 + j\,\omega/(Q\omega_0)}\right) \tag{3-26}$$

where the resonance frequency $\omega_0 = \sqrt{k/m_{mod}}$, and $Q = k/(\omega_0 b)$ is the quality factor of the resonant beam and m_{mod} its modal mass about 0.35 to 0.45 times the static mass. The response of (3-26) is further discussed and analyzed in [22]. If assuming $m_0 = \rho t A$, and for the used switches in this study, $\rho = 19300$ kg/m^3 (gold), membrane thickness

t =3 µm, and A =0.170 x 0.11 mm, evaluates to $m_0 = 1.0 \cdot 10^{-9}$ kg. By using the earlier estimated spring constant of 8 N/m from the pull-in voltage measurement, electroacoustic resonance can be calculated to $\omega_0 = 137 \cdot 10^3$ rad/s, or 21 kHz.

The mechanical resonance is more obvious in the open state than in the closed state. Figure 3-19 (a) shows the noise hump appearing at slightly above 10 kHz in the open state of the MEMS with 12.3 %tuning running at a center frequency of 10 GHz. Compared to the phase noise for the closed state in Figure 3-19 (b) the resonance has diminished.

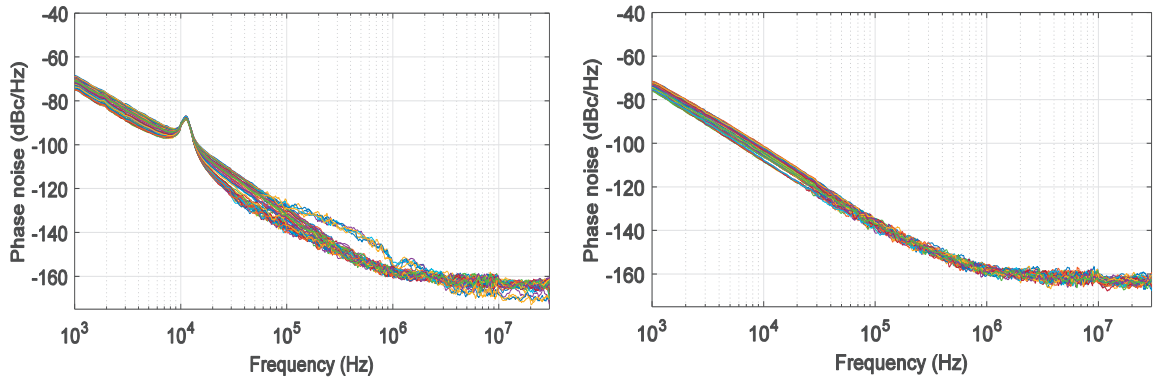

Figure 3-19 Phase noise of a MEMS-tuned cavity oscillator with a three-row MEMS configuration measured at different bias level versus offset frequency as reported in Paper [A]. (a) All switches are in the open state. (b) All switches are in the closed state.

3.4.4 Potential improvements of used RF-MEMS

This study has found some issues and suggested improvements for the used RF-MEMS and they are discussed below.

Stiction

The stiction issues and fastened MEMS-membranes became a severe problem during the analysis. As several switch elements were biased in parallel with a considerable spread in pull-in voltage, between 20 V to 90 V, the highest voltage was used to enable all elements to the closed state. That implied a risk for causing bonding effect and damaging the membrane for those with lower pull-in voltage. Non-conductive capacitive MEMSs, which probably are more robust for permanent stiction, are in that perspective preferred.

Resonances

Electroacoustic resonance was found for the MEMS in particular in the open state, due to lack of mechanical stability for the membrane in this position. A redesign of another top electrode to fix the membrane for the open position would partly solve this problem.

More holes in the membrane and therefore a decreased modal mass would decrease the switching time or increase the resonance frequency and probably make it less sensitive for acoustic vibrations. The effect of the squeeze film damping is also reduced with holes in the membrane which would further decrease the switching time.

Reliability

A capsulated RF-MEMS would be preferred to avoid contamination of glue and solder paste in the assembly processes.

The MEMS-switch could be designed to cover an analog tuning as a varactor. In this case, a combined technology could enhance for both PLL-locking and digital sub-band control.

3.5 Tuning components and technology comparison

Different high-Q tuning techniques compared to methods used in this study are presented in Table 3-2, regarding tuning range and unloaded Q-factor. In oscillator applications, other aspects as power handling, power loss, or vibration sensitivity must also be considered. Semiconductor varactor tuning has previously been discussed with drawbacks of large-signal degradation of Q-factor when strong coupling and high RF-power are applied. RF-MEMS varactors are robust for high power, but suffers from poor vibration robustness and may have non-continuous tuning characteristic due to the pull-in voltage.

Table 3-2 Comparison of different high-Q tuning techniques

Ref	fc (GHz)	Tuning-ratio (TR) (%)	Q_0	Technology
[96]	32.5	10		Ferroelectric
[43]	3	67		YIG
[97]	1	28	65	Varactor diode
[98]	12.5	1.23	150	SIW and switchable varactor diode
[91]	3.45	90	300-650	SIW and 3D MEMS varactor/switch
[92]	4.8	33	300-500	SIW and MEMS varactor/switch
[99]	6.425	5.4	140-240	SIW and MEMS varactor/switch
[100], [74]	3.475	6		MEMS varactor
[101]	23	5	750-1450	MEMS cantilever
Paper [A]	10.065	2.1	700-1115	MEMS digital (2 steps), one row@1 mm
Paper [A]	9.915	8.1	400-500	MEMS digital (2 steps), one row@2.5 mm
Paper [A]	10.085	5	700-1123	MEMS digital (8 steps), three rows@1 mm
Paper [A]	10.035	12.3	250-826	MEMS digital (8 steps), three rows@2.5 mm
Paper [G]	10.2	1.5	300-650	Varactor diode, two rows@1 mm depth
Paper [G]	10.4	2	300-400	Varactor diode, two rows@2.5 mm depth

Chapter 4.

Oscillator Design and Characterization

This section describes the oscillators designed and analyzed in this study. Considerable efforts are spent on how to optimize the phase noise given the discussed boundary conditions. Critical conditions for the active device are, as earlier mentioned, the power handling capacity and RF noise figure. Therefore, GaN has followed as a good choice, which has been the used technology for all designs. Furthermore, a high-quality resonator is needed, which in the first design is implemented with a cavity and discussed in Chapter 4.2.1. A design with a hybrid technology implemented with a discrete LC-network is shown in Chapter 4.3. Besides the importance of a high unloaded quality-factor, the resonator has to be optimally coupled to take advantage of its potential, which is studied throughout all oscillator designed. A MMIC-oscillator achieves the optimum coupling by utilizing an impedance transformed quasi-lumped resonator to match the gain of the amplifier as is shown in Chapter 4.4.1. A different approach to match the power coupling to the resonator is by adjusting the gain of the amplifier. Chapter 4.4.2 demonstrates an electronically adjustable reflection amplifier.

A digitally tunable cavity oscillator using an electronically movable ground plane of MEMS-switches with minor degradation of the performance is discussed in Chapter 4.2.2. Analog tuning by using an additional tuning element of semiconductor varactors is discussed in Chapter 4.2.2.

4.1 Experimental setup

Phase noise measurements have been performed with the PLL-method, using a commercial signal source analyzer from Rohde & Schwarz, FSUP50 [102]. Figure 4-1 shows a block diagram of the PLL-method. Only free-running oscillators are tested in this study.

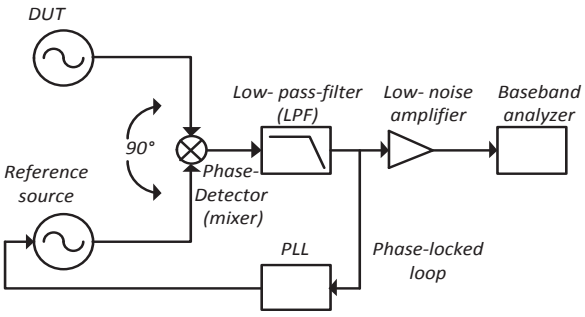

Figure 4-1 A block diagram is showing the used PLL-method [103].

The noise floor in the instruments may limit when measuring high-performance oscillators, in particular at a high carrier frequency. Table 4-1 shows the typical phase noise performance for the used FSUP50 for different offset and carrier frequencies. An important test condition in this study is at 100 kHz offset frequency at 10 GHz carrier frequency. The instrument performance at this condition is not sufficient to measure the cavity oscillator reported in Paper [C].

Table 4-1 FSUP50 phase noise sensitivity versus input frequency and offset [102].

Offset frequency	Input frequency and Input level +10 dBm<, Typical values R&S®FSUP50 (dBc/Hz)				
	10 MHz	**100 MHz**	**1 GHz**	**10 GHz**	**40 GHz**
1 kHz	-161	-160	-134	-116	-106
10 kHz	-168	-168	-143	-126	-114
100 kHz	-170	-176	-158	-138	-126
1 MHz	-175	-177	-165	-150	-140
10 MHz		-179	-172	-167	-155
30 MHz			-172	-170	-159

To improve the noise floor in the measurement system, two nearly identical oscillators are used as is illustrated in Figure 4-2. One of these is slightly shifted in frequency, and the phase noise measurement is performed on the down converted and significant lower IF-frequency, which in our study is around 30 MHz.

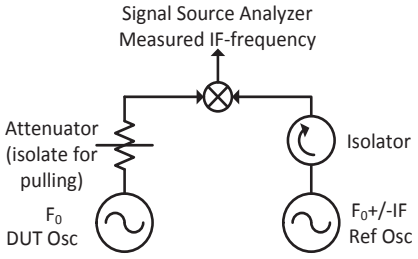

Figure 4-2 Setup of mixed measurement.

The effect of combining to equal and uncorrelated oscillators is 3 dB extra noise contribution. The measured noise figure on the down-converted signal has to be afterward compensated.

4.2 Cavity based oscillators

A cavity based oscillator is using a testfixture containing a MMIC reflection amplifier on a PCB for connecting the resonator. The resonator is varied in different designs, as implementation for fixed frequency, or enhancing tunability by RF-MEMS-switches or by varactors.

4.2.1 Fixed frequency

The resonator for fixed frequency is simply an empty aluminum cavity dimensioned for the TE_{101}-mode. The cavity is placed on top of an exciting microstrip line connected to a

reflection amplifier. The amplifier is a MMIC-amplifier designed in a 0.25-µm GaN-HEMT process at TriQuint 3MI process. Figure 4-3 (a) shows a photo of the oscillator with the cavity and Figure 4-3 (b) shows a schematic.

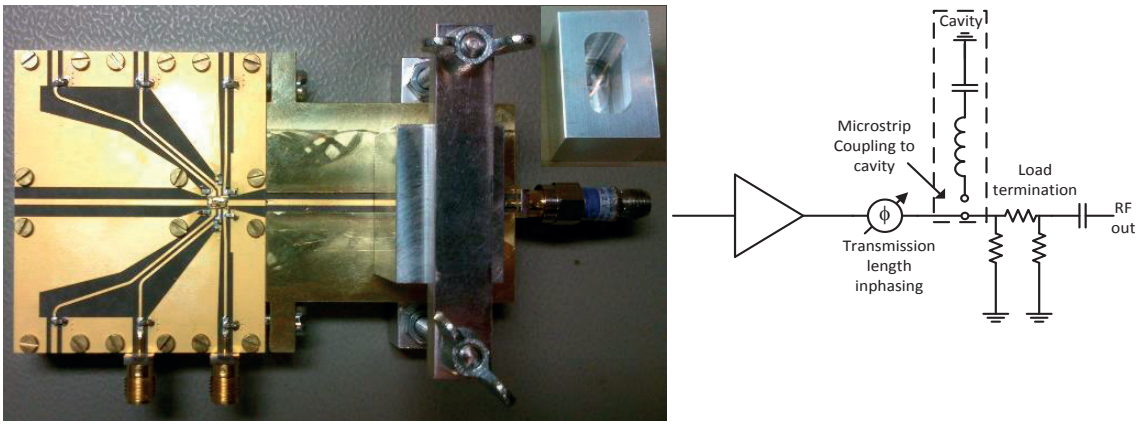

Figure 4-3 (a) Picture of the cavity oscillator. (b) Schematic.

The setup is very flexible to adjust the cavity coupling by changing the perpendicular position to the microstrip line, and the phase condition by sliding the cavity along the strip. The oscillation frequency is about 10 GHz.

Table 4-2 shows the phase noise performance at 100 kHz and 400 kHz, respectively, for different cavity positions and open loop gain. The best performance is achieved for the weakest coupling with an open loop gain close to unity. Reason is that high gain will force the amplifier in deep compression, which is not beneficial for up-converted flicker noise and thermal noise.

Table 4-2 Measured phase noise versus coupling of the resonator

Cavity position offset (mm)	R_s/loss (Ω)/(dB)	Optimum phase noise performance @100 kHz (dBc/Hz) @bias level (V_d/V_g)	Phase noise @400 kHz (dBc/Hz)	FOM[1] @400 kHz (dB)	F_{op}[2] @400 kHz (dB)	Gain (dB) Reflection Amp @ opt for 100 kHz bias (V_g/V_d)	$\lvert R_N \rvert$[3] (Ω)	$\frac{R_S}{\lvert R_N \rvert}$	Open loop gain[4] (dB)
0.6	8.1/2.8	-139 @4/-1.9	-152.5	219	15	6.8	18.7	0.4	4
3.4	14/5	-141@4/-1.8	-155.5	223	10	7.0	19.1	0.7	2
3.9	19.2/7	-141.5@5/-1.6	-156	221	9	8	21.6	0.89	1
5.9	**20/7.4**	**-144.5@5/-1.8**	**-160**	**227**	**7**	**7.9**	**21.3**	**0.94**	**0.5**

(1) $FOM=-\mathcal{L}(\Delta f)+20\log(f_0/\Delta f)-10\log(P_{DC}/1mW)$

(2) $F_{op}=173.9+10\log[8\eta\beta/(1+\beta)^3]+20\log(Q_0)-FOM$

(3) The negative resistance is the real part after phase compensation to a serial resonator in 50 ohm system.

(4) $G_{loop}=20\log|(R_s-Z_0)/(R_s+Z_0)|+20\log|(-|R_n|-Z_0)/(-|R_n|+Z_0)|$

The phase noise for the optimally coupled resonator is shown versus bias at 100 kHz offset in Figure 4-4 (a) and versus offset frequency for optimum bias in Figure 4-4 (b). Optimum *FOM* at 400 kHz offset is measured to 227 dB. Under the same optimum condition, the power was +5 dBm, the power consumption P_{DC}=200 mW, and the flat noise floor -165 dBc/Hz.

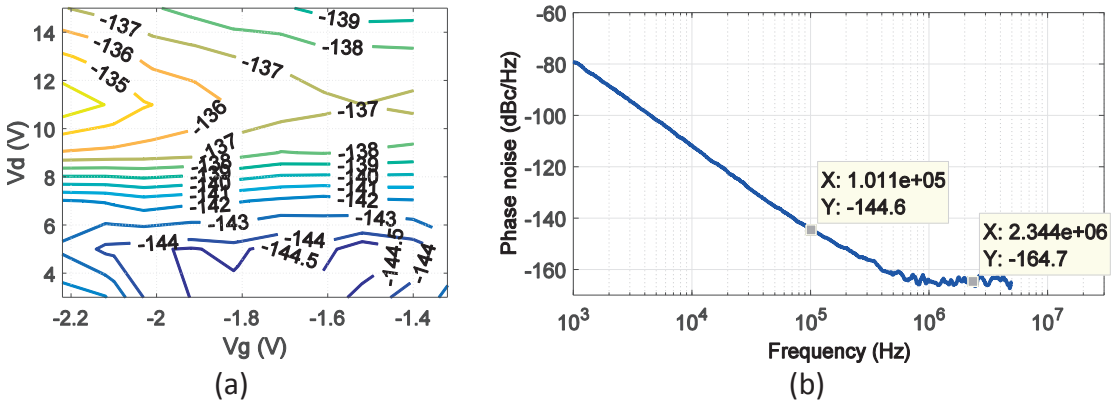

Figure 4-4 (a) Phase noise in dBc/Hz at 100 kHz offset versus bias. (b) The phase noise for best bias versus offset frequency.

The phase noise of this oscillator is below the noise floor of the instrument used for measurement. Therefore, the setup proposed in Chapter 4.1 with two equally oscillators for down-converting the signal was used. Once the best achievable performance of the two equally tuned and biased oscillators is determined, one of these oscillators is kept fixed at this condition as a reference oscillator. Different test conditions have been applied to the other oscillator. The measured results are compensated for the noise floor of the reference oscillator. Figure 4-5 shows a photo of the test setup.

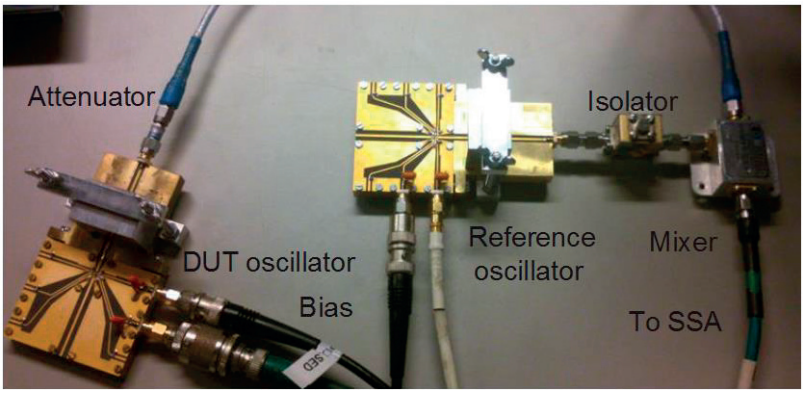

Figure 4-5 Photo of the experimental setup

The design is further analyzed in Paper [C].

4.2.2 Tunable frequency

The frequency tunability for the resonator on the first design is implemented by a tunable ground plane inside the cavity of an intruded PCB of MEMS-switches. In the second design, semiconductor varactors coupled to the E-field are assembled on the PCB.

Figure 4-6 shows a sketch of the complete setup of the MEMS-tuned oscillator, with the intruded PCB illustrating the positions of the MEMS-switches and a schematic of the setup. The setup is further demonstrated in Paper [B].

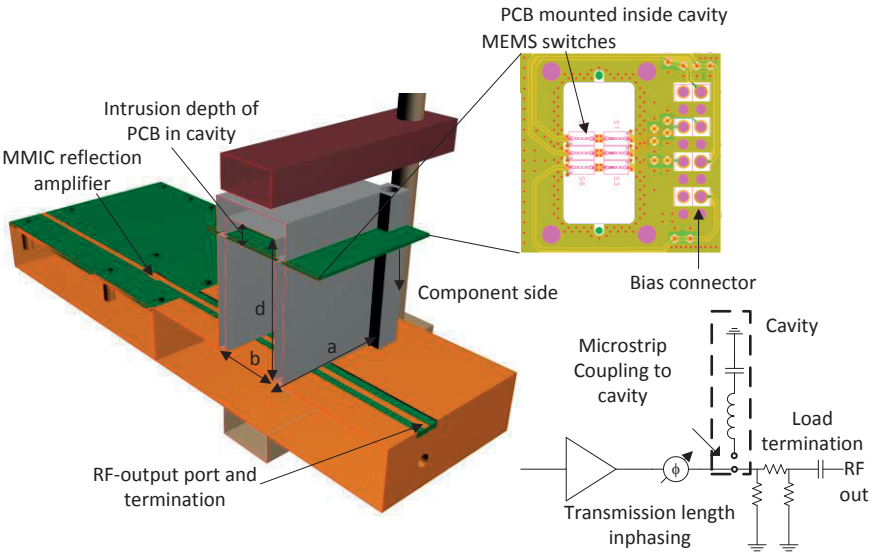

Figure 4-6 Cross section sketch of the setup of a cavity oscillator with RF-MEMS-switches forming an electronically tunable wall.

Different assembly alternatives of the switches, for a one-row configuration and a three-row configuration are shown in Figure 4-7 (a-b), respectively. Figure 4-7 (c) shows a photo of the completely assembled PCB.

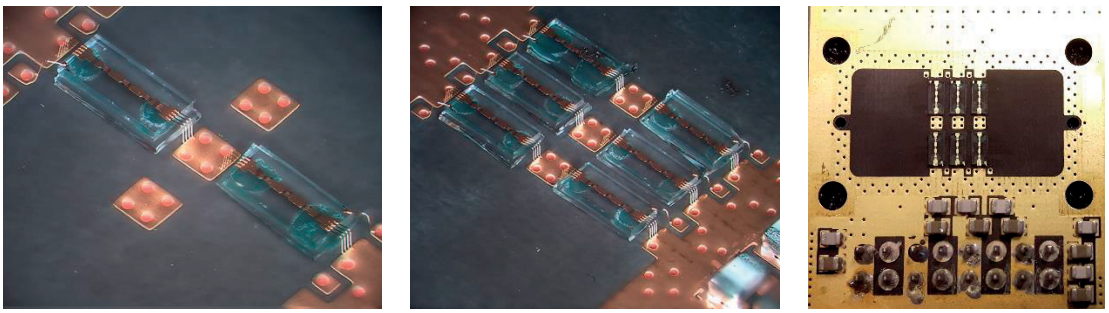

Figure 4-7 Photo of the assembled switches and PCB. (a) One-row configuration. (b) Three-row configuration. (c) A layout of the PCB. The cavity opening is 20.7 mm x 10.35 mm.

The positions of the MEMS-switches, by varying the intrusion depth of the PCB (1 mm and 2.5 mm) and the configuration on it (one row or three rows) are analyzed with trade-offs for tuning-range, frequency resolution, Q-factor and phase noise. The oscillation frequency is about 10 GHz. Figure 4-8 shows a summary of the studied setups with frequency tuning versus the bit position of the MEMS-states.

Table 4-3 shows a more detailed analysis of the performance.

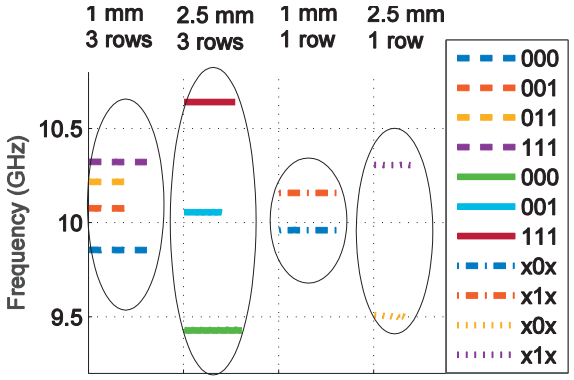

Figure 4-8 Summary of the studied MEMS-configurations versus oscillation frequencies. State "0" equals open MEMS-state, and "1" equals closed MEMS-state, for the assembled positions, respectively. State "x" denotes a not assembled position.

Table 4-3 Tuning range, Phase noise and Q-factor, versus simulations for different MEMS-setup.

Setup	State	Measurement						Simulation		
		Q_0	Freq (GHz)	Tuning ratio Increase/state and total (%)(***)		Optimum Phase Noise @100kHz (dBc/Hz)	Optimum Phase Noise @1MHz (dBc/Hz)	Q_0	Freq (GHz)	Tuning ratio (%)(***)
One-row MEMS @1 mm depth.	x0x	1115	9.96	+0	2.1	-140	-159	2309	9.96	2.0
	x1x	700	10.17	+2.1		-139	-160	913	10.16	
One-row MEMS @2.5 mm depth.	x0x	400	9.51	+0	8.2	-126	-149	2377	9.65	6.7
	x1x	500	10.32	+8.2		-128	-158	775	10.32	
Three-row MEMS @1 mm depth.	000	1050	9.84	+0	5	-139	-160	1545	9.84	4.8
	001	700	10.07	+2.3		-134	-160	702	10.08	
	011	700	10.22	+1.5		-129	-158	718	10.22	
	111	1123(*)	10.33	+1.1		-140	-159	675	10.32	
Three-row MEMS @2.5 mm depth.	000	300	9.42	+0	12.3	-126	-154	1313	9.32	13.3
	001	250	10.05	+6.5		-123	-153	510	10.05	
	011	350	10.43	+3.7		N/A(**)	N/A(**)	700	10.44	
	111	826(*)	10.65	+2.1		-133	-159	821	10.65	
Empty PCB @1 mm depth.		1817	9.998			-140	-160	3000	9.998	
Empty PCB @2.5 mm depth.		1602	9.925			-140	-160	3000	9.941	
Empty cavity Paper [C]		3800	9.93			-145	-165	4000	9.93	

(*) Lower on-resistance measured than assumed in the model.
(**) Too low loop gain to measure with the used amplifier.
(***) Tuning range is defined as $2(f_{max}-f_{min})/(f_{max}+f_{min})$

From Table 4-3 it is obvious that the tunability increases by the intrusion depth of the PCB, and consequently degrades the phase noise performance. The tuning also compresses, when the number of MEMSs set in the closed state are increased. This is probably due to more distorted RF-field, which complicates the positioning of the MEMS to achieve a

uniform frequency resolution versus the states. However, the concept of using MEMS-switches to tune the ground plane inside the cavity works in general with good result. They can be used for digital control of the resonance frequency over a quite broad range, 12 % with phase noise performance in the range of -133 dBc/Hz to -123 dBc/Hz at 100 kHz offset frequency. *FOM* and FOM_T are 196 dB and 198 dB, respectively. These results are further analyzed and reported in Paper [A].

Another oscillator is based on a varactor-tuned cavity which is analyzed in Paper [G]. The varactors are assembled with similar techniques as reported in Paper [A], on a PCB intruded inside the cavity. Figure 4-9 shows a picture of the complete setup and including sub-blocks.

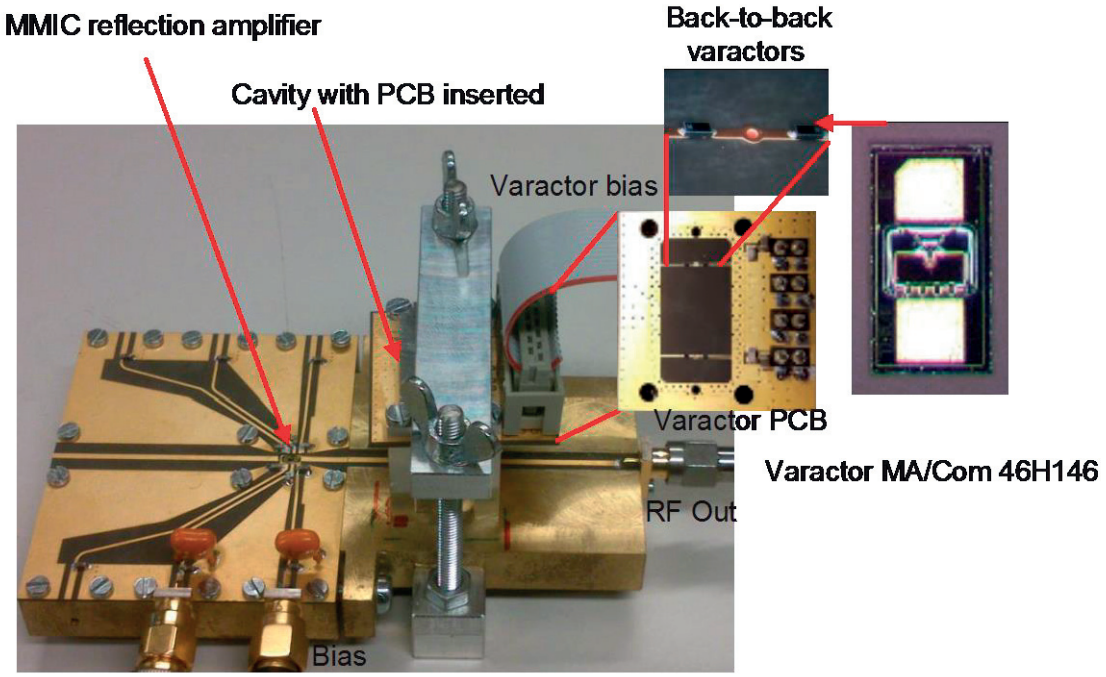

Figure 4-9 Picture of the oscillator for a varactor-tuned cavity.

The varactors are aligned with the E-field, and their capacitance increases the electrical length of the waveguide, which is short-circuited at the end by a lid. A model of the tuned cavity was discussed in Chapter 3.3.3.

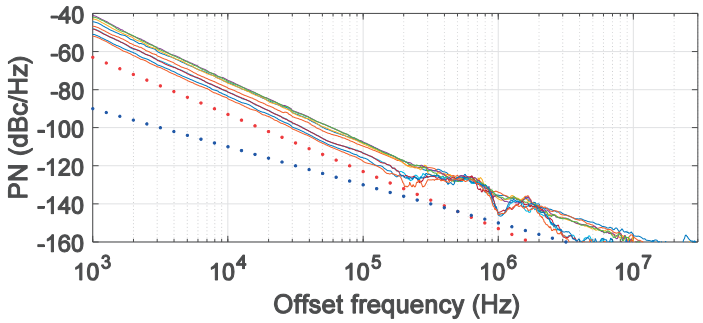

Figure 4-10. Varactor cavity at 1 mm depth. Phase noise (dBc/Hz) versus varactor voltage (-20 V to -0.1 V) for optimum bias V_d/V_g=11.5 V/-1.8 V. Support lines for -20 dB/dec and -30 dB/dec are added.

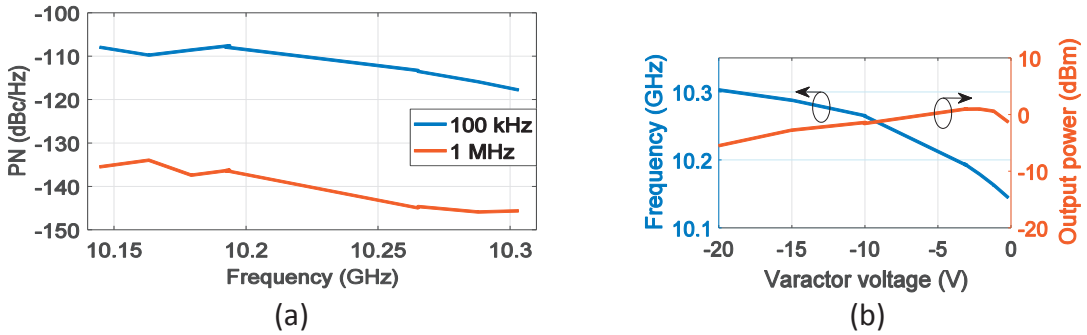

Figure 4-11. Varactor cavity at 1 mm depth. (a) Phase noise at 100 kHz and 1 MHz offset frequency, respectively, versus frequency for optimum bias V_d/V_g=11.5 V/-1.8 V. (b) Frequency and output power versus varactor voltage.

Figure 4-10 shows the phase noise versus offset frequency. The varactor voltage is swept from 0 to -20 V. Figure 4-11 (a) shows phase noise versus oscillation frequency at offset frequencies of 100 kHz and 1 MHz, at the bias point V_d/V_g=11.5 V/-1.8 V. For offset frequencies lower than 200 kHz the flicker noise contributes to a -30 dB/decade slope. At offset frequencies in the range 200 kHz to 1 MHz thus for the -20 dB/decade region, the phase noise variation is minor affected versus varactor voltage and tuning sensitivity. This indicates that the modulation noise is less dominating, which otherwise should have strong effect in this region. However, the change in varactor bias and tuning frequency influence on the total Q-factor due to the large-signal degradation, which contributes to the overall variation in the phase noise. Figure 4-11 (b) shows the tuning frequency and the output power versus varactor voltage for the optimum bias, V_d/V_g=11.5 V/-1.8 V. The best phase noise is measured at the most reversed varactor voltage, thus at less large-signal degradation of Q due to most margin for RF-voltage across the varactors and most power capability.

The optimum phase noise at 100 kHz offset and 1 MHz offset, respectively, measures -118 dBc/Hz and -146 dBc/Hz. The measured small signal Q_0=400, which can be scaled to the Q_0-factor of the fixed frequency cavity oscillator in Paper [C] with expected 20 dB lower phase noise. A deviation in further degradation of 7 dB from this value indicates that the phase noise is not primarily limited by the unloaded Q_0 of the cavity but rather by modulation noise proportional to the tuning sensitivity and large-signal effects. Previously, Chapter 2.6.1 discussed the power dependent Q-factor due to the RF-voltage limitation across the varactors. Further, the measured oscillator has higher bias current and gain for loss compensation at optimum, which introduces more flicker noise, in particular at 100 kHz offset.

4.3 Flexible hybrid oscillator

An oscillator was developed as a testbed to use LF-noise characterized devices in an oscillator setup. The oscillation frequency is 1 GHz, and phase noise is studied versus offset frequency and bias level.

A hybrid oscillator based on GaN-HEMT device and a lumped element resonator implemented on a low loss PCB has been designed. A photo and a schematic are shown in Figure 4-12 (a) and Figure 4-12 (b), respectively. The testbed is made flexible so that a bare die transistor device can be close connected between two pieces of PCB, one with the

termination network on the gate side, and one with different resonator topologies on the drain side. R_{stab} is for stabilization and suppresses out-of-band resonances.

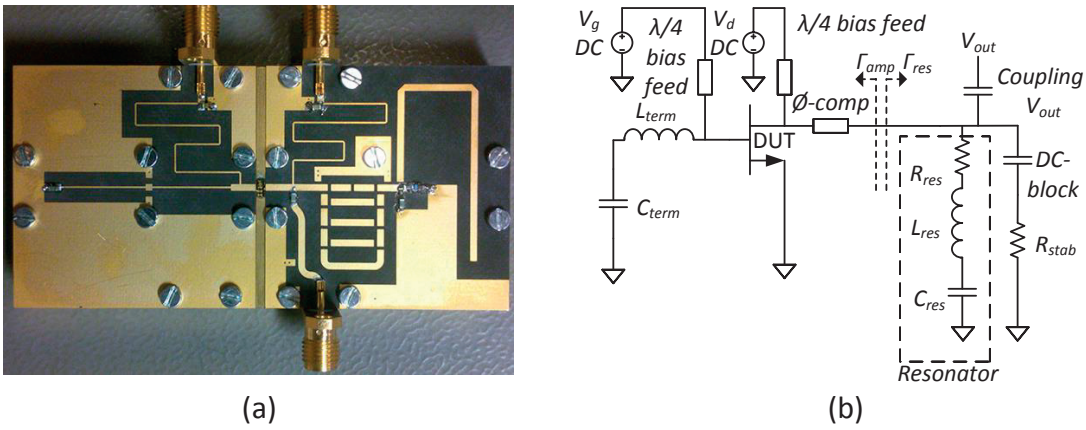

Figure 4-12 (a) Photo of the hybrid oscillator. (b) Schematic.

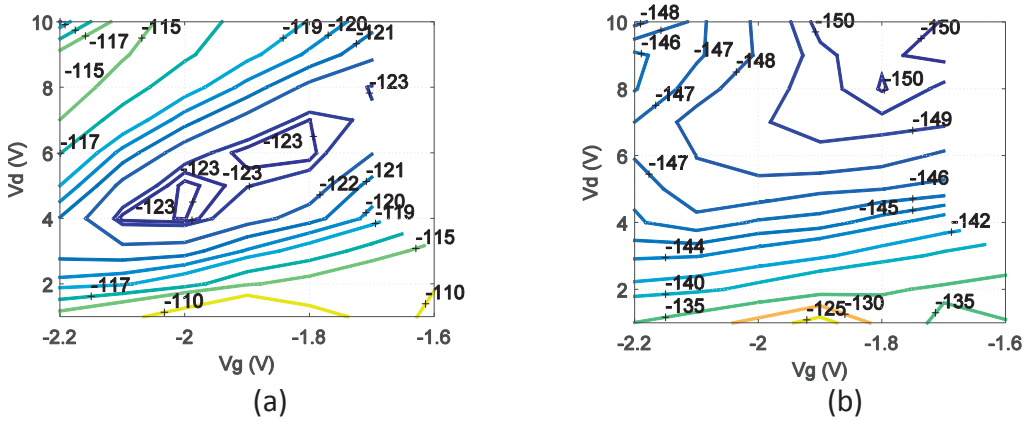

Figure 4-13 Measured phase noise in dBc/Hz versus bias level for different offset frequency. (a) 100 kHz offset frequency. (b) 1 MHz offset frequency.

Figure 4-13 (a) and (b), respectively, show measured phase noise at 100 kHz and 1 MHz. It is found that at 100 kHz offset, the performance is limited by flicker noise, and stays essentially constant if power is increased. Thus, the benefits with higher power level counterbalance the increased flicker noise at higher current. At 1 MHz, the increased signal power due to higher bias level is beneficial for the phase noise.

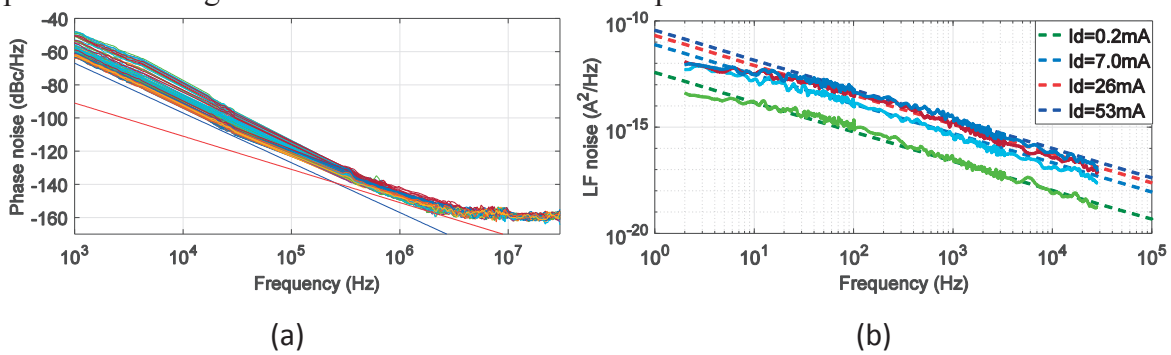

Figure 4-14. (a) Measured phase noise is shown. Support lines for -20 dB/decade and -30 dB/decade are added. (b) Measured LF noise is shown of the used 8x50 um GaN at V_d=10 V for different I_d versus simulation.

Figure 4-14 (a) shows measured phase noise for all swept bias level, and Figure 4-14 (b) shows measured LF-noise, fitted to a simulation model, with k_F=6×10^{-10} , A_F=0.87, and F_{fe}=1.5 according to (2-11). The noise floor for this component is quite low, compared to the thermal noise current of a 50 Ω resistor that measures $3 \cdot 10^{-22}$ A^2/Hz. Optimum phase noise is measured for an open loop-gain around 1.5 dB, and the equivalent loss resistance in the serial resonator is about R_S=11 Ω or -4 dB, and Q≈49. The measured reflection gain for the transistor at optimum bias V_d/V_g=5V/-2V is about 5.5 dB, or a corresponding $|R_N|$=15 Ω and $R_S/|R_N| = 0.7$.

At 1 MHz offset frequency, a phase noise of -150 dBc/Hz is measured from 1 GHz oscillation frequency, and a power-normalized figure of merit (FOM) of 186 dB is reached. The noise figure F=21 dB, out of which 2-3 dB is dependent on a none-optimum coupling, and 2 dB due to a DC to RF-efficiency of 65 %. The noise figure compensated for the finite efficiency and none-optimum coupling is 17 dB. The results are further analyzed in Paper [F].

4.4 MMIC based oscillators

This work presents two MMICs, one integrated oscillator discussed in Chapter 4.4.1, and one reflection amplifier with electronic gain control intended for an external resonator discussed in Chapter 4.4.2.

4.4.1 Integrated oscillator

The design uses the same active transistor as the previously presented reflection amplifier for the cavity oscillators and is integrated to a 15 GHz on-chip resonator. The resonator is implemented as a parallel resonator, that is transformed by a quarter-wavelength transformer and adjusted to fulfill the phase condition. Figure 4-15 (a) and (b), respectively, show a chip photo and a schematic of the oscillator.

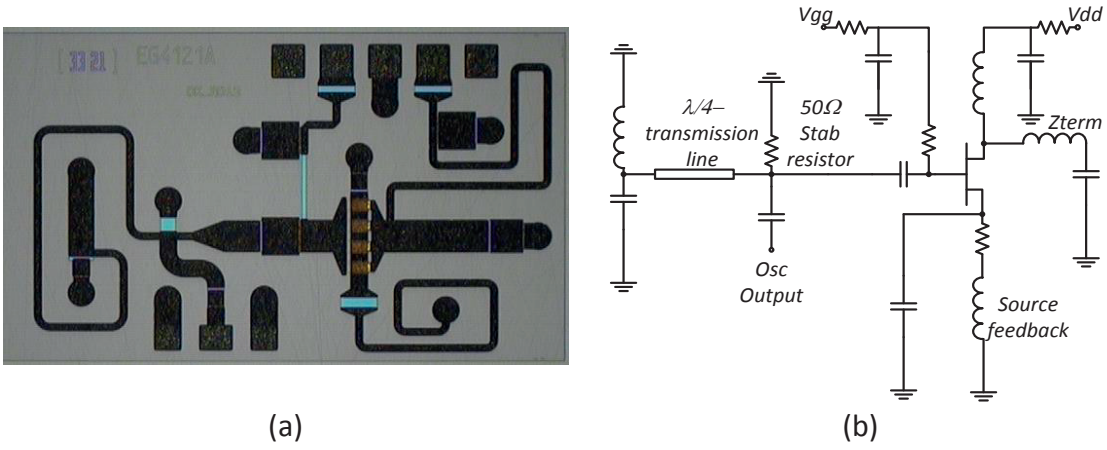

Figure 4-15 (a) Chip photo of the oscillator, size 2.0x1.0 mm. (b) Schematic.

The transformer gives flexibility to match the coupling factor, or the impedance, to the active device. Matching the gain of the amplifier, or equivalently the negative resistance R_N, to the equivalent serial resistance R_S of the resonator according to (2-45) and (2-47),

is difficult by scaling the width of an open quarter-wavelength microstrip stub. Schematic of such resonator is depicted in Figure 4-16 (a), and calculation of achievable R_S is

$$R_S \approx \frac{c_0}{4W}\sqrt{\frac{\pi\mu_0}{\sigma\varepsilon_r f}} \tag{4-1}$$

where c_0 is the free space velocity, ε_r relative permittivity, μ_0 permeability, W is the width of the microstrip line, σ the metal conductivity, and f the frequency. If connected to a lumped parallel resonator as a quarter-wavelength transformer shown in Figure 4-16 (c), the dimensions will be more feasible for the lumped resonator as

$$L = \frac{Z_C^2}{R_s\omega_0 Q} \tag{4-2}$$

$$C = \frac{R_s Q}{Z_C^2\omega_0} \tag{4-3}$$

where L and C are the corresponding lumped resonator components and Q-factor to achieve a certain R_s using a transformer with characteristic impedance Z_c. Another topology to match the coupling can be achieved by a coupled $\lambda/2$ resonator as in Figure 4-16 (b). The separation between lines in the coupler-resonator can be used to set the desired coupling factor. However, the topology is quite area consuming.

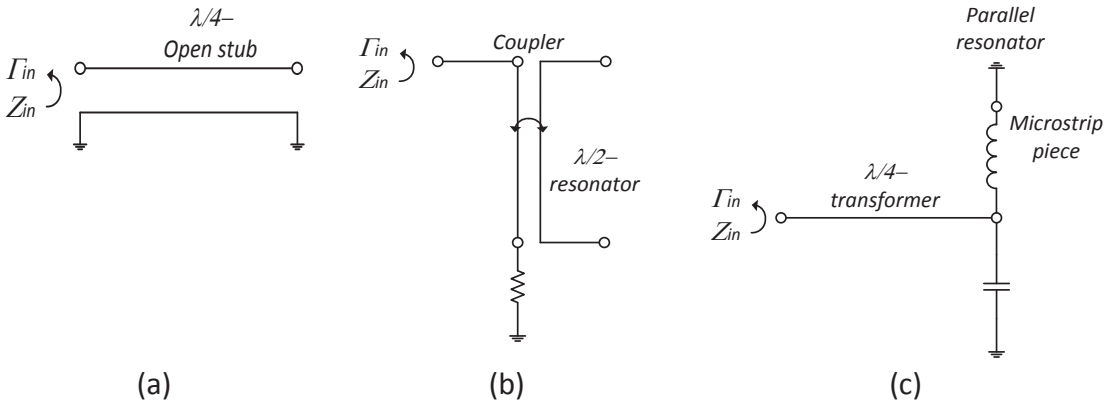

Figure 4-16 (a) Open quarter wavelength stub-resonator. (b) Coupler-resonator. (c) Transformed resonator.

Phase noise results from the oscillator with the transformed resonator is shown in Figure 4-17 (a-b), versus offset frequency for all measured bias, and at a fixed offset of 100 kHz versus bias, respectively. The optimum phase noise measures -106 dBc/Hz at 100 kHz for an oscillation frequency of 15 GHz with a corresponding FOM=191 dB. The results are further reported in Paper [E].

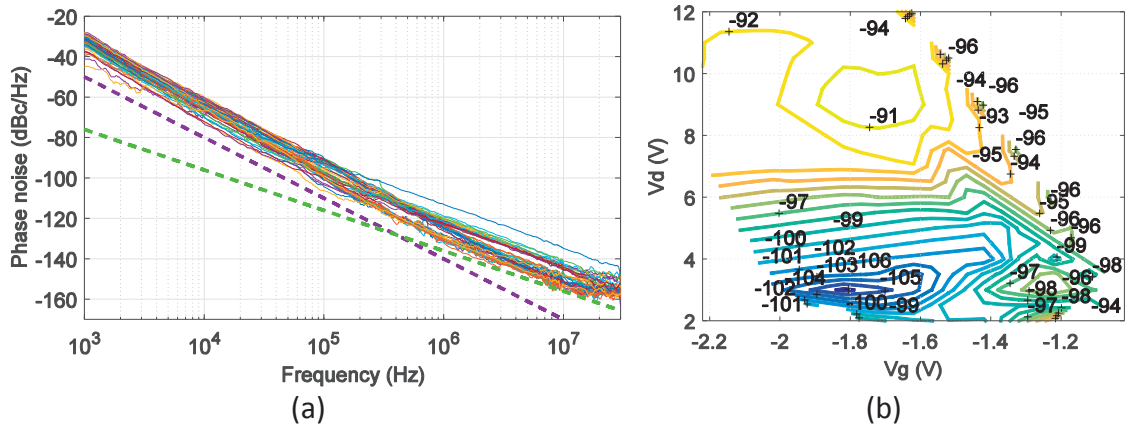

Figure 4-17 (a) Phase noise (dBc/Hz) versus offset frequency for all bias is shown. Support lines for -20 dB/decade and -30 dB/decade are added. (b) Phase noise at 100 kHz offset versus bias is shown.

4.4.2 Reflection amplifier with adjustable gain

An oscillator with the feature to optimize the resonator coupling by adjusting the gain of the reflection amplifier is reported in Paper [D]. The two different methods by optimizing the gain in comparison to a change in the coupled impedance of the resonator was discussed earlier in Chapter 2.5.2. The amplifier is made for 8.5 GHz, with an adjustable gain between 0 dB to +7 dB, and it is designed and fabricated in a 0.25-µm GaN-HEMT process at UMS, GH25-10 process.

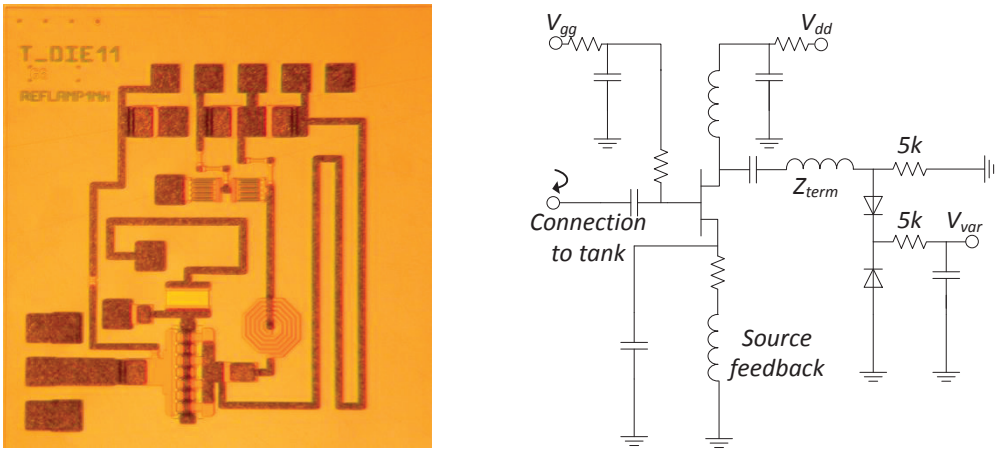

Figure 4-18 (a) Photo of the reflection amplifier, size 1.0 mm x 1.0 mm. (b) Schematic

A connected cavity locks the frequency to 8.5 GHz, and for different varactor voltages, the reflection gain is changed along the black line in Figure 4-19 (a). Figure 4-19 (b) shows the corresponding phase variation at the fixed frequency of 8.5 GHz, which is less than +/-10 deg, and have minor impact on the resonator phase condition.

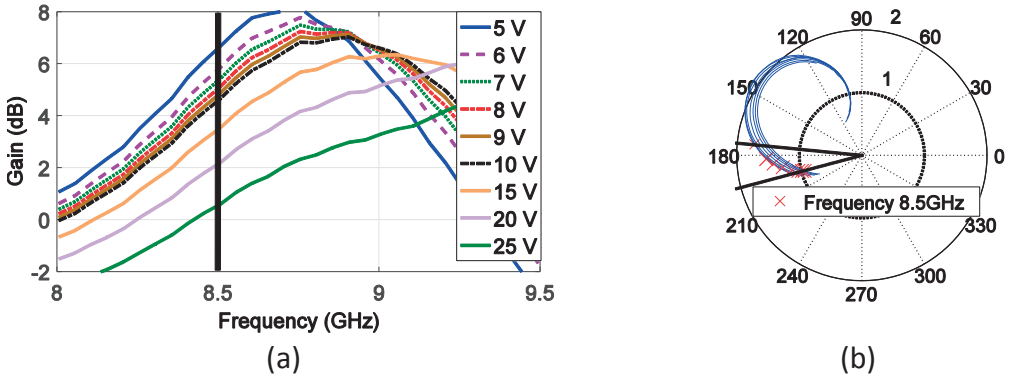

Figure 4-19 (a) Magnitude of the reflection gain versus varactor voltage. (b) Polar plot of the reflection gain.

In Figure 4-20 (a), the starting position is a strong coupling (low R_s) which means that the amplifier gain $-R_N$, has to be lowered by a higher varactor voltage, compared to the situation in Figure 4-20 (b). In Figure 4-20 (b) the starting position of the cavity is weak coupling ($R_s \approx |R_N|$), and the gain increases with a lower varactor voltage. In both cases the optimum phase noise performance appears at the same bias level, showing that the gain tuning has a minor impact on the bias level of the active transistor.

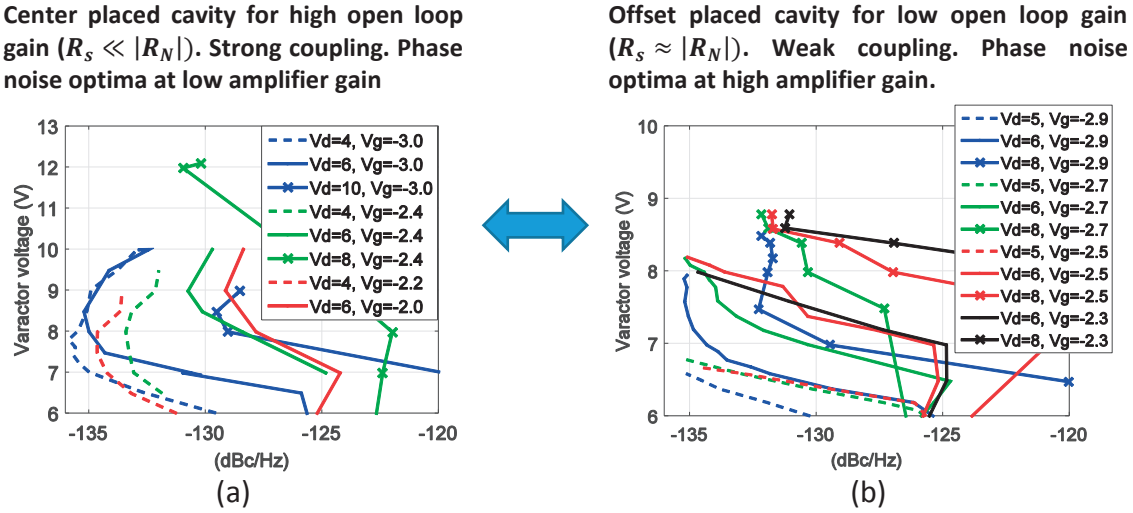

Figure 4-20 Two different cases of resonator coupling discussed in Paper [D].

The minimum phase noise reached for optimum gain setting is -136 dBc/Hz, which can be compared to -139 dBc/Hz that was obtained with the mechanical tuning of the resonator impedance, i.e., by moving the cavity. Despite the slight degradation due to the electronically controlled circuitry, the design is motivated as it easily can be made adaptive to compensate for process and temperature variations. The loop-gain can also be adjusted to ensure a proper start-up condition, and then be optimized for the stationary condition. FOM at 100 kHz for an electronically gain control and manual gain control measures to 212 dB, and 215 dB, respectively.

Chapter 5.

Conclusions

The thesis has demonstrated optimization of oscillators targeting low phase noise. Choice of technology for the active device and the resonator is important, but as crucial is to utilize and combine the included parts to form a well-designed oscillator. Parameters as the power capacity, RF noise floor, and flicker noise for the amplifying part and the unloaded quality-factor for the resonator circuitry set boundaries for the theoretically achievable performance.

In this work, an effective noise figure is defined to measure the performance against the theoretical noise level. It has been shown that the performance in the 20 dB region is limited by the Q-factor and the DC-power efficiency. This means that the commonly used power-normalized figure-of-merit figure, *FOM*, is only limited by the unloaded quality-factor of the resonator and the thermal noise floor. To reach the noise floor, the resonator must be optimally coupled to the active device, which means a trade-off between power coupled to the resonator and loaded Q-factor. Experimentally, the optimal coupling factor is found to be $\beta=1$, in contrast to $\beta=1/2$ which is predicted by a small-signal linear model. One reason for the deviation is that the model does not consider non-linear noise up-conversion.

The thesis reports on several state-of-the-art oscillators. A cavity based oscillator shows an excellent phase noise of -145 dBc/Hz at 100 kHz from a 9.9 GHz oscillation frequency. A MMIC oscillator demonstrates a phase noise of -106 dBc/Hz at 100 kHz from a 15 GHz carrier. The two oscillators present an effective noise figure of about 16 dB above the theoretical noise floor. A substantial contribution to the effective noise figure is the finite DC to RF efficiency, which for the cavity oscillator and MMIC oscillator measures around 6 % and 8 %. Compensation for the efficiency shows operational noise figures for the cavity oscillator and MMIC-oscillator of 4 dB and 5 dB, respectively, extracted in the $1/f^2$ region.

One of the factors most critical for the operational noise figure is the resonator coupling factor, which may be tuned in different ways, e.g., mechanically or by changing the bias condition to control the gain of the reflection amplifier. The thesis also reports on a reflection amplifier with separate electronic gain control. It demonstrates electronic tuning with phase noise within 3 dB from the performance of a mechanically tuned cavity oscillator based on the same technology. The electronic tuning function can be used for compensation of assembly tolerances and temperature spread.

Beside low-phase-noise fixed frequency oscillators, different tuning technologies are also considered. It is investigated how the tuning elements limit the performance of tunable oscillators. High-Q tuning elements with good power capacity are for this reason, RF-MEMSs. We have demonstrated digital tuning by using switches forming an electronically tunable ground plane inside a cavity resonator. The position of the MEMSs on a PCB intruded at different depth in the cavity are investigated regarding the tuning range, frequency resolution, Q-factor, and phase noise. The design demonstrates a 12.3 % digital tuning with phase noise varying from -133 dBc/Hz to -123 dBc/Hz at 100 kHz offset frequency around an oscillation frequency of 10 GHz.

For analogue tuning, solid state varactors are investigated. The setup is very similar as for the MEMS setup, with GaAs varactors assembled on the PCB. The varactors are aligned with the E-field of the TE_{101} resonant mode inside the cavity to form an efficient coupling for varied positions. The coupling is chosen for or a compromise between tunability and noise performance. A tuning range of 1.6 % around a 10 GHz oscillation frequency is recorded with a phase noise down to -118 dBc/Hz at 100 kHz offset. A problem with the varactors are their finite power capability limiting the large-signal Q-factor. Measurements of the cavity for low excitation power show significantly higher Q_0 than for the power levels valid in the resonator under oscillation condition. The large-signal Q-degradation is identified as the main reason why the measured phase noise is worse compared to simulations based on small-signal Q-factor. This motivates usage of high power capacity varactors as SiC-varactors for tuning of high Q-resonators.

The RF-MEMS tuning has shown some issues regarding electroacoustic conversion, i.e., microphony. In particular, for MEMS-switches in the open state with no forces applied on the membrane, mechanical resonances can appear and modulate the signal. For this reason, MEMS-based varactors are not preferable, despite their extremely high power capability. A remedy to suppress the resonances is to prevent the membrane from motion in the static states. A secondary electrode, which could fix the membrane in the open state, would be beneficial. Further investigation also includes some reliability issues regarding stitching and bonding effect of the membranes.

This work has demonstrated optimization and analysis of oscillators. Parameters to influence by design are discussed to optimally utilize the performance of the including parts and achieve performance close theoretical bounds. By combining different technologies, excellent phase noise and good tunability are demonstrated. The thesis has shown methods and strategies to build optimized oscillators, which are needed to meet the demands of cutting edge technology in future communication systems.

Summary of appended papers

Paper [A]

Analysis of a MEMS Tuned Cavity Oscillator on X-band

In this paper, a cavity oscillator on X-band with an electronically tunable wall of RF MEMS-switches are analyzed in detail regarding the position of the MEMSs' for best tuning range, phase noise, and digital resolution.

My contribution is design and implementation of the oscillator, verification, and analysis of the result. I have been the first author of the paper.

Paper [B]

RF-MEMS Tuned GaN HEMT based Cavity Oscillator for X-band

In this paper, a cavity oscillator on X-band with an electronically tunable wall of RF MEMS-switches shows a digital tuning capability of 5 %, maintaining good phase noise of about -140 dBc/Hz at 100 kHz offset. A novel building practice of an aluminum cavity with an intruded PCB of MEMS switches coupled to a microstrip line connected to a GaN-HEMT reflection amplifier is demonstrated.

My contribution is design of the oscillator with MEMS-tuning, verification, and analysis. I have been the first author of the paper.

Paper [C]

Phase Noise Analysis of an X-Band Ultra-low Phase Noise GaN HEMT based Cavity Oscillator

In this paper, a state-of-the-art cavity oscillator for fixed frequency on X-band is presented. It reports an analysis to find the best resonator coupling, by changing the position of the cavity.

My contribution is design of the oscillator, verification, and analysis of the results. I have been first author of the paper.

Paper [D]

A GaN HEMT X-band Cavity Oscillator with Electronic Gain Control

This paper presents a novel method to change the gain of a MMIC-reflection amplifier in GaN-HEMT, without degrading the Q-factor for a connected resonator. By an electronic change of the gain, the optimum coupling to the resonator can always be maintained, which is essential for a well-designed oscillator.

My contribution is MMIC-design, verification, and analysis of the oscillator. I have been the first author of the paper.

Paper [E]

Low phase noise power-efficient MMIC GaN-HEMT Oscillator at 15 GHz based on a Quasi-lumped on-chip resonator

This paper reports on a fixed frequency MMIC oscillator, with an integrated resonator of lumped LC, which is optimally coupled by an impedance transformation to the active transistor. It shows a state-of-the-art performance of a fixed frequency oscillator in GaN-HEMT.

My contribution is verification and analysis of the design. I have been the first author of the paper.

Paper [F]

Phase noise analysis of a tuned-input/tuned-output oscillator based on a GaN HEMT device

This paper reports on a hybrid oscillator, with a GaN-HEMT device connected to a lumped LC-resonator on a PCB. By changing the resonator impedance, an optimal coupling is found, and the optimum bias for best phase noise is analyzed for different frequency offset to show the effect of flicker noise. The GaN-HEMT device is characterized regarding flicker noise.

My contribution is designing the oscillator, measuring, and analyzing the results. I have been the first author of the paper.

Paper [G]

An X-band varactor-tuned cavity oscillator

This paper reports on a varactor tuned cavity oscillator. An embedded PCB with mounted varactors inside the cavity demonstrates a tuning capacitance efficiently coupled to the RF-field. This method enhances a rather large tuning-range and maintaining good Q-factor of the resonator.

My contribution is designing the oscillator, measuring and analyzing the results. I have been the first author of the paper.

Paper [H]

Low-Frequency Noise Measurements - A Technology Benchmark with Target on Oscillator Applications

This paper reports on low-frequency noise measurements of different devices, as GaN-HEMT, InGaP HBT, and GaAs pHEMT with high bias level in the saturated region for targeting oscillator application.

My contribution is developing the measurement setup.

Acknowledgements

This work would never be done for me without some remarkable great persons that supported me in the daily work.

First, I would like to express my gratitude to my examiner and head of the Microwave Electronics Laboratory, Prof. Herbert Zirath, and Prof. Jan Grahn as head of the GigaHertz Center who let me into this wonderful academic world again, and for providing a stimulating and pleasant research environment.

An extremely gratitude I would like to express to my supervisor, Dr. Dan Kuylenstierna, who guided me through the academic work and gave me daily advice and continuous encouragement, and for helping me with writing and practical things in the laboratory work as wire bonding, or in other words, for being the best supervisor!

Special thanks, I would like to bring to Dr. Szhau Lai for introducing me the research field, and for being a discussion colleague throughout the work. Special thanks also to Dr. Mustafa Özen, Dr. Rumen Kozhuharov, and Dr. Vessen Vassilev for giving me much advice. Thanks, Thanh Ngoc Thi Do and Mingquan Bao for many fruitful discussions within the GaNOsc project, and to Carl-Magnus Kihlman and Mats Myremark for mechanical and production support.

I would like to thank all other colleagues at the Microwave Electronics Laboratory who have made the daily work being lovely.

Special thanks, I would like to bring to my managers, sponsors, mentors and colleagues at Ericsson AB, in particular to Dr. Peter Olanders, Dr. Hannes Medelius, and Annika Engblom who have sponsored my work. Many thanks to Thomas Emanuelsson for being my mentor and for bringing interesting research topics and valuing my research work for Ericsson and to Per Ligander for valuable assistance and fruitful discussions. I would like to bring special thanks to Ericsson's staff at the production facility in Borås who made all tricky assembly possible.

Finally, I would like to thank my family, my wife Karin, my daughters Annie and Emelie for supporting me and making me feel loved all the time. I love you so much!

This work was supported by the GigaHertz Center in a joint research project financed by the Swedish Governmental Agency for Innovation Systems, (VINNOVA), Chalmers University of Technology, Ericsson AB and Ruag Space AB.

References

[1] A. K. P. Ulrich L. Rohde, Georg Boeck, *The Design of Modern Microwave Oscillators for Wireless Applications*: John Wiley & Sons, Inc, 2005.

[2] F. B. Llewellyn, "Constant frequency oscillators," *The Bell System Technical Journal,* vol. 11, pp. 67-100, 1932.

[3] E. Peterson, J. G. Kreer, and L. A. Ware, "Regeneration theory and experiment," *The Bell System Technical Journal,* vol. 13, pp. 680-700, 1934.

[4] W. A. Edson, "Noise in Oscillators," *Proceedings of the IRE,* vol. 48, pp. 1454-1466, 1960.

[5] E. H. Colpitts, "Oscillation generator," US 1624537, 12 April 1927, 1918.

[6] E. B. Craft and E. H. Colpitts, "Radio Telephony," *Transactions of the American Institute of Electrical Engineers,* vol. XXXVIII, pp. 305-343, 1919.

[7] J. K. Clapp, "An Inductance-Capacitance Oscillator of Unusual Frequency Stability," *Proceedings of the IRE,* vol. 36, pp. 356-358, 1948.

[8] M. Prigent, M. Camiade, J. C. Nallatamby, J. Guittard, and J. Obregon, "An efficient design method of microwave oscillator circuits for minimum phase noise," *IEEE Trans. Microw. Theory Techn.,* vol. 47, pp. 1122-1125, 1999.

[9] D. B. Leeson, "A simple model of feedback oscillator noise spectrum," *Proc. IEEE,* vol. 54, pp. 329-330, Feb 1966.

[10] K. Kurokawa, "Some basic characteristics of broadband negative resistance oscillator circuits," *The Bell System Technical Journal,* vol. 48, pp. 1937-1955, 1969.

[11] K. Kurokawa, "Noise in Synchronized Oscillators," *IEEE Trans. Microw. Theory Techn.,* vol. 16, pp. 234-240, 1968.

[12] V. Rizzoli, F. Mastri, and C. Cecchetti, "Computer-aided noise analysis of MESFET and HEMT mixers," *IEEE Trans. Microw. Theory Techn.,* vol. 37, pp. 1401-1410, 1989.

[13] H. K. Gummel and H. C. Poon, "An integral charge control model of bipolar transistors," *The Bell System Technical Journal,* vol. 49, pp. 827-852, 1970.

[14] H. Statz, H. A. Haus, and R. A. Pucel, "Noise characteristics of gallium arsenide field-effect transistors," *Electron Devices, IEEE Transactions on,* vol. 21, pp. 549-562, 1974.

[15] M. W. Pospieszalski, "Modeling of noise parameters of MESFETs and MODFETs and their frequency and temperature dependence," *Microwave Theory and Techniques, IEEE Transactions on,* vol. 37, pp. 1340-1350, 1989.

[16] I. Angelov, H. Zirath, and N. Rorsman, "A new empirical nonlinear model for HEMT and MESFET devices," *IEEE Trans. Microw. Theory Techn.,* vol. 40, pp. 2258-2266, 1992.

[17] I. Angelov, R. Kozhuharov, and H. Zirath, "A simple bias dependant LF FET noise model for CAD," in *IEEE MTT-S Int. Dig.* , 2001, pp. 407-410 vol.1.

[18] A. Hajimiri and T. H. Lee, "A general theory of phase noise in electrical oscillators," *IEEE J. Solid-State Circuits,* vol. 33 no. 2, pp. 179-194, Feb 1998.

[19] J. Antes and I. Kallfass, "Performance Estimation for Broadband Multi-Gigabit Millimeter- and Sub-Millimeter-Wave Wireless Communication Links," *IEEE Trans. Microw. Theory Techn.,* vol. 63, pp. 3288-3299, 2015.

[20] M. R. Khanzadi, D. Kuylenstierna, A. Panahi, T. Eriksson, and H. Zirath, "Calculation of the Performance of Communication Systems From Measured Oscillator Phase Noise," *Circuits and Systems I: Regular Papers, IEEE Transactions on,* vol. 61, pp. 1553-1565, 2014.

[21] J. Everard, X. Min, and S. Bale, "Simplified phase noise model for negative-resistance oscillators and a comparison with feedback oscillator models," *IEEE Trans. Ultrason., Ferroelectr., Freq. Contr.,* vol. 59, no.3, pp. 382-390, Mar 2012.

[22] G. M. Rebeiz, *RF MEMS: Theory, Design and Technology*: Hoboken, John Wiley & Sons, 2003.

[23] J. Everard, *Fundamentals of RF Circuit Design with Low Noise Oscillators*. New York,: NY: Wiley, 2001.

[24] T. Eriksson, *Private conversation of phase noise limitations of the datacapacity at Chalmers,* 2015.

[25] Behzad. Razavi, *RF Microelectronics*: Prentice-Hall, Inc, 1998.

[26] H. Nyquist, "Thermal Agitation of Electric Charge in Conductors," *Physical Review,* vol. 32, pp. 110-113, July 1928.

[27] J. B. Johnson, "Thermal Agitation of Electricity in Conductors," *Physical Review,* vol. 32, pp. 97-109, July 1928.

[28] J. G. Tartarin, G. Soubercaze-Pun, L. Bary, C. Chambon, S. Gribaldo, O. Llopis*, et al.*, "Low Frequency and linear high frequency noise performances of AlGaN/GaN grown on SiC substrate," in *European Gallium Arsenide and Other Semiconductor Application Symposium, GAAS 2005* 2005, pp. 277-280.

[29] Z. H. Liu, S. Arulkumaran, and G. I. Ng, "Improved Microwave Noise Performance by SiN Passivation in AlGaN/GaN HEMTs on Si," *IEEE Microw. Compon. Lett.,* vol. 19, pp. 383-385, 2009.

[30] M. Reisch, *High-Frequency Bipolar Transistors, Physics Modeling, Applications*: Springer-Veriag Berlin Heidelberg, 2003.

[31] L. Szhau, D. Kuylenstierna, M. Hörberg, N. Rorsman, I. Angelov, K. Andersson*, et al.*, "Accurate Phase-Noise Prediction for a Balanced Colpitts GaN HEMT MMIC Oscillator," *IEEE Trans. Microw. Theory Techn.,* vol. 61, pp. 3916-3926, 2013.

[32] A. Grebennikov, *RF and Microwave Transistor Oscillator Design*: John Wiley & Sons Ltd, 2007.

[33] R. W.Rhea, *Oscillator Design & Computer Simulation*: McGraw-Hill, 1995.

[34] A. Hati, D. A. Howe, F. L. Walls, and D. Walker, "Noise figure vs. PM noise measurements: a study at microwave frequencies," in *IEEE International Frequency Control Symposium and PDA Exhibition Jointly with the 17th European Frequency and Time Forum, 2003. Proceedings of the 2003*, 2003, pp. 516-520.

[35] R. W. Rhea, *Discrete Oscillator Design: Linear, Nonlinear, Transient, and Noise Domains* Artech House, 2010.

[36] J. Everard, "Low Phase Noise Oscillators including some Detailed Designs," in *Proc. IEEE Int. Freq. Control Symp. (FCS), 2007, Joint with the 21st European Frequency and Time Forum*, 2007, pp. 1156-1163.

[37] J. Everard, "Low phase noise signal generation; Models and theory; Oscillators and their key elements; Fractional regenerative frequency division; Teaching," in *2012 IEEE International Frequency Control Symposium Proceedings*, 2012, pp. 1-6.
[38] T. E. Parker, "Current Developments in SAW Oscillator Stability," in *31st Annual Symposium on Frequency Control. 1977*, 1977, pp. 359-364.
[39] J. Everard and M. Xi, "Simplified phase noise model for negative resistance oscillators," in *2011 Joint Conference of the IEEE International Frequency Control and the European Frequency and Time Forum (FCS) Proceedings*, 2011, pp. 1-5.
[40] G. Gonzalez, *Microwave Transistor amplifiers Analysis and Design*: Prentice-Hall, Inc., 1984.
[41] G. Gonzalez, *Foundations of oscillator circuit design*: Artech House, Inc., 2007.
[42] K. K. M. Cheng and J. K. A. Everard, "Noise Performance Degradation in Feedback Oscillators with non zero Phase Error," *Microwave and Optical Technology Letters,* vol. 4, pp. 64-66, 1991.
[43] X. Zhang, X. Han, M. Balinskiy, and H. X. Tang, "Compact, widely tunable, half-lambda YIG oscillator," in *Proc. IEEE Int. Freq. Control Symp. (FCS)*, 2012, pp. 1-3.
[44] D. Kuylenstierna, S. Lai, B. Mingquan, and H. Zirath, "Design of Low Phase-Noise Oscillators and Wideband VCOs in InGaP HBT Technology," *IEEE Trans. Microw. Theory Techn,* vol. 60, pp. 3420-3430, 2012.
[45] J. W. M. Rogers, J. A. Macedo, and C. Plett, "The effect of varactor nonlinearity on the phase noise of completely integrated VCOs," *IEEE J. Solid-State Circuits,* vol. 35, pp. 1360-1367, 2000.
[46] G. Kahmen, M. Wietstruck, M. Kaynak, B. Tillack, and H. Schumacher, "Static and dynamic characteristics of a MEMS Varactor with broad analog capacitive tuning range for wideband RF VCO applications," in *45th Eur. Microw. Conf. (EuMC), 2015*, 2015, pp. 1011-1014.
[47] E. Björnson, M. Matthaiou, A. Pitarokoilis, and E. G. Larsson, "Distributed massive MIMO in cellular networks: Impact of imperfect hardware and number of oscillators," in *2015 23rd European Signal Processing Conference (EUSIPCO)*, 2015, pp. 2436-2440.
[48] A. Wagemans, P. Ballus, R. Dekker, A. Hoogstraate, H. Maas, A. Tombeur*, et al.*, "A 3.5 mW 2.5 GHz diversity receiver and a 1.2 mW 3.6 GHz VCO in silicon-on-anything," in *IEEE Int. Solid-State Circuits Conf. Tech. Dig.*, 1998, pp. 250-251.
[49] J. van der Tang and D. Kasperkovitz, "Oscillator design efficiency: A new figure of merit for oscillator benchmarking,," in *Proc. IEEE ISCAS*, 2000, pp. 533-536.
[50] H. Zirath, "Low phase-noise balanced Colpitt InGaP-GaAs HBT VCOs with wide frequency tuning range and small VCO-gain variation," in *Microwave Conference, 2007. APMC 2007. Asia-Pacific*, 2007, pp. 1-4.
[51] I. Bahl, *Lumped Elements for RF and Microwave Circuits*: Artech House, 2003.
[52] H. Zirath, R. Kozhuharov, and M. Ferndahl, "Balanced Colpitt oscillator MMICs designed for ultra-low phase noise," *IEEE J. Solid-State Circuits,* vol. 40, pp. 2077-2086, 2005.
[53] B. Mingquan, L. Yinggang, and H. Jacobsson, "A 25-GHz ultra-low phase noise InGaP/GaAs HBT VCO," *IEEE Microw. Compon. Lett.,* vol. 15, pp. 751-753, 2005.

[54] D. Baek, K. Sangsoo, K. Jeong-Geun, K. Dong-Wook, and H. Songcheol, "Ku-band InGaP-GaAs HBT MMIC VCOs with balanced and differential topologies," *IEEE Trans. Microw. Theory Techn.,* vol. 52, pp. 1353-1359, 2004.

[55] L. Xiaoyong, S. Shekhar, and D. J. Allstot, "Gm-Boosted Common-Gate LNA and Differential Colpitts VCO/QVCO in 0.18-um CMOS," *IEEE J. Solid-State Circuits,* vol. 40, pp. 2609-2619, 2005.

[56] D. Hauspie, P. Eun-Chul, and J. Craninckx, "Wideband VCO With Simultaneous Switching of Frequency Band, Active Core, and Varactor Size," *IEEE J. Solid-State Circuits,* vol. 42, pp. 1472-1480, 2007.

[57] H. Jong-Phil and L. Sang-Gug, "Low phase noise gm-boosted differential Colpitts VCO with suppressed AM-to-FM conversion," in *Radio Frequency Integrated Circuits Symposium, 2009. RFIC 2009. IEEE*, 2009, pp. 255-258.

[58] V. S. Kaper, V. Tilak, H. Kim, A. V. Vertiatchikh, R. M. Thompson, T. R. Prunty*, et al.*, "High-power monolithic AlGaN/GaN HEMT oscillator," *IEEE J. Solid-State Circuits,* vol. 38, pp. 1457-1461, 2003.

[59] V. S. Kaper, R. M. Thompson, T. R. Prunty, and J. R. Shealy, "Signal generation, control, and frequency conversion AlGaN/GaN HEMT MMICs," *IEEE Trans. Microw. Theory Techn.,* vol. 53, pp. 55-65, 2005.

[60] X. Hongtao, C. Sanabria, N. K. Pervez, S. Keller, U. K. Mishra, and R. A. York, "Low phase-noise 5 GHz AlGaN/GaN HEMT oscillator integrated with Ba(x)Sr(1-x)TiO3 thin films," in *IEEE MTT-S Int. Dig.* , 2004, pp. 1509-1512 Vol.3.

[61] G. Soubercaze-Pun, J. G. Tartarin, L. Bary, J. Rayssac, E. Morvan, B. Grimbert*, et al.*, "Design of a X-band GaN oscillator: from the low frequency noise device characterization and large signal modeling to circuit design," in *IEEE MTT-S Int. Dig.* , 2006, pp. 747-750.

[62] C. Sanabria, X. Hongtao, S. Heikman, U. K. Mishra, and R. A. York, "A GaN differential oscillator with improved harmonic performance," *IEEE Microw. Compon. Lett.,* vol. 15, pp. 463-465, 2005.

[63] J. G. Tartarin, K. W. Wong, E. Thurnier, and O. Llopis, "X-band and K-band low-phase-noise VCOs using SiGe BiCMOS technology," in *SiGe Technology and Device Meeting, 2006. ISTDM 2006. Third International*, 2006, pp. 1-2.

[64] C. N. Rheinfelder, K. M. Strohm, L. Metzger, H. Kibbel, J. F. Luy, and W. Heinrich, "47 GHz SiGe-MMIC oscillator," in *IEEE MTT-S Int. Dig.*, 1999, pp. 5-8 vol.1.

[65] H. Jacobsson, B. Hansson, H. Berg, and S. Gevorgian, "Very low phase-noise fully-integrated coupled VCOs," in *IEEE MTT-S Int. Dig.* , 2002, pp. 577-580 vol.1.

[66] J. Maree, J. B. de Swardt, and P. W. van der Walt, "Low phase noise cylindrical cavity oscillator," in *IEEE AFRICON 2013*, 2013, pp. 1-5.

[67] P. Rice, M. Moore, A. R. Barnes, M. J. Uren, N. Malbert, N. Labat*, et al.*, "A 10 GHz dielectric resonator oscillator using GaN technology," in *2004 IEEE MTT-S Int. Dig.*, Fort Worth, TX, 2004, pp. 1497-1500.

[68] C. Florian, P. A. Traverso, G. Vannini, and F. Filicori, "Design of Low Phase Noise Dielectric Resonator Oscillators with GaInP HBT devices exploiting a Non-Linear Noise Model," in *2007 IEEE MTT-S Int. Dig.*, Honolulu, HI, 2007, pp. 1525-1528.

[69] T. P. Wang, "A fully integrated w-band push-push CMOS VCO with low phase noise and wide tuning range," *IEEE Trans. Ultrason., Ferroelectr., Freq. Control,* vol. 58, pp. 1307-1319, 2011.

[70] L. Zhou, Z. Wu, M. Sallin, and J. Everard, "Broad tuning ultra low phase noise dielectric resonator oscillators using SiGe amplifier and ceramic-based resonators," *IET Microwaves, Antennas & Propagation,* vol. 1, pp. 1064-1070, 2007.

[71] M. Nick and A. Mortazawi, "A very low phase-noise voltage-controlled-oscillator at X-band," in *IEEE MTT-S Int. Microw. Symp, 2011*, 2011, pp. 1-4.

[72] L. Zhou, W. Y. Yin, J. Wang, and L. S. Wu, "Dielectric Resonators With High Q-Factor for Tunable Low Phase Noise Oscillators," *IEEE Trans. Compon. Packag. Manuf. Technol.,* vol. 3, pp. 1008-1015, 2013.

[73] W. C. Huang, P. Chen, Z. Q. Yu, L. Tian, and J. Y. Zhou, "An electrically tunable X-Band voltage-controlled oscillator using substrate integrated waveguide dual-mode bandpass filter with circular cavity," in *45th Eur. Microw. Conf. (EuMC), 2015*, 2015, pp. 247-250.

[74] G. Kahmen, M. Wietstruck, and H. Schumacher, "An ultra-low phase noise 3.37-3.58 GHz MEMS varactor based VCO with continuous frequency tuning," in *IEEE MTT-S Int. Microw. Symp, 2016*, 2016, pp. 1-4.

[75] Z. Chen, W. Hong, J. Chen, and J. Zhou, "Design of High-Q Tunable SIW Resonator and Its Application to Low Phase Noise VCO," *IEEE Microw. Compon. Lett.,* vol. 23, pp. 43-45, 2013.

[76] A. Collado, F. Mira, and A. Georgiadis, "Mechanically Tunable Substrate Integrated Waveguide (SIW) Cavity Based Oscillator," *IEEE Microw. Compon. Lett.,* vol. 23, pp. 489-491, 2013.

[77] B. I. Son, H. C. Jeong, and K. W. Yeom, "Design of a low phase noise voltage tuned DRO based on improved dielectric resonator coupling structure," in *2012 Asia Pacific Microwave Conference Proceedings*, 2012, pp. 1121-1123.

[78] A. K. Poddar, U. L. Rohde, and T. Itoh, "Multi-knots Möbius Strips: Applications in oscillator circuits," in *IEEE MTT-S Int. Microw. Symp, 2015*, 2015, pp. 1-4.

[79] T. Nakamura, T. Masuda, N. Shiramizu, A. Nakamura, and K. Washio, "A 1.1-V Regulator-Stabilized 21.4-GHz VCO and a 115% Frequency-Range Dynamic Divider for K-Band Wireless Communication," *IEEE Trans. Microw. Theory Techn.,* vol. 60, pp. 2823-2832, 2012.

[80] F. F. He, K. Wu, W. Hong, L. Han, and X. Chen, "A Low Phase-Noise VCO Using an Electronically Tunable Substrate Integrated Waveguide Resonator," *IEEE Trans. Microw. Theory Techn.,* vol. 58, pp. 3452-3458, 2010.

[81] S. R. Systems, "Low Noise Current Preamplifier, SR570-DC to 1MHz current preamplifier," *Datasheet,* 2005.

[82] A. Blaum, O. Pilloud, G. Scalea, J. Victory, and F. Sischka, "A new robust on-wafer 1/f noise measurement and characterization system," in *Microelectronic Test Structures, 2001. ICMTS 2001. Proceedings of the 2001 International Conference on*, 2001, pp. 125-130.

[83] S. R. Systems, "Low-Noise Voltage Preamplifier, SR560-DC to 1MHz voltage preamplifier," *Datasheet,* 2011.

[84] C. Sanabria, "Noise of aluminum gallium nitride/gallium nitride HEMTs and oscillators," Ph.D., University of California, Santa Barbara, United States -- California, 2006.

[85] D. M. Pozar, *Microwave Engineering*, Fourth ed.: John Wiley & Sons, Inc., 2012.

[86] F. Nigon, D. Cros, S. Verdeyme, M. Aubourg, and P. Guillon, "Full wave electromagnetic analysis of planar whispering gallery mode DRO," *Electronics Letters,* vol. 33, pp. 668-669, 1997.

[87] A. A. Barannik, V. N. Skresanov, V. V. Glamazdin, A. I. Shubny, M. P. Natarov, V. A. Zolotarev*, et al.*, "Whispering gallery mode resonator unit for low phase-noise oscillators," in *2016 9th International Kharkiv Symposium on Physics and Engineering of Microwaves, Millimeter and Submillimeter Waves (MSMW)*, 2016, pp. 1-4.

[88] H. Feng Ping, Z. Xiao Wei, and M. Jun-Fa, "Design of a low phase noise oscillator based on high Q tunable dielectric resonator," in *Advanced Research and Technology in Industry Applications (WARTIA), 2014 IEEE Workshop on*, 2014, pp. 1397-1400.

[89] L. Zhou, Z. Wu, R. Chu, and J. F. Mao, "Ultra Low Noise Dielectric Resonators Oscillators with Tuning at Ku Band," in *2008 China-Japan Joint Microwave Conference*, 2008, pp. 474-477.

[90] C. T. M. Wu, T. Itoh, A. K. Poddar, and U. L. Rohde, "A C-band tunable oscillator based on complementary coupled resonator using substrate integrated waveguide cavity," in *44th Eur. Microw. Conf. (EuMC), 2014*, 2014, pp. 715-718.

[91] X. Liu, L. P. B. Katehi, W. J. Chappell, and D. Peroulis, "High-Q Tunable Microwave Cavity Resonators and Filters Using SOI-Based RF MEMS Tuners," *J. Microelectromech. Syst.,* vol. 19, pp. 774-784, 2010.

[92] S. J. Park, I. Reines, C. Patel, and G. M. Rebeiz, "High-Q RF-MEMS 4-6-GHz Tunable Evanescent-Mode Cavity Filter," *IEEE Trans. Microw. Theory Techn.,* vol. 58, pp. 381-389, 2010.

[93] B. C. Deloach, "A New Microwave Measurement Technique to Characterize Diodes and an 800-Gc Cutoff Frequency Varactor at Zero Volts Bias," *IEEE Trans. Microw. Theory Techn.,* vol. 12, pp. 15-20, 1964.

[94] C. A. Muley and S. A. Naveed, "Modelling of cantilever based MEMS RF switch," in *2013 Fourth International Conference on Computing, Communications and Networking Technologies (ICCCNT)*, 2013, pp. 1-5.

[95] G. Kahmen, M. Wietstruck, and H. Schumacher, "An ultra-low phase noise 3.37 - 3.58 GHz MEMS varactor based VCO with continuous frequency tuning," *IEEE MTT-S Int. Microw. Symp., 2016,* 2016.

[96] S. Courreges, L. Yuan, Z. Zhiyong, C. Kwang, A. Hunt, and J. Papapolymerou, "Ferroelectric Tunable Bandpass Filters for Ka-Band Applications," in *38th Eur. Microw. Conf. (EuMC)*, 2008, pp. 55-58.

[97] W. M. Fathelbab and M. B. Steer, "A reconfigurable bandpass filter for RF/microwave multifunctional systems," *IEEE Trans. Microw. Theory Techn.,* vol. 53, pp. 1111-1116, 2005.

[98] H. Fanfan, C. Xiao-Ping, W. Ke, and H. Wei, "Electrically tunable substrate integrated waveguide reflective cavity resonator," in *Microwave Conference, 2009. APMC 2009. Asia Pacific*, 2009, pp. 119-122.

[99] A. Anand, J. Small, M. S. Arif, M. Sinani, D. Peroulis, and X. Liu, "A novel high-Qu octave-tunable resonator with lumped tuning elements," in *IEEE MTT-S Int. Microw. Symp, 2013*, 2013, pp. 1-3.

[100] G. Kahmen, M. Kaynak, M. Wietstruck, B. Tillack, and H. Schumacher, "MEMS varactor with high RF power handling capability for tuning of wideband low noise RF VCOs," in *44th Eur. Microw. Conf. (EuMC), 2014*, 2014, pp. 207-210.

[101] L. Pelliccia, F. Cacciamani, P. Farinelli, and R. Sorrentino, "High-Q Tunable Waveguide Filters Using Ohmic RF MEMS Switches," *IEEE Trans. Microw. Theory Techn.,* vol. 63, pp. 3381-3390, 2015.

[102] Rohde&Schwarz, "R&S FSUP Signal Source Analyzer Specifications," *Version 06.02,* Feb 2009.

[103] Agilent Technologies, "Agilent's Phase Noise Measurement Solutions," *Selection guide and datasheet,* July 31 2013.